EPFL

Thèse n° 10 464

Modeling and optimization of PCB coils for inductive power transfer systems

Présentée le 23 février 2024

Faculté des sciences et techniques de l'ingénieur
Laboratoire d'électronique de puissance
Programme doctoral en génie électrique

pour l'obtention du grade de Docteur ès Sciences

par

Xiaotong DU

Acceptée sur proposition du jury

Prof. A. P. Burg, président du jury
Prof. D. Dujic, directeur de thèse
Prof. Z. Ouyang, rapporteur
Dr V. Lazarevic, rapporteur
Prof. F. Rachidi-Haeri, rapporteur

École polytechnique fédérale de Lausanne

2024

École Polytechnique Fédérale de Lausanne
Power Electronics Laboratory
Station 11
1015 Lausanne, Switzerland

http://pel.epfl.ch

"Constrained optimization is the art of compromise between conflicting objectives. This is what design is all about."

William A. Dembski

Acknowledgements

Life is not a competition. It's a collaboration

First of all, I would like to thank Prof. Drazen Dujic for giving me the opportunity to do my Ph.D. thesis in power electronics laboratory (PEL). He has guided me into the topics of optimization design of magnetic components and given me plenty of research freedom. Furthermore, I want to thank him for sponsoring me to conferences and workshops, where I could exchange research results with experts from around the world.

Special thanks belong to Dr. Chengmin Li. The detailed discussions in many aspects of my research, and particularly his support in unraveling the mysteries of power electronics hardware, were much appreciated. Many thanks to Nikolina Djekanovic, who was my office colleague for four years. Many discussions with her in magnetics theory extended and consolidated my knowledge. I thank Dr. Andrea Cervone for his detailed explanation on control theory of electric machines. I would like to thank Dr. Ignacio Polanco, Dr. Changhwan Park, Philippe Bontemps, Jules Macé, Renan Pillon Barcelos, Stefan Subotic, Max Dupont and all the other colleagues in PEL for all the inspirational discussions and for providing a great research atmosphere. Furthermore, big thanks go to the semester and master students, who have supported me in my research: Roberto Chedraui Abud and Jérémie Veuthey.

In addition to the lab colleagues, I would like to thank all my friends outside PEL. My flatmates Li, Wanting and Yuting left me many precious memories of funny discussions, movie nights, outdoor activities. They are always generous to share nice food. Thanks to them, our apartment is not only a place to live but also a home where I regain my energy. I also want to thank LuLu, Chaoqun, Zhiwen, Aya, Jerome, Jiande, Yihui and my boyfriend Manuel. They are my hiking and swimming partners and my close friends who are always generous to encourage and support me. Whenever I need them, they are always there. Their names do not appear on our scientific publications, but without their support, many achievements would not have been possible and my Ph.D. journey would be less fun. I also want to thank many other people who I encountered during my Ph.D. and showed their kindness. I would like to thank them for their trust and support during this intense phase of my life.

Finally, I want to thank my beloved family, especially my grandmother Yueshu for her unconditional love and great confidence in me. Without her, I wouldn't be who I am today. I owe my sincerest gratitude to my parents Hongmei and Jianguo, my aunts and uncles Weijie, Weiguo, Aijun and Guoqin, my cousins Yurou and Qianqian for their priceless love and for always being my harbor though all these years.

Lausanne, October 2023

Abstract

The auxiliary power supply for medium voltage converters requires high insulation capability between the source and the load. Inductive power transfer technology, with an air gap between the primary and secondary coil, offers such high insulation capability, making it a potential candidate for auxiliary power supply in medium voltage converters. Additionally, its contactless nature provides flexibility, facilitating converter maintenance. However, the large air gap between the primary and secondary coil typically results in a loosely coupled inductive power transfer system, necessitating optimization of the inductive power transfer system to achieve high efficiency and high power density. This thesis focuses on the coil link optimization. It introduces a novel design of the coil link structure, models the coil pairs, and presents an optimization flow to design optimal winding geometry based on given system specifications. The research of this thesis revolves around PCB coils, which are favored for their easily controlled manufacturing process.

To maintain modularity in medium voltage converters, the inductive power transfer system consists of multiple coil pairs, each supplying one power electronics building block. The primary side of each coil pair is connected to a common power source. To ensure independent operation of the secondary coils without closed-loop control, the LCL-S compensation network is utilized. The advantage of this compensation network is analyzed and its design process is discussed in this thesis.

The characteristics of a coil, including self and mutual inductances and coil losses, are defined by its winding geometry. Therefore, by optimizing the winding geometry, high coil link efficiency can be achieved. This thesis develops a model to calculate the magnetic field inside each winding turn when no ferrite is present behind the winding. The brute-force optimization is conducted on the PCB coil pairs with the proposed model, resulting in a Pareto front showcasing the trade-off between high efficiency and high power density. This allows designers to choose an optimal design fitting the size constraints of their converters. To verify the magnetic model predicting the coil pair characteristics, three designs are prototyped, and one has been tested under different load conditions. Five coil pairs are connected and tested as a system, confirming the independence among different outputs.

When ferrite is added to the backside of a winding, it alters its inductance and resistance, and therefore has the potential to increase power transfer efficiency. However, the modeling of the coil pair becomes more complex due to the crowding field around ferrite edges. In this thesis, different ferrite shapes are compared, and a magnetic model with 5 mm thick round shape ferrite is proposed, based on a database from finite element simulation together with an artificial neural network, predicting the coil pair characteristics. The validity of the finite element simulation data is pre-verified with impedance analyzer and power tests, and the accuracy of the magnetic model is confirmed with simulation test datasets and characteristic tests on coil prototypes.

The design of the coil link requires thermal coordination considering the temperature limit of each component inside coils. This thesis proposes a thermal model to predict the temperature rise in coil pairs. The proposed electric circuit model with LCL-S compensation network, the magnetic model based on artificial neural network, and the thermal model based on thermal network are all independent from external simulations and easily integrated into the optimization flow, ensuring fast optimization. After exploring all degrees of freedom of winding geometries, one coil pair on the Pareto front is selected and tested under various load conditions. Additionally, the partial discharge test is performed on the coil pair to verify its insulation capability.

Keywords inductive power transfer, auxiliary power supply, design and optimization, compensation network, artificial neural network, thermal model

Résumé

L'alimentation auxiliaire des convertisseurs à moyenne tension nécessite une capacité d'isolation élevée entre la source et la charge. La technologie de transfert de puissance inductive, avec un espace d'air entre la bobine primaire et secondaire, offre une telle capacité d'isolation élevée, ce qui en fait un candidat potentiel pour l'alimentation auxiliaire des convertisseurs à moyenne tension. De plus, sa nature sans contact offre une flexibilité, facilitant la maintenance du convertisseur. Cependant, le grand espace d'air entre la bobine primaire et secondaire pourrait conduire à un système de transfert de puissance inductive faiblement couplé, nécessitant une optimisation du lien de la bobine pour atteindre une haute efficacité et une densité de puissance élevée. Cette thèse propose la conception de la structure du lien de la bobine, modélise les paires de bobines et présente un processus d'optimisation pour concevoir une géométrie d'enroulement optimale basée sur des spécifications électriques données. L'utilisation de bobines PCB est préférée en raison de leur processus de fabrication facilement contrôlable.

Pour maintenir la modularité dans les convertisseurs à moyenne tension, le système de transfert de puissance inductive se compose de plusieurs paires de bobines, chacune alimentant un bloc de construction d'électronique de puissance. Le côté primaire de chaque paire de bobines est connecté à une source commune. Pour assurer un fonctionnement indépendant des bobines secondaires sans contrôle en boucle fermée, le réseau de compensation LCL-S est utilisé. L'avantage de ce réseau de compensation est analysé et son processus de conception est discuté dans cette thèse.

Les caractéristiques d'une bobine, y compris l'inductance propre et mutuelle et les pertes de la bobine, sont définies par sa géométrie d'enroulement. Par conséquent, en optimisant la géométrie d'enroulement, une efficacité élevée du lien de la bobine peut être atteinte. Cette thèse développe un modèle pour calculer le champ magnétique à l'intérieur de chaque spire d'enroulement lorsqu'aucun ferrite n'est présent autour de l'enroulement. L'optimisation par force brute est effectuée sur les paires de bobines PCB avec le modèle proposé, ce qui donne une frontière de Pareto mettant en évidence le compromis entre haute efficacité et haute densité de puissance. Cela permet aux concepteurs de choisir une conception optimale adaptée aux contraintes de taille de leurs convertisseurs. Pour vérifier le modèle magnétique prédisant les caractéristiques de la paire de bobines, trois conceptions sont prototypées et l'une d'entre elles est soumise à des essais de puissance dans différentes conditions de charge. Cinq paires de bobines sont connectées et testées en tant que système, confirmant l'indépendance entre les différentes sorties.

Lorsqu'un ferrite est ajouté à l'arrière d'un enroulement, il modifie l'inductance et la résistance de la bobine. Le couplage entre deux bobines peut être augmenté en incorporant du ferrite. Dans cette thèse, différentes formes de ferrite sont comparées et la forme ronde est choisie comme conception finale. La modélisation de la paire de bobines devient plus complexe en raison du champ dense autour des bords du ferrite, et manque de solutions analytiques précises. Un modèle magnétique est proposé, basé sur une base de données de simulations par éléments finis associée à un réseau de neurones artificiels, pour prédire les caractéristiques de la paire de bobines. La validité des données de simulation par éléments finis est pré-vérifiée avec un analyseur d'impédance et des essais de puissance, et l'exactitude du modèle magnétique est confirmée avec des jeux de données de simulation et des tests de caractéristiques sur un prototype de paire de bobines.

La conception de la paire de bobines doit prendre en compte la coordination thermique en fonction de la limite de température dans chaque composant à l'intérieur des bobines. Cette thèse propose un modèle thermique pour prédire l'élévation de température dans les paires de bobines. Le modèle de circuit

électrique proposé avec le réseau de compensation LCL-S, le modèle magnétique basé sur le réseau de neurones artificiels et le modèle thermique basé sur le réseau thermique sont tous indépendants des simulations externes et facilement intégrés dans le processus d'optimisation, assurant un temps d'optimisation rapide. Après avoir exploré toutes les libertés de géométrie d'enroulement, une paire de bobines sur la frontière de Pareto est sélectionnée et testée dans différentes conditions de charge. De plus, des tests de décharge partielle sont effectués sur la paire de bobines pour vérifier sa capacité d'isolation.

Keywords transfert de puissance inductive, alimentation auxiliaire, conception et optimisation, réseau de compensation, réseau de neurones artificiels, modèle thermique

List of Abbreviations

ANN	artificial neural network
ANPC	active neutral point clamped (NPC)
APS	auxiliary power supply
CFD	computational fluid dynamics
CHB	cascaded H-bridge
FB	full bridge
FC	flying capacitor
FEM	finite element modeling
GA	genetic algorithm
HB	half bridge
HVdc	high voltage dc
IPT	inductive power transfer
ML	machine learning
MMC	modular multilevel converter
MV	medium voltage
NPC	neutral point clamped
NPP	neutral point piloted
OWPT	Optical wireless power transmission
PD	partial discharge
PEBB	power electronics building block
PoF	Power over fiber

Contents

1 Introduction

1.1 Medium Voltage Converters

In a modern grid, the sources and loads are either AC or DC, and power electronic converters which realize conversion in various forms (AC-DC, DC-AC, AC-AC, DC-DC), in different voltage levels and are indispensable and dominating equipment. Especially in the last 20 to 30 years, reducing CO_2 emission by replacing fossil-fuel-based power sources with renewable energy sources such as solar and wind, is getting increasing notion worldwide. An example of a modern hybrid power system incorporating conventional and renewable energy sources, loads, and energy storage elements is shown in **Fig. 1.1**.

The medium voltage (MV) converters typically work with a voltage level of 1 kV-36 kV AC and usually with a high power level of several megawatts. Typical applications of MV converters include renewable energy conversion, data centers, DC transmission and distribution grid, super-charging stations and high power variable speed drives (used in electrified transportation, petrochemical, mining, electromagnetic propulsion, and military equipment, etc.). As the critical part in these applications, medium-voltage power electronic converters directly contribute to the operational performance of the whole system.

Multilevel voltage source converters which could produce multilevel waveforms at the AC terminals have been proposed in 1980's and are currently commercialized for various applications, including marine propulsion, wind energy conversion, extruder, grinding mills, pumps, etc. Some classic topologies have been widely deployed, such as neutral point piloted (NPP), NPC [1], active NPC (ANPC) [2], flying capacitor (FC) [3] and hybrid converter composed of FC with NPC, ANPC or NPP [4]. The complexity limits the voltage scalability in practice and leads to the fact that commercially available NPC or FC having up to 5 voltage levels per converter leg.

Modular topologies including cascaded H-bridge (CHB) converters [5] and modular multilevel converter (MMC) [6] as shown in **Sec. 1.1** were proposed lately. Modularity and scalability are achieved through the cascaded connection of identical cells. The topology proposed by ROBICON company in 1997 is composed of phase shifting transformers and cascade-connected H-bridge (single-phase full-bridge) cells [5]. Compared to monolithic converters, CHB is suited to reach higher voltage and power levels by using low-cost low-voltage semiconductors. In addition, CHB has a more significant number of output voltage levels and the harmonics move to higher frequency. These characteristics of CHB permit reduction in switching frequency at the cell level, which leads to lower switching losses and improved efficiency.

Another modular converter that penetrated the industry is MMC. Its cell is typically a half-bridge or a full-bridge circuit. Since the topology and its operation principles were proposed [6], research for a

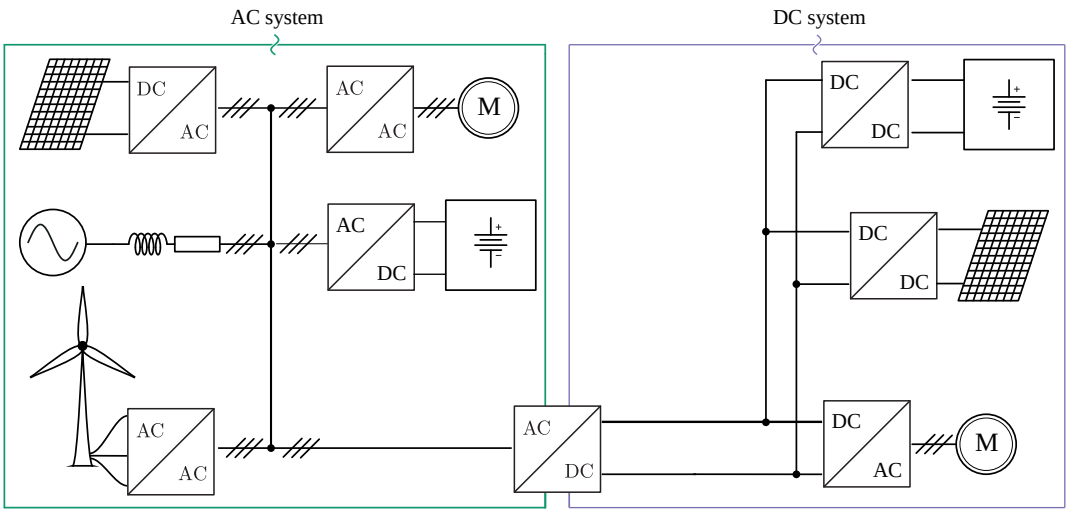

Fig. 1.1 Modern hybrid grid with sources and loads of AC or DC nature.

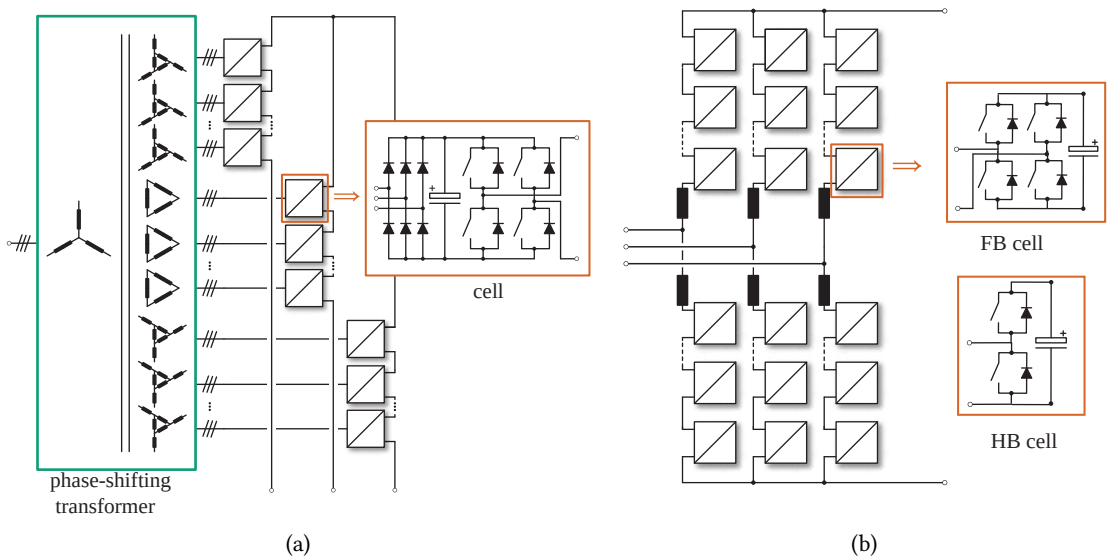

Fig. 1.2 Modular multilevel converters:(a) CHB ROBICON drive, (b) MMC with two possible cell structures.

wide range of applications has been carried out on it, including high voltage dc (HVdc), back-to-back systems, as well as MV motor drives. It can easily reach medium to high voltage levels while increasing AC side power quality due to its modularity and scalability.

As discussed above, the majority of MV converters have some modularity in the design. Each modular converter is structured from various interconnections of fundamental cells. In a modular converter, by adding or removing fundamental cells, its voltage amplitude or the output level number changes accordingly. The function definition and systematic design of the fundamental integrated block is needed.

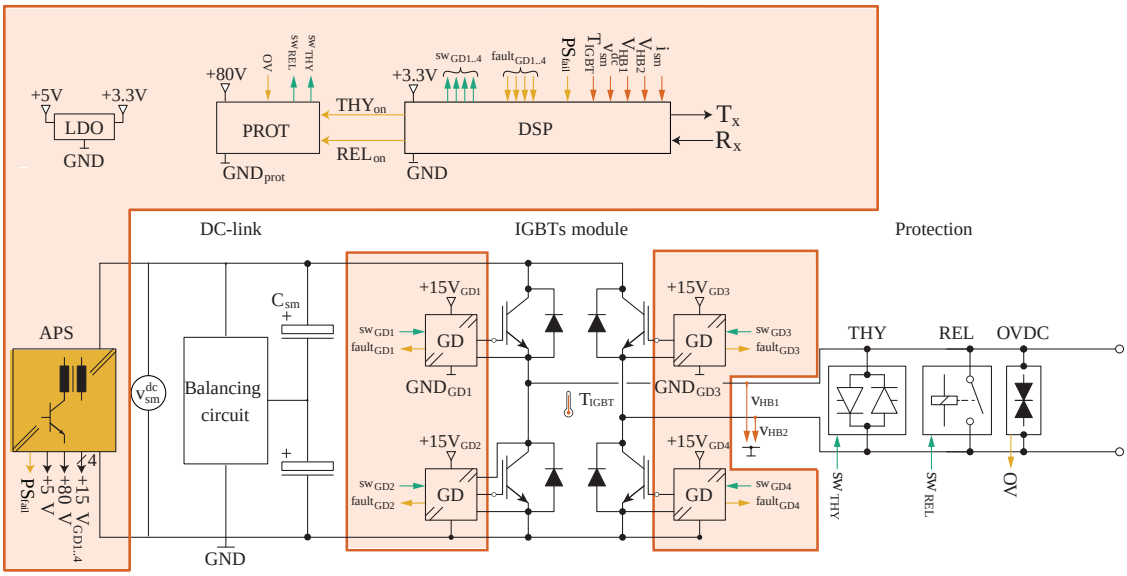

Fig. 1.3 PEBB structure for a MMC submodule [8] with APS highlighted.

1.2 Auxiliary Power Supply for Power Electronic Building Blocks

The power electronics building block (PEBB) as the fundamental block in modular converters is defined to serve various applications by integrating power devices, gate drivers, sensors, and other components together into fundamental building blocks with characteristic interfaces. It has redefined the conventional pattern of designing and manufacturing power electronics systems by incorporating several novel concepts such as flexible structure, modular design, hierarchical control design, and parallel engineering [7].

Taking the PEBB of MMC designed at the power electronics laboratory at EPFL as an example, the composition of functional PEBB is demonstrated in **Fig. 1.3**. The PEBB comprises main power switches (a full bridge (FB) power circuit in **Fig. 1.3**), capacitor, controller unit, gate driver unit, isolated digital sensor unit, protection unit and the auxiliary power supply (APS) unit. All units need to be energized to function correctly; therefore, APS, which supplies energy to those units, is critical in a PEBB structure. Commonly, APS offers around 3.3 V/5 V supply for controller chips such as DSP or FPGA; 15 V-20 V supply for gate drivers circuit; multiple power supplies for voltage, current, and temperature sensors as well as A/D conversion and amplifier; power supply for the primary protection and auxiliary elements including relays, fans, etc.

APS is usually designed to meet the following requirements: 1) to provide sufficient power for PEBB for its operation and functions; 2) to achieve high efficiency, since APS is constantly working when main converter is processing power; 3) to withstand output load variation (0%-100%) and have high dynamic response speed to ensure safe operation during instant change of PEBB working conditions; 4) to be able to operate with wide input voltage range conditions; 5) to offer sufficient insulation capability. For a modular converter, among all these requirements, sufficiently high insulation voltage and output power are core requirements. In estimation of power consumption, usually small power is needed for the sensors and controllers (< 1 W). The power required by gate driver units depends on the semiconductor types, switching frequency, and the amount of semiconductor devices in the PEBB

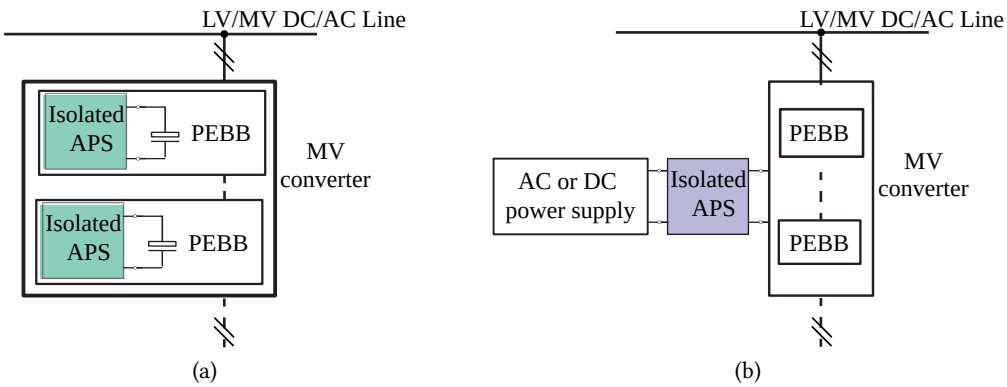

Fig. 1.4 (a) Internal APS powered from the present DC source inside the MV converter. (b) External APS powered from an external energy source.

[9]. The total required output power of APS ranges from a few watts to dozen tens of watts.

The necessary insulation voltage level is either defined by the system voltage or by the PEBB voltage. It depends on the realization of the auxiliary supply. APS is either energized from a DC link which is already present in PEBB main power stage, such as one of the system capacitors (internal APS) as shown in **Fig. 1.4a**, or from an external power source independent of the PEBB (external APS) as shown in **Fig. 1.4b**. Both solutions are widely deployed in commercial MV products, each offering pros and cons.

In modular converters, internal APS only has to offer insulation up to PEBB DC bus voltage. This attribute confers an advantage over external APS. Among internal APS solutions, transformer-isolated DC-DC converters are popular due to the design simplicity and low cost [10], [11]. Based on the flyback topology, different improvements have been made to achieve high input voltage, high step-down challenges such as input-series-output-parallel (ISOP) flyback structure [12], [13] and series-connected transistors [14], [15]. However, the internal APS only starts to power the controllers when the DC Bus voltage reaches a certain level. PEBB controllers are used to monitor local currents, voltages and temperatures, to respond instantly and to diagnose local faults. Therefore, in order to reduce the risk on power switches during start up and fault period, control and auxiliary system can be energized from an external APS. Detaching APS from the internal DC link is desired to realize non-stop and independent operation. When PEBB is shut down unexpectedly, the APS system would function as normal to ensure that the driving, communication, measuring and fault detection circuits are always enabled. Consequently, external APS is appealing solution since it ensures the independent operation fed from an external power source.

The external APS solution can adopt the similar design of an internal APS such as series connected flyback [16], however, when the voltage goes above 10 kV, the APS usually has a separate converter connected in the previous stage to convert the high voltage to low voltage as shown in **Fig. 1.4b**. Depending on the power source of the converter, different step down solutions are used in addition to isolated APS solutions. If it is AC power source, a small low power AC transformer or a non isolated AC/DC stage is usually connected to the AC line and its output connects to a galvanically isolated APS [17]. With a DC power source, non-isolated DC/DC converters can be used to step down the voltage and through an isolated APS to supply auxiliary power to the MV converters [18], [19]. No

matter which power source or which step down converter is used, a galvanically isolated APS with high insulation capability is usually necessary as the secondary stage to supply auxiliary power to the MV converters.

In modular MV converters, the external APS needs to have multiple outputs to supply all the PEBBs in the converter. Stacked PEBBs are floating with respect to ground potential, and therefore there is a huge potential difference between reference potential of PEBBs and the earthing point. Since external APS must be able to supply those floating PEBBs, it must overcome the high insulation challenge between its input and outputs. In consequence, the main constraint of external power supply for modular MV converters is related to high insulation level which is the full converter voltage amplitude. When it comes to MV converters, this insulation voltage stress could be scaled up to tens of kV. Even though realizing high insulation with traditional transformers is simple and possible, the conventional transformers become rather bulky and costly with the requirement of small power transmission. Therefore, it is beneficial to look for alternative solutions. APS system requires high insulation but at the same time the power requirement is usually less than 150 W per PEBB. The inductive power transfer (IPT) without physical contact between the primary and secondary sides is attractive solution as APS for MV converters[20]–[23], where the gap between primary and secondary side offers high insulation capability.

1.3 Inductive Power Transfer

Wireless power transfer technologies can be categorized into near-field (less than a wavelength of transmitting electromagnetic wave) and far-field (more than a wavelength). In the far-field, the electromagnetic energy propagates in the form of electromagnetic radiation which includes radio waves, microwaves, infrared, light, x-rays, and gamma rays [24]. The energy transfer efficiency of far-field electromagnetic radiation is low and is only used to transfer low power and information. In the near-field, inductive power transfer (IPT) and capacitive power transfer (CPT) are the two main wireless coupling methods. CPT transfers power through induced electric field in the two vertically positioned sets of electric dipoles. IPT is based on the interaction between the magnetic field and electric circuit: a varying magnetic field $\vec{H}$ can be generated by a varying electric current (Ampère's law). The magnetic flux going through the receiving loop will induce an electromotive force in that loop (Faraday's law). CPT systems achieve high efficiency only when the gap distance is smaller than 1 mm, and therefore are not suitable for high insulation applications [25]–[28].

An IPT system consists of an input stage power converter and an output stage power converter, the primary and secondary side compensation network, the transmitter coil and the receiver coil as shown in **Fig. 1.5**. The alternating current carried by the transmitter coil will generate a magnetic field which induces a voltage in the receiver coil. Therefore, energy is transmitted from the transmitter side to the receiver side via an air gap without any physical contact.

As shown in **Fig. 1.6**, IPT technology has been applied as the power supply in various applications spanning a wide power range and a large distance range, including bio-medical implants, portable device, home appliances, industry automation lines, electrical vehicles, etc. The research of applying IPT technology to power an artificial heart started back in 1960 [29]. From that time on, IPT has been researched in various active implantable medical devices such as drug delivery systems [30], prosthetic limb muscle activation [31] and electro-mechanical heart assist devices [32]. In those devices, the primary battery usually takes up a large space and needs to be replaced when it runs out

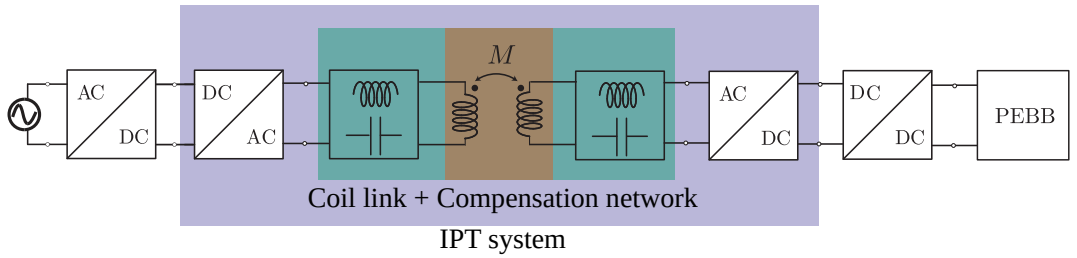

Fig. 1.5 The structure of an IPT as APS for PEBBs with the coil link, compensation networks, an inverter on the primary side and a rectifier on the secondary side highlighted.

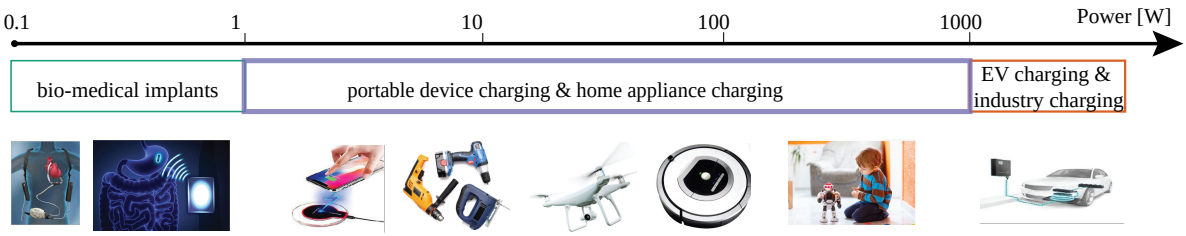

Fig. 1.6 Applications of IPT systems. From left to right it shows applications on bio-medical implants, phones, household tools, drones, cleaning robots, toys, and vehicles.

of energy. An IPT solution could charge the battery from outside of the human body or can even work nonstop to replace the battery solution. The power demand is usually less than 1 W and the charging system usually has a tiny size (<1 cm^2) and typically small gap (< 3 cm) [33], [34]. These size constraints require the IPT system to operate at MHz range. The challenge for IPT charge for medical implants applications is related to safety issues caused by the electromagnetic field near human organs [35], and the heat generated by coils on human skin tissues.

For slightly higher power usage from 5 W to 100 W, IPT has been widely used in portable mobile devices such as phone and tablet charging. Qi standard for the charging system below 65 W has been proposed, and nowadays there are countless Qi compatible phones, tablets and other devices on the market [36]. The operating frequency is from 105 kHz to 205 kHz which is far away from the radio frequency to avoid signal interference. The design of the charger needs to achieve high power transfer efficiency. The transmitter and receiver coil should be well aligned. This is usually realized by either using multiple transmitter coils, or mechanically aligning a single transmitting coil with the receiving coil.

Recently, there is interest in developing IPT charger systems above 30 W for portable power tools, robotic vacuum cleaners, drones and e-bikes [37]–[40]. In the medium power range, the Ki cordless kitchen standard defines versatile cooktops that wirelessly deliver up to 2200 watts of power to smart cordless kitchen appliances [41]. Using IPT for power transferring and battery charging adds cord-free flexibility and freedom to those products. Recently, multiple pickup IPT systems are popular especially in clean rooms and material handling applications due to its cord-free, clean and safe advantage [42], [43]. Fast control and power management are the special challenges in multiple pickup systems.

High power IPT above 1 kW is widely used in industry, such as floor conveyors in assembly lines and electrified rail systems [44]. Recently, IPT has been considered as an alternative solution for electric vehicle charging. Besides its convenience, the compatibility to opportunity charging makes

IPT solution more attractive. Opportunity charging refers to charging the vehicles discretely in short time rather than continuously charge it in a longer time. An IPT system installed at the fixed stops such as bus stop, parking lot, traffic lights makes opportunity charging feasible. The challenges to achieve higher efficiency lies in coil misalignment and dynamic charging [45], [46]. In addition, safety concern requires foreign object detection and smart control system to regulate the power. Until recently, private vehicles, public transportation and cargos with IPT charging solutions were tested in different projects and started to enter the market [47], [48]. In the future, IPT charging solutions have potential to further enlarge its market share.

In addition to the applications discussed above, IPT is a potential solution to the high insulation needing applications due to its contactless nature. IPT coils form a transformer with a large air gap, and the gap between its primary and secondary winding could serve as a natural galvanic insulation medium. One scenario which exhibits high insulation level challenges is the APS system in MV converters.

1.4 Objectives and Contribution

Even though IPT technology has been commercially deployed in several applications, there are several challenges considering the application of auxiliary power supply in MV converters. On one hand, as in various applications, high power transfer efficiency and high power density are expected because external APS is operating continuously, even when main converter is not processing power. On the other hand, mechanical arrangement imposes constraints on the coil size, and a large gap exists between primary and secondary coils due to MV insulation coordination [49], [50]. The coil size constraints and the gap between coils introduces new challenges in designing a high efficiency IPT system.

The main objectives of the thesis are related to design optimization of IPT systems as APS for MV converters. A possible converter realization with IPT as APSs is shown in **Fig. 1.7**. Specifically to the APS application, the design constraints of IPT systems are: sufficient output power for all modular PEBBs, independent and constant output voltage, thermal and insulation coordination, and the physical size limitation. The optimization goal is to achieve high efficiency and high power density. The main contribution of the thesis can be summarized as:

- Modeling, optimization design and prototyping of PCB coil pairs. Improvements of the accuracy of the existing winding loss models and derivation of new analytic models for PCB spiral coils.
- Modeling of the effect of adding ferrite on coils backside. Extension of analysis into different ferrite geometries and shorter computation time compared to existing models.
- Analytic thermal modeling of the integrated coil, which takes all the structure and material parameters as design freedoms and offers fast computation.
- Systematic optimization flow for PCB based IPT coil pairs with electric specifications defined for APS in MV converters.

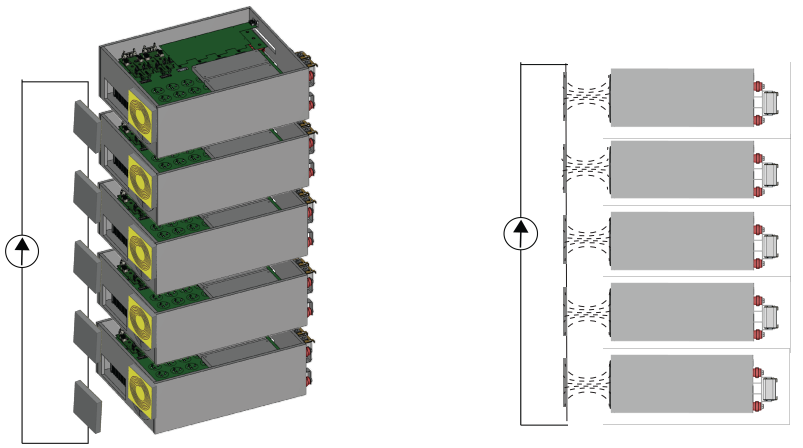

Fig. 1.7 Conceptual illustration of one branch of CHB composed of five PEBBs with IPT as APS. On the left side is the 3D view, on the right side shows the side view.

1.5 Outline of the Thesis

This thesis is organized into eight chapters following the design logic of IPT coil link. The thesis firstly presents the state of art of APS for MV converters and various IPT solutions. Then the design of each part in the coil link is discussed in each chapter, which includes compensation network design, the coil geometry design and the ferrite shape design. Based on the structure of the coil system and the loss modeling, the thermal network is build. In the end, the systematic design optimization of the entire IPT system is presented.

- **Chapter 2** introduces different solutions for external auxiliary power supplies of MV converters. Different layouts of IPT system are also compared. The IPT structure deployed in this thesis is with series-connected primary PCB coils and independent secondary PCB coils. This chapter later discusses the free design space in a coil link which includes the compensation network, winding and magnetic shielding.
- **Chapter 3** focuses on the compensation network design as part of coil link design. Commonly used compensation networks are presented and analyzed, with different performance and characteristics compared. Considering the requirement of constant and independent output among coil pairs in our application scenario, the compensation network structure is determined, and the component dimensioning rule is introduced.
- **Chapter 4** builds the magnetic model to predict the inductance and high frequency resistance of coils without ferrite, based on which, the brute-force search is executed in the coil geometry design space to find optimal coil geometry to achieve high power transfer efficiency of coil link and small coil size. A coil pair from Pareto front is prototyped and tested under different load conditions.
- **Chapter 5** presents the magnetic model for coil with ferrite on PCB's backside. Different ferrite geometries are firstly compared in perspective of quality factor and coupling factor, and the model is built on the selected optimal ferrite shape. The artificial neural network (ANN) together with finite element modeling (FEM) database is utilized to build the model. Test is done on the prototype from Chapter 4 to verify the accuracy of the model.

- **Chapter 6** proposes an axial symmetrical thermal network based on the integrated coil structure. The thermal model predicts the temperature rise inside the coil in the stable state, and is verified for different coil sizes, coil orientation, winding geometries and room temperatures through thermal test.
- **Chapter 7** proposes the optimization flow to achieve high efficiency and high power density, based on the thermal model and the magnetic model with ferrite. The optimization is done with genetic algorithm (GA) in design space. One coil pair on Pareto front is prototyped and tested.
- **Chapter 8** concludes the main obtained results in this thesis and previewing future activities around this topic.

1.6 List of Publications

Journal papers:

[1] X. Du and D. Dujic, "Modeling and Design Optimization of Loosely Coupled PCB Spiral Coils in Inductive Power Transfer Systems," IEEE Transactions on Power Electronics, vol. 38, no. 11, pp. 13430-13442, Nov. 2023.

[2] X. Du, C. Li and D. Dujić, "Design and Characterization of PCB Spiral Coils for Inductive Power Transfer in Medium-Voltage Applications," IEEE Transactions on Power Electronics, vol. 37, no. 5, pp. 6168-6180, May 2022.

Conference papers:

[1] X. Du, C. Li and D. Dujic, "Inductive Power Transfer System for Auxiliary Power Supply in MV Converters," PCIM Europe 2022; International Exhibition and Conference for Power Electronics, Intelligent Motion, Renewable Energy and Energy Management, Nuremberg, Germany, 2022, pp. 1-9.

[2] X. Du and D. Dujić, "Inductive Power Transfer System with Series Connected Primary and Independent Secondary Coils," IECON 2020 The 46th Annual Conference of the IEEE Industrial Electronics Society, Singapore, 2020, pp. 3901-3906.

2

Auxiliary Power Supply for Medium Voltage Converters

Based on an overview of the solutions for auxiliary power supplies in medium voltage converters, this chapter discusses further the potential and advantages of using IPT technologies over the state of the art existing prototypes. In addition, the design objectives and design space of IPT system are discussed in detail.

2.1 External Auxiliary Power Supply

The external APS needs to be galvanically isolated and has to offer high insulation capability reaching the converter system voltage level. The commonly used solutions are the current transformer, voltage transformer, the solution based on IPT and fiber optic.

2.1.1 Current transformer

The solution based on current transformer connects multiple loads to one common source on the primary side. The current transformer is realized by using only one cable passing through the center of different cores, and mounting secondary windings on each cores [51]. An example is shown in **Fig. 2.1b**, the current transformer [52] consists of a basic unit and supply several galvanicaly isolated outputs with only one AC bus current loop in the primary side. The basic unit, referring to the primary side of the system, is supplied with a DC voltage and generates a trapezoidal current at 18 kHz. The AC current is monitored and controlled within the tolerance band [53]. Based on the same current transformer concept, the HPE laboratory at ETH proposed a modularized auxiliary power supply based on current transformer to supply auxiliary power to MMC [54] as shown in **Fig. 2.1c**. Rectifier unit containing ring cores are mounted on each submodule. The AC bus as the primary winding goes through the center of the ring cores. The coupling between adjacent secondary windings, as shown in **Fig. 2.1d**, can optimize output voltage stability. To achieve the requirements for insulation between primary and secondary windings of over 20 kV, the dielectric material potting are used on the secondary winding instead of primary AC bus.

One drawback of the current transformer solution is that the current transformer occupies large volume due to the high insulation requirement, since the high voltage cable and the size of the toroidal core represent essential criterion determining the partial discharge strength of the system. In addition, this solution reduces the flexibility of system and the parts can not be quickly disconnected and replaced.

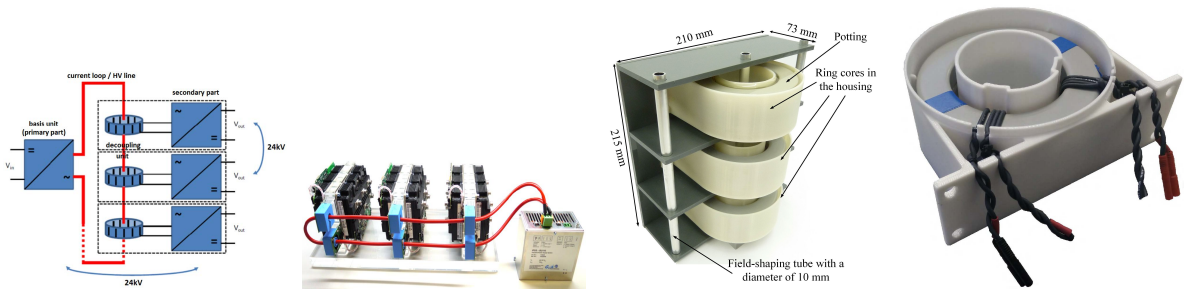

(a) (b) (c) (d)

Fig. 2.1 Current transformer prototypes (a) functional principal [52] (b) product from GVA company as IGBT drivers [52] (c) design in HPE Lab without coupling windings [54] (d) design in HPE Lab with coupling windings [55].

2.1.2 Voltage transformer

Voltage transformer based high insulation power supply has been on market since the beginning of this century. The primary and secondary windings are potted together to offer high insulation capability as the power supplies from the Siebel Elektronik and GVA power shown in **Tab. 2.1**. This solution has high power conversion efficiency because the transmitter and receiver could be brought close due to high electric strength of the solid dielectric material in between [56]. Authors in [22] paid special attention to reduce the electric field enhancements by using field guidance geometry, such as bending the coils to bowl shaped profile and using conductive coatings. As a result, the PD free voltage is 67 kV AC and can operate with system voltage up to 36 kVrms. In summary, due to the rather close distance between primary and secondary coils, the power transfer efficiency of HV isolated transformer system are usually above 90% as shown in **Tab. 2.1**. However because of the potting material, the voltage transformer solutions are usually heavy and bulky.

2.1.3 Inductive power transfer

Inductive power supply has been used in various fields for its mechanical flexibility from low power charger for bio-medical implants to high power charger for home and industry appliances. As discussed in **Sec. 1.3**, in addition to its flexibility and therefore convenience, IPT can also offer high insulation capability. In 2015, ABB proposed the air core IPT technology used as APS for MV converters [57] as shown in **Tab. 2.1**. From that time, multiple IPT prototypes as power supply with high insulation capabilities have been made with different coil structures, compensation networks, insulation material, etc. [22], [23], [58]. Several representative IPT APS for MV converters prototypes with their design specifications are shown in **Tab. 2.1**.

In most IPT systems, the coils are exposed in air and air is the only insulation barrier between the high voltage coil and low voltage coil. Because of low dielectric strength of air, a large air gap is usually required to withstand high voltage, and this large distance between coils usually leads to less compact system and cause low power transfer efficiency [49], [50], [57], [58]. For example, in [49], the air gap is 50 mm to withstand the converter voltage of 6.6 kV. Even though the overall coil size is relatively large $300 \times 150\text{mm}^2$, the transmitting efficiency is only 46.9%. However, the efficiency can be increased by optimizing coil geometries. The solution from ABB uses solenoid coil, and the air gap between the outer primary coil and secondary coil is 75 mm [57], the maximum efficiency

	Siebel Elektronik	GVA power	ABB	ABB
Potted core transformer				
Number of input channels	1	1	1	1
Number of output channels	1 or 4	2	1	1
Input voltage	230 V AC or 24 V DC	24 V DC	110 V DC	220 V DC
Output vltage	35 V DC or 35 V AC	35 V DC	105 V DC	130 V DC
Max output power per channel	150 W	150 W	250 W	250 W
Insulation type	solid dielectric	solid dielectric	solid dielectric	solid dielectric
Insulation voltage (PD-free)	75 kHz	-	200 kHz	400 kHz
Resonant frequency	PD free at 18 kV AC	PD free at 21 kV AC	PD free at 67 kV AC	PD free at 100 kV AC
Coil link Efficiency	>90%	>90%	90% -95%	90% -95%

	ABB	Nagaoka Uin. of Tec.	CPES	Uni. Texas
IPT		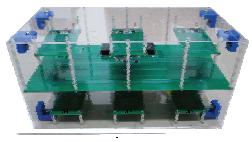	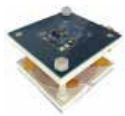	
Number of input channels	1	1	1	1
Number of output channels	1	6	1	1
Input voltage	48V DC	24 V DC	48 V DC	12 V DC
Output vltage	25 -28 V DC	4.5-15 V DC	42-52 V DC	10-15V DC
Max output power per channel	30 W	16.6 W	100 W	100 W
Insulation type	air	air	air	solid dielectric
Insulation voltage (PD-free)	850 kHz	2 MHz	1 MHz	4 MHz
Resonant frequency	-	designed at 6.6 kV AC	PD free at 23 kV AC	breakdown at 25 kV AC
Coil link Efficiency	< 85%	< 46.9%	78 - 92.78%	< 75%

Tab. 2.1 Reported transformer and IPT prototype solutions for APS in MV converters. 1. Siebel [59]; 2. GvA [60]; 3,4. ABB [22]; 5. ABB IPT solution[57]; 6. Nagaoka University of Technology [49]; 7. CPES, Virginia Tech [21]; 8. University of Texas [61].

could reach 90%. Design in [62] has an air gap of 34 mm between primary and secondary coils, the maximum efficiency is 92.78%.

2.1.4 Power over fiber

Due to its high galvanic insulation and low EMI sensitivity, light is another way to supply auxiliary power to medium voltage converter. The optic link can be via optic fiber or via air. Power over fiber (PoF) provides power to a remote location with the transmitter (laser light), an optical fiber and a photo-voltaic power converter at the receiver end. PoF system has been used since the 1990s in power field for instance supplying power to the HV current sensors [63]. PoF has very low parasitic capacitance makes it particularly interesting for gate driver supply solution for wide band gap devices. Until recently, the power transmitted per optic fiber is limited to 10 W and makes it hard to be used

(a) (b) (c)

Fig. 2.2 Power over fiber products (a)250 mW PoF platform from MH GoPower Co. Ltd. [70] (b)(c) 2W laser and 50% conversion efficiency optical power converter from Broadcom Inc [71], [72].

as APS for high power converters [64]. The commercially available PoF platform is up to 1 W and is shown in **Fig. 2.2**. Recently, the advances in laser diode [65] and multi-juction solar cell technology [66] have been made. The photovoltaic power converter reaches the conversion efficiency over 60% [67]. In the optimistic future, the power and voltage level of PoF could be increased and the cost could be reduced. By splitting, manipulating and controlling the light beam [68], PoF has the potential to be used to offer auxiliary power to multiple PEBBs. However, with the current technology, using PoF as APS still has the problem of high cost, power limitation and relatively low efficiency when compared to current transformer solutions [69].

Optical wireless power transmission (OWPT) refers to a laser light beam directed in a straight line over air towards a receiver [73], [74]. Due to the safety concerns of the objects and persons in the beam path, this technology has not been widely used in civil applications. As one of the wireless power transfer technology, the efficiency of OWPT over a short distance is much lower than the other wireless power transfer technologies, and instead it exhibits high efficiency in the far field (> 1 m) power transfer comparable to radial frequency technology. However, for the APS inserted in MV converters, the power is still transferred in the near field. Besides safety concern and low efficiency, the strict requirement on alignment of transmitter and receiver is also a challenge for using OWPT as APS.

2.2 Design Space of IPT Systems

The objective of this thesis is to design and optimize the coil link in the design space following several design objectives. Design space defines all of the possible design alternatives, including winding structure, ferrite geometry and material, as well as converter level topology and compensation network design.

2.2.1 Coil structure

Different coil shapes have been used in IPT systems for various applications. The most common used IPT coil structure have thin plates in view of practical designs. Depending on the location of windings, these planar structures are divided into two types: single-sided and dual-sided [75], [76]. The coil's location influences the magnetic flux distributions. Solenoid windings are commonly utilized as a dual-sided solution, as illustrated in **Fig. 2.3a** with two parallel solenoid windings positioned on

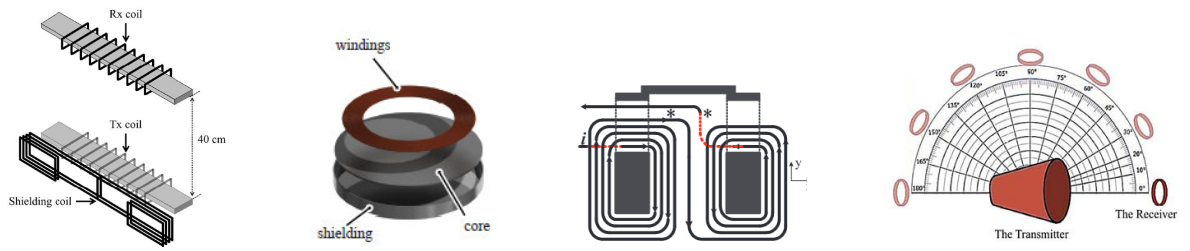

(a) (b) (c) (d)

Fig. 2.3 Different winding layouts (a) solenoid winding [77] (b) planar winding [80] (c) DD winding [81](d) conical winding [82]

ferrite bars [77]. The solenoid windings with the ferrite bars inside form a loosely coupled system and as a double-sided system, it has large leakage flux [78], [79]. The system shown in **Fig. 2.3a** has an air gap of 400 mm, solenoid coil 500 mm long and 60 mm wide and only reaches 0.09 coupling factor. In practice, the solenoid winding is preferable in the application which is sensitive to coil misalignment such as electric vehicle charging system because there is no zero coupling position in dual-sided winding structure [78].

Single sided planar coil systems have spiral winding placed on one side of the ferrite plate and the winding may be structured in circular, square or segmented shapes [83], [84]. Single sided planar coils are appropriate for small distance IPT applications such as inductive heating [85], domestic appliance charging [46], EV charging [80]. Authors of [80] compare the efficiency among circular shape, square shape, rectangular shape and segmented shape windings. Results show that a circular winding of the same area has the best coupling. The single-sided coil is less tolerant to misalignment, however additional winding can be used to overcome this drawback. The DD winding, as shown in **Fig. 2.3c** has two winding connected in series magnetically and achieves high flux path height which is proportional to half of the length of the winding pad [84]. DD layout is preferable for misalignment tolerance, therefore is used in dynamic charging systems such as EV charging [84], [86].

Other winding shapes designed for specific application scenario usually possesses low power density, such as crossed coils in [87] for arbitrary direction power transfer. In addition, in some applications, the flat coil structure is not preferred any more. For example, conical winding design as shown in **Fig. 2.3d** based on the idea of wave reflection could get high magnetic flux concentration [82]. When comparing to planar winding structure, the conical coil has larger and wider magnetic field from the top radius of the conical winding, which is useful in multi pick-up systems. However for the APS application, conical structure is not preferable because conical structure occupies relatively large volume. In the long distance IPT system, one or two intermediate coils can be added on the receiver or the transmitter plate, the link efficiency can be improved [88].

Since the space for APS is limited, firstly the structure which meets physical requirements of APS should be selected. Secondly, the big misalignment will not happen in an APS for MV converters because the APS is installed at a fixed position. Therefore, the maximum misalignment due to inaccurate positioning during installation should be less than 5 mm. When comparing the coil layouts mentioned above, the planar coil structure with single-sided circular shape winding could be a preferable solution.

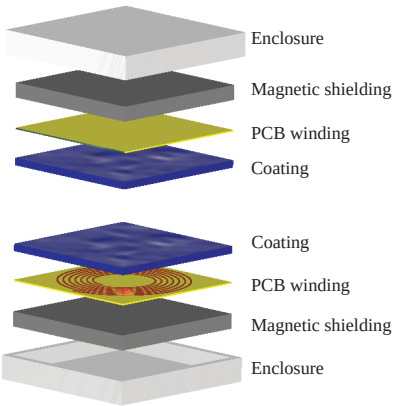

Fig. 2.4 A coil system containing PCB winding, ferrite plate, enclosure and the dielectric coating.

2.2.2 Winding construction

Besides the coil layout, the coil winding construction have several options. Stranded litz wire, solid wire and hollow copper wire have been used in high frequency applications [79], [89]. Skin effect and proximity effect should be taken into account in high frequency operation design. Skin effect loss could be reduced by using litz wire with diameter less than one fourth of skin depth. In addition, the proximity effect at the bundle level can be canceled by twisting litz wires. However, the proximity effect at strand level can not be ignored and can cause larger AC losses than solid conductor at high frequency above 500 kHz [90], [91] and can induces larger losses than hollow copper tubes at frequencies higher than 100 kHz [92]. PCB coil, even though shows higher loss at high frequency, can be easily manufactured and quality control is easier. Therefore PCB coil is selected as the coil solution and the final coil structure is shown in **Fig. 2.4**. The coil system under exploration is composed of winding, magnetic shielding, enclosure and dielectric encapsulation. On the back side of the PCB winding, ferrite is added to increase the coupling factor between two coils. Both the PCB winding and ferrite are fixed in an enclosure.

2.2.3 Magnetic shielding material

Ferromagnetic material on the backside of planar coils provides low magnetic reluctance path behind coils and therefore can achieve better coupling performance between coils by reducing leakage flux. Characteristics of different material are illustrated in **Tab. 2.2**. Ferrite is widely used in high frequency applications (> 25 kHz) due to its low eddy current loss thanks to its low conductivity. Moreover, the low saturation point is not a problem for large air gap IPT systems. Besides ferrite, nanocrystalline ribbon cores have been recently used in 85 kHz IPT systems [93]–[95], however when comparing with ferrite cores, in these researches nanocrystalline shows higher eddy current losses due to its high conductivity. In addition, due to the anisotropic electromagnetic properties of nanocrystalline core, the nanocrystalline core losses could be 20% higher than ferrite core [95] at 85 kHz. Moreover, even though nanocrystalline core has higher permeability, it has small effect on mutual and self inductance because of the large air gap between primary and secondary coils in IPT system and also due to the counter-effect of the eddy current induced in nanocrystalline weakening the linkage flux. Consequently, ferrite is taken as the magnetic shielding material on the backside of the coils. Its effects on the power transfer efficiency is analyzed in **Chap. 5**.

Tab. 2.2 Ferromagnetic material characteristics

material	saturation B	Initial permeability	Conductivity	Frequency
Silicon steel	$0.8 \sim 2.2T$	$< 10 \cdot 10^4$	$\sim 10^7$ S/m	<1 kHz
Amorphous alloy	$0.5 \sim 1.6T$	$< 5 \cdot 10^4$	$\sim\sim 10^3$ S/m	<25 kHz
Nanocrystalline alloy	$1 \sim 1.2T$	$< 10 \cdot 10^4$	$\sim 10^4$ S/m	<25 kHz
Ferrite	$0.3 \sim 0.5T$	$<2 \cdot 10^4$	$\sim 10^-5$ S/m	>25 kHz

2.2.4 Magnetic shielding shape

Ferrite shapes in IPT coils are derived from magnetic core structure including pot core [80], [96], [97], U core [98], [99], and E core [45], [46]. And these core shapes can be used with planar spiral coils as shown in **Fig. 2.5**. The E core is widely used in the transmitter coil as charging rail for autonomous machines [46]. The U core is usually used with double D winding structure [98]. The pot core can be used with spiral winding on one side of it [80]. Besides these magnetic core types, ferrite plates are widely used in IPT technology due to its easy manufacturing and implementation. In this thesis, the ferrite plates will be used and different surface shapes including rectangular shape, round shape and strip bars as shown in **Fig. 2.6** will be compared and analyzed in the following chapters.

For the planar IPT system as shown in **Fig. 2.4** where power is transferred through loosely coupled contactless coils, when ferrite is added on the backside of coils, the magnetic flux density distribution is inhomogeneous in the contactless coupling coils. Based on the selected ferrite plate shape, the quantitative model of ferrite effect to the planar coil system is needed in designing the IPT system and will be discussed in this thesis.

2.2.5 Multiple outputs IPT structure

In one modular converter, there could be multiple PEBBs stacked together. As shown in **Fig. 2.7**, the solutions to supply all these PEBBs could be "distributed solution" where each PEBB is separately energized from different IPTs and converters, such as the solutions in [21], [57], [61], or the "centralized solution" where the APS for each PEBB is connected through one single primary side converter. The centralized solution requires a single centralized converter instead of multiple converters at the input stage, and consequently saves space inside the main power converter. In the centralized solution, the primary coils could be one integrated coil as shown in solution 6 in **Tab. 2.1** [49] or multiple coils. The primary multiple coils connecting in series bring more flexibility to the system.

This thesis will work on the topology that possesses multiple secondary coils and connecting multiple

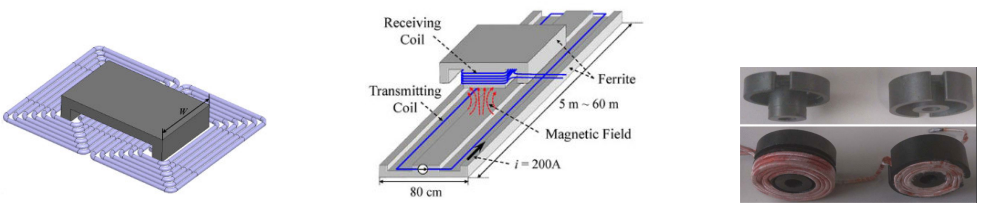

(a) (b) (c)

Fig. 2.5 Different ferrite shapes (a) U shape [98] (b) E shape [46] (c) pot shape [96]

primary coils in series as shown in **Fig. 2.8**. L_p and L_s stand for the primary and secondary self inductance. M is the mutual inductance. On both primary and secondary side, there is equivalent series resistance coil resistance represented by R_p and R_s. This system consist of one primary side converter, one primary compensation network, multiple primary coils, multiple secondary coils, multiple secondary side compensation network and multiple secondary side converters. The primary side converter outputs the high frequency square wave, and through the compensation network, a constant high frequency current is obtained on the primary coil. The secondary coil and secondary compensation components compose a network to output constant high frequency voltage which will then be rectified to DC voltage and provided to PEBB. Each part of the IPT system needs to be designed to achieve a optimal system and will be discussed in the following sections.

2.2.6 Inverter

In the primary side of IPT system, an inverter is needed to convert DC power into high frequency AC power. Four basic inverter topologies are shown in **Fig. 2.9**. The inverter is connected to a compensation network at its output and composes a resonant inverter. Voltage and current inverters work with different compensation networks. In the high frequency applications, zero-voltage-switching is desired and this is ensured by the resonant topology and appropriate duty cycle. Further discussion together with compensation network is included in **Chap. 3**.

2.2.7 Rectifier

At the secondary side of the IPT link, a rectifier is usually implemented to convert the received AC power to DC power to be used by the electronic systems later (the load). Diodes are usually used in rectifier topologies due to its simplicity and its negligible disturbance on the secondary resonance topology. In the low voltage high frequency IPT system, the Schottky diodes exhibit an advantage of low switching loss due to no reverse recovery currents, and exhibits low forward voltage.

The four basic rectifier topologies with voltage source behavior are shown in **Fig. 2.10**. In a half wave rectifier as shown in **Fig. 2.10a**, the current is drawn only at positive peaks of the input voltage. Full wave rectifier as shown in **Fig. 2.10b** and **Fig. 2.10c** in contrary draws current at both positive and negative peaks. Due to lower cost and space, half wave rectifiers such as class D and class E are widely used in high frequency applications >1 MHz [100]. An inverse coupled current doubler rectifier as shown in **Fig. 2.10c** outputs half of the input voltage and two times of the input current and is attractive solution for output current applications [101].

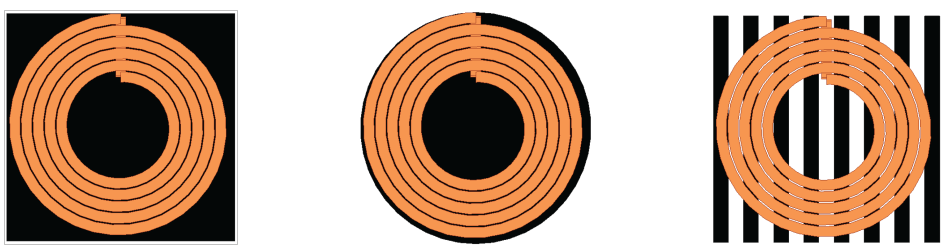

(a) (b) (c)

Fig. 2.6 Same windings with different planar ferrite shapes (a) rectangular shape (b) round shape (c) strips.

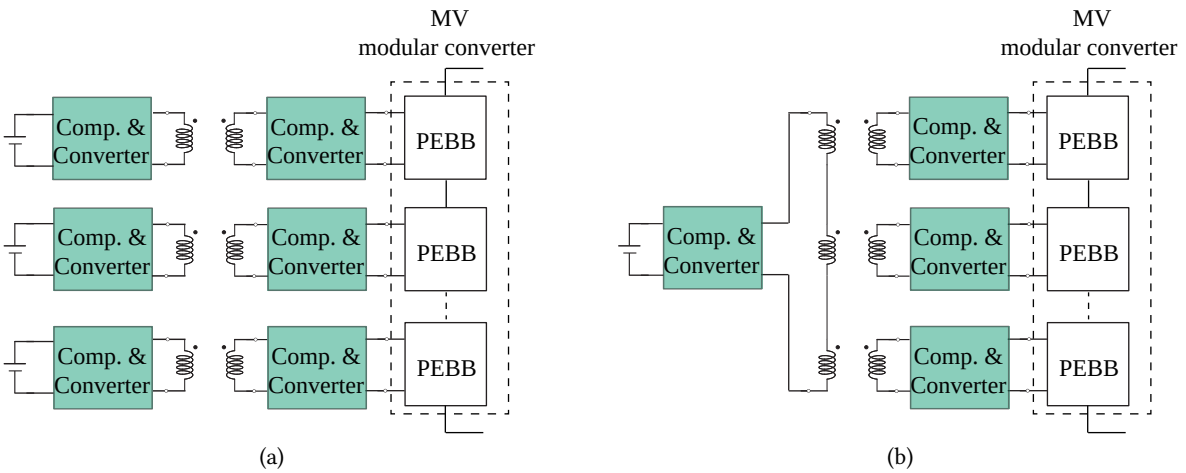

Fig. 2.7 Different solutions for multiple outputs (a) distributed solution (b) centralized solution.

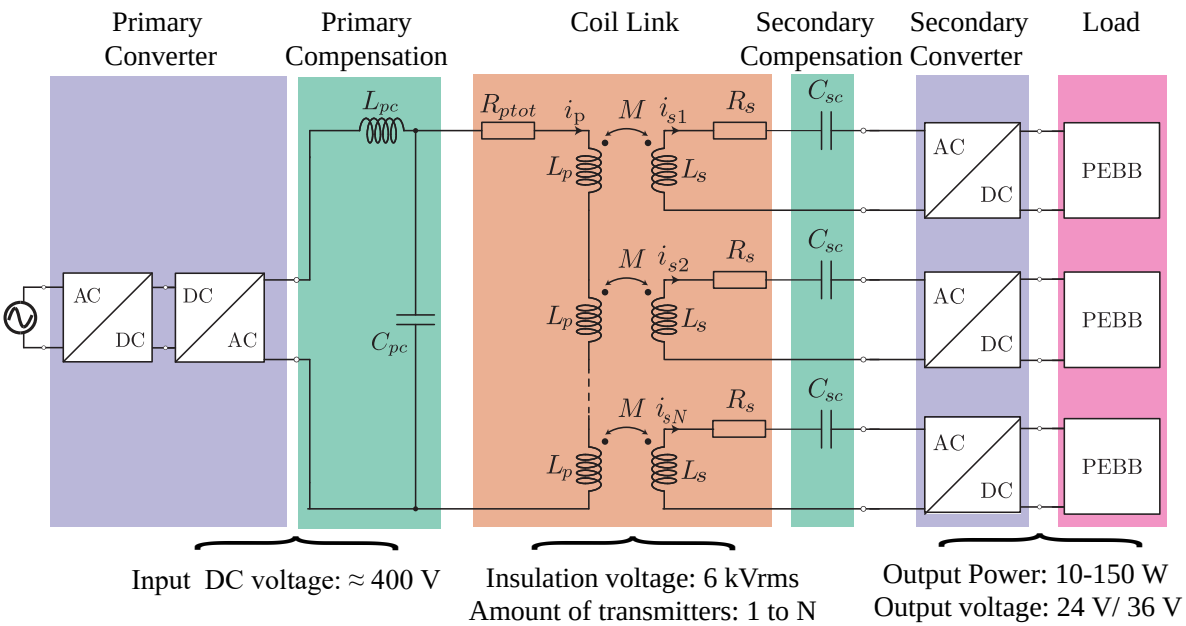

Fig. 2.8 Centralized IPT structure followed in this thesis.

In this thesis, the demanding output current is low and the switching frequency is considered to be below 1 MHz, therefore the full wave rectifiers including HB and FB topologies are considered. The optimization design based on both topologies will be done and discussed in the following chapters.

2.2.8 Compensation network

In order to improve the power efficiency of a coil link, compensation networks are usually added in an IPT system. On the secondary side, a compensation capacitor can be placed in parallel or in series with the secondary coil which will result in different power transmission ratios. The primary coil and primary compensation capacitor on the primary side form a resonant tank which converts

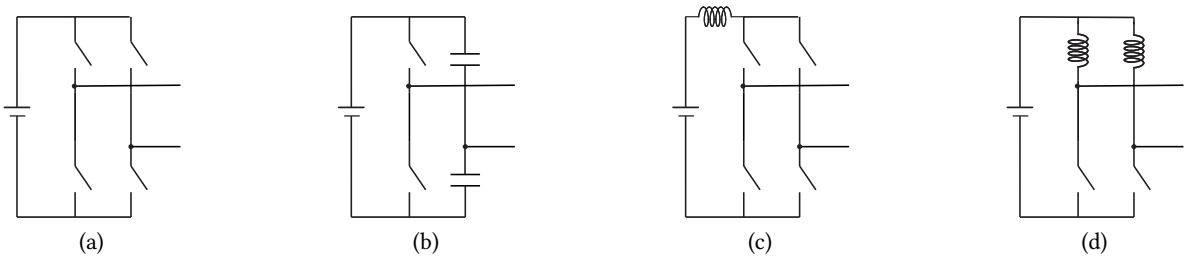

Fig. 2.9 Different inverter topologies (a) Voltage fed FB rectifier (b) Voltage fed half bridge (HB) rectifier (c) Current fed FB rectifier (d) Current fed HB rectifier (with current doubling).

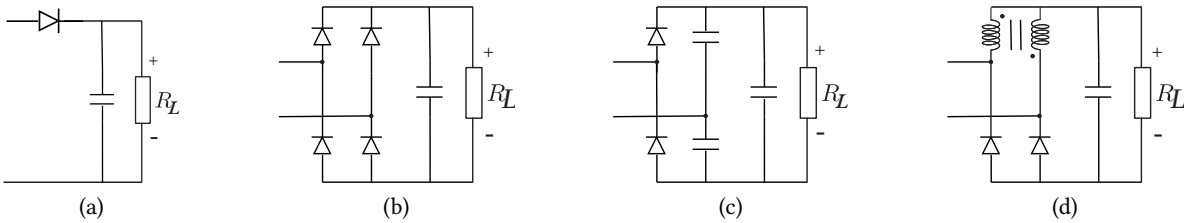

Fig. 2.10 Different rectifier topologies with voltage source behavior (a) Half wave rectifier (b) Full wave FB rectifier (c) Full wave HB rectifier (with voltage doubling) (d) Inverse coupled current doubler rectifier .

square wave voltages into sinusoidal waveform at the resonant frequency. The primary side could work as a constant voltage source or a current source depending on the primary side inverter and compensation topology.

The four basic compensation networks are shown in **Fig. 2.11**. Even though the basic compensation topologies are simple, for some desired performance, hybrid compensation topologies are preferred. As a power supply for MV converters, as shown in **Fig. 2.8** the IPT system needs to offer constant output voltage to multiple PEBBs. As the APS for PEBBs, IPT system has independent outputs to make sure that when one PEBB changes its operating conditon, other PEBBs are supplied normally from APS. The output of each receiver coil should be independent of PEBB conditions of other receivers. By careful selection of compensation networks and design of capacitors and inductors, IPT can be operated as a transformer with a load independent voltage ratio without control loop. In the single output coil structure, the compensation technique by inserting capacitors in series into both primary coil and secondary coil known as the S-S compensation are adopted in [22], [57], and the output voltage variation is within 2%. However, if there are multiple outputs, the S-S compensation network can not ensure independent work among all the outputs. LCL-S compensation network as shown in the **Fig. 2.8** is a hybrid compensation topology which has an inductor in series and a capacitor in parallel with primary coils and a capacitor placed in series with secondary coil. LCL-S compensation network can be adopted to achieve independent multiple outputs [61]. The characteristics of four basic compensation networks as well as the advantage of using LCL-S compensation topology will be discussed further in **Chap. 3**.

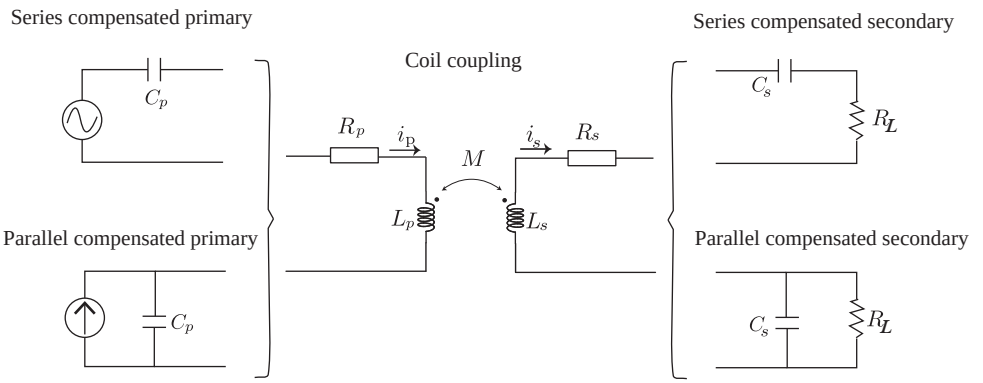

Fig. 2.11 IPT coil pair with four basic compensation networks.

2.3 Design Objectives and Constraints

As for most power supplies, optimization goals of the IPT based APS are to achieve high efficiency and high power density. In addition, in the design of the APS system in MV converters, special considerations should be made to insulation and thermal coordination.

2.3.1 High efficiency and high power density objectives

As shown in **Fig. 2.8**, the losses in the IPT system come from the losses on coils, losses due to the parasitic resistance of compensation network components, and losses on primary and secondary converters. A high operation frequency leads to a high power transfer efficiency from the transmitter coil to the receiver coil [102]. In addition, the high operating frequency allows to reduce the size of inductors and capacitors. However, the losses on the other components in the IPT system introduced by high frequency should be taken into consideration during the design of IPT system. The frequency bands where most of IPT systems operate are from 20 kHz to 13.56 MHz [103]. The lower frequency range from 20 kHz to 100 kHz are used in IPT system transferring kW power and are normally used in electric transportation. In 2014, Task Force J2954 of SAE (Society of Automotive Engineers) agreed that the 85 kHz band should be selected for electric vehicles based on the current usage status of plural candidate frequency bands as well as compatibility with other radio systems. Above 1 MHz, IPT systems are normally used for charging consumer devices and transfer typically below 5 W. The frequency range 6.78 MHz ± 15 kHz is recommended by global and local regulatory recommendation groups such as Airfuel Alliance [104] and Wireless Power Consortium [105] for consumer devices, and this is a specially designated industrial scientific medical (ISM) band. The band of 13.56 MHz ± 7 kHz is one of emerging band for medical and mobile devices [106]–[108]. For the power range below 200 W and above 5 W, the frequency range from 100 kHz to 1 MHz are usually used [103], and in this thesis, the optimization is done in this frequency range.

Even though the losses are distributed in all the components of IPT system, most of losses occur on the coil link. In the primary side inverter, achieving zero voltage switching is expected [50] on semiconductor devices because the semiconductor devices work under high voltage and high frequency. Consequently, most losses appear on coils, and these losses are influenced by the quality factor of each coil which is the ratio between the inductance at a frequency and the resistance of the coil $Q = \frac{wL}{R}$. In addition, the coupling factor which is the ratio between mutual inductance and self

inductance $k = \frac{M}{\sqrt{L_p L_s}}$ influences the coupling efficiency between two coils. Quality factor together with coupling factor determines the coil link power transfer efficiency. Under the same distance, coil geometry should be optimized to achieve high Q and k [21].

2.3.2 Insulation coordination

In an IPT system, the distance between primary and secondary coil determines the coupling performance of the system and therefore influences the power transfer performance. The smaller the distance, the better the coupling performance, therefore the distance should be as small as possible to obtain optimal system. On the other hand, the insulation capability of the IPT system is determined by the distance and the larger the distance, the higher the insulation capability. In order to reach the MV converter system insulation level, the shortest distance should be determined and is one design constraint that should be respected. Under the same insulation level requirement, the minimum distance is also influenced by the dielectric material implemented in the coil system. In order to keep the flexibility of the IPT system and keep the primary and secondary coils separable, the air is used as the basic insulation barrier. And the shortest distance between coils is determined based on the dielectric characteristic of air. In this thesis, the minimum distance is defined following insulation coordination in IPT system.

2.3.3 Thermal coordination

The heat in a system is dissipated to the surroundings via three ways: convection, conduction, and radiation. In order to keep the normal functionality of the components in the APS system, the hottest temperature inside each component should be kept under a certain level, therefore the thermal coordination needs to be considered in the design process. The thermal network considering convection, conduction and radiation effects are useful to model the thermal dissipation capability and to predict the temperature inside the system. As shown in **Fig. 2.4**, in the IPT system, the convection happens on the top, bottom and side surfaces contacting air. The conduction happens in the copper coil, FR4 PCB material, ferrite, solid dielectric layer and the box walls. The thermal radiation happens on the surfaces and can be calculated [109], [110] in nonlinear form.

The thermal dissipation is widely researched in the high power application such as EV [111]. For IPT as APS system, small surface area and dielectric encapsulation bring more challenges to the thermal coordination. The thermal model can be obtained by FEM and thermal network method (TNM). Thermal FEM needs the supporting of computational fluid dynamics to extend the constant convection coefficients on the boundary with an explicit simulation of the fluid flow around the object and it is computationally expensive. TNM sacrifices modeling accuracy with fast modeling speed. But for the symmetrical geometry, the accuracy with TNM is relatively high. In addition, comparing to FEM, TNM model is easier to be integrated in the optimization flow. In this thesis, a generalized TNM for various coil geometries and materials is proposed and is integrated into the optimization flow to predict the thermal performance of coil pairs.

2.4 Summary

Because of its contactless nature between primary and secondary winding, IPT has great potential in high insulation applications such as APS in MV converters. However, large insulation distance brings

challenges to design a system with high power transmission efficiency and power density. Therefore, the IPT coil link structure needs to be optimized to achieve high transmission efficiency and power density, while meeting the insulation requirements, stable output voltage and thermal requirements.

Different design choices of IPT system are discussed in this chapter. Planar coil structure, PCB winding together with system structure shown in **Fig. 2.8** are selected as the basis for further discussion in this thesis. The other free parameters, including compensation networks, winding geometry parameters and magnetic shielding shape, will be discussed in the following chapters.

High efficiency and high power density for IPT system with any given electric specifications can only be achieved if a systematic design optimization framework is established and supported by advanced modeling. However, modeling and optimization of IPT systems is a complex task. Firstly, the large fringing field in IPT systems leads to complex modeling. Secondly, many degrees of freedom in the components in an IPT system are multi-physically coupled in a non-linear way, including compensation network, winding design, magnetic shielding design, thermal design and insulation design, etc.. In the following chapters, the optimization of an PCB based multiple outputs IPT coil link is demonstrated part by part.

3
Compensation Network Design

Based on four basic compensation networks, according to the design goal of achieving independent operation among secondary sides in APS of PEBBs, the hybrid LCL-S compensation network is further discussed in this chapter. The systematic design approach of the LCL-S compensation network to achieve the optimization goal is discussed. In addition, the impacts of operating parameters on the system efficiency are explored.

3.1 Compensation Networks

An inductive link with only two coils can transfer certain amount of power over a distance, however in order to transfer the maximum amount of power within the system constraints, the compensation capacitors are usually added in addition to the coils to reduce the reactive power on the primary and secondary sides [112]. In a coil link, the compensation network design should follow some rules to achieve the optimal IPT link. In this section, four basic compensation networks shown in **Fig. 2.11** are reviewed and explained.

3.1.1 Equivalent model

The link of the primary and secondary coil is shown in **Fig. 3.1**, where 'p' and 's' represent primary and secondary, respectively. L_p, L_s are self inductance of primary and secondary coils, respectively. R_p and R_s represent the resistance of coils. M is mutual inductance between the primary and secondary coil. The characteristic equations of this coil pair is:

$$\begin{aligned} V_p &= (j\omega L_p + R_p) \cdot I_p - j\omega M \cdot I_s \\ V_s &= -(j\omega L_s + R_s) \cdot I_s + j\omega M \cdot I_p \end{aligned} \tag{3.1}$$

From (3.1), we can get current controlled voltage source equivalent model shown in **Fig. 3.2**. The current controlled voltage source represents the coupling effect between primary and secondary coils.

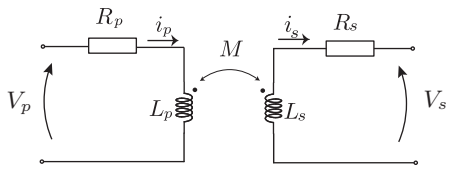

Fig. 3.1 Primary and secondary coils with self inductance L_p, L_s, parasitic AC resistance R_p, R_s, and mutual inductance M.

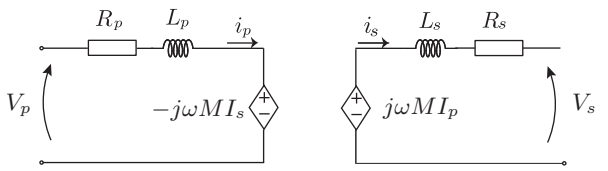

Fig. 3.2 Equivalent model with current controlled voltage source.

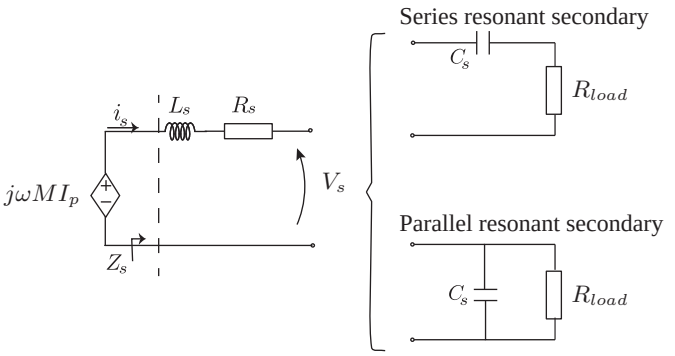

Fig. 3.3 Secondary compensation topologies with series connected capacitor and parallel connected capacitor.

3.1.2 Design of secondary compensation networks

Two secondary compensation topologies are shown in **Fig. 3.3**. In the following discussion, the characteristics of secondary sides with series compensation network and parallel compensation network are derived separately. And the optimization is later discussed on both topologies together.

3.1.2.1 Series compensation on the secondary coil side

As shown in **Fig. 3.3**, the input impedance of the secondary side is composed of secondary coil, the compensation network and load. With series compensation topology on the secondary side, the input impedance of the secondary is

$$Z_s = j\omega L_s + R_s + \frac{1}{j\omega C_s} + R_{load} \tag{3.2}$$

The coupling effect is represented by current controlled voltage source in **Fig. 3.2**. Further simplification could be done by replacing the voltage source by the reflected impedance on the primary side. Seen from the primary side, the secondary impedance will reflect to the primary side as shown in **Fig. 3.4** and the reflected impedance can be calculated.

This reflected impedance is dependent on the coupling and operating frequency

$$Z_r = -j\omega M \frac{j\omega M}{Z_s} = \frac{\omega^2 M^2}{Z_s}. \tag{3.3}$$

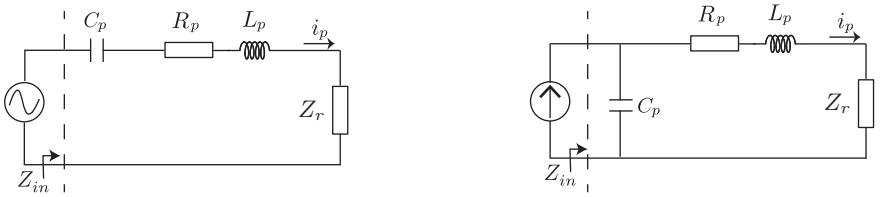

Fig. 3.4 Equivalent circuit of the primary side with reflected secondary impedance (a) series compensation primary (b) parallel compensation primary.

For series compensation secondary, the reflected impedance to the primary is

$$\begin{aligned}\mathfrak{Re}\,(Z_r) &= \frac{\omega^4 C_s^2 M^2 (R_s + R_{load})}{(\omega^2 C_s L_s - 1)^2 + \omega^2 C_s^2 (R_s + R_{load})^2} \\ \mathfrak{Im}\,(Z_r) &= \frac{-\omega^3 C_s M^2 (\omega^2 C_s L_s - 1)}{(\omega^2 C_s L_s - 1)^2 + \omega^2 C_s^2 (R_s + R_{load})^2}\end{aligned} \tag{3.4}$$

In most cases, secondary coil resistance R_s is much smaller than the load R_{load}, the equations above are simplified to

$$\begin{aligned}\mathfrak{Re}\,(Z_r) &= \frac{\omega^4 C_s^2 M^2 R_{load}}{(\omega^2 C_s L_s - 1)^2 + \omega^2 C_s^2 R_{load}^2} \\ \mathfrak{Im}\,(Z_r) &= \frac{-\omega^3 C_s M^2 (\omega^2 C_s L_s - 1)}{(\omega^2 C_s L_s - 1)^2 + \omega^2 C_s^2 R_{load}^2}\end{aligned} \tag{3.5}$$

Assuming a constant current on the primary side, the resonance network on the secondary could work at amplitude resonant frequency ω_{resA} which is defined as the frequency when $\mathfrak{Re}\,(Z_r)$ is at its maximum value. In this case, there is highest power delivered to secondary side. The amplitude resonant frequency for series compensated network is

$$\omega_{resA} = \frac{1}{\sqrt{C_s L_s}} \tag{3.6}$$

The resonance network can also work at the phase resonant frequency ω_{resP} , which makes the reflected secondary impedance Z_r real and phase angle equal to zero, i.e. $\mathfrak{Im}\,(Z_r) = 0$. Operating at phase resonant frequency makes the reflected impedance Z_r purely resistive regardless of coupling and load variation. For series compensated secondary, phase-resonant frequency corresponds to the amplitude-resonant frequency.

$$\omega_{resP} = \omega_{resA} = \frac{1}{\sqrt{C_s L_s}} \tag{3.7}$$

Under this frequency, the capacitor fully compensates secondary inductance. The input impedance of the secondary side is purely resistive.

$$Z_s = R_{load} + R_s \tag{3.8}$$

Since the capacitor fully compensates the secondary coil self inductance, the current passing through load is

$$I_{load} = I_s = \frac{j\omega M I_p}{Z_s} = \frac{j\omega M I_p}{R_{load} + R_s} \tag{3.9}$$

The voltage across the load is:

$$V_{load} = I_{load} R_{load} = j\omega M I_p \frac{R_{load}}{R_{load} + R_s} \tag{3.10}$$

It can be seen that, the current through the load changes with the load variation, while the voltage across the load keeps relatively constant regardless of load change by supposing a small secondary coil resistance R_s.

3.1.2.2 Parallel compensation on the secondary coil side

As shown in **Fig. 3.3**, with parallel compensation topology on the secondary side, the input impedance of the secondary is

$$Z_s = j\omega L_s + R_s + \frac{1}{j\omega C_s + \frac{1}{R_{load}}} \tag{3.11}$$

The reflected impedance Z_r to the primary is

$$\begin{aligned} \mathfrak{Re}\left(Z_r\right) &= \frac{\omega^2 M^2 \left(C_s^2 R_{\text{load}}^2 R_s \omega^2 + R_{\text{load}} + R_s\right)}{R_{\text{load}}^2 \left(\omega^2 C_s L_s - 1\right)^2 + C_s^2 R_{\text{load}}^2 R_s^2 \omega^2 + L_s^2 \omega^2 + 2 R_{\text{load}} R_s + R_s^2} \\ \mathfrak{Im}\left(Z_r\right) &= \frac{-\omega^3 M^2 \left(C_s R_{\text{load}}^2 \left(\omega^2 C_s L_s - 1\right) + L_s\right)}{R_{\text{load}}^2 \left(\omega^2 C_s L_s - 1\right)^2 + C_s^2 R_{\text{load}}^2 R_s^2 \omega^2 + L_s^2 \omega^2 + 2 R_{\text{load}} R_s + R_s^2} \end{aligned} \tag{3.12}$$

Considering the coil resistance R_s is much smaller than the R_{load}, the equations above are simplified to

$$\begin{aligned} \mathfrak{Re}\left(Z_r\right) &= \frac{\omega^2 M^2 R_{load}}{R_{load}^2 (\omega^2 C_s L_s - 1)^2 + \omega^2 L_s^2} \\ \mathfrak{Im}\left(Z_r\right) &= \frac{-\omega^3 M^2 \left(C_s R_{\text{load}}^2 \left(\omega^2 C_s L_s - 1\right) + L_s\right)}{R_{\text{load}}^2 \left(\omega^2 C_s L_s - 1\right)^2 + \omega^2 L_s^2} \end{aligned} \tag{3.13}$$

According to the definitions of amplitude resonance and phase resonance, one can get

$$\omega_{resA} = \frac{1}{\sqrt{C_s L_s}} \tag{3.14}$$

$$\omega_{resP} = \sqrt{\frac{1}{C_s L_s} - \frac{1}{C_s^2 R_{load}^2}} = \omega_{resA} \sqrt{\frac{\alpha^2}{1 + \alpha^2}} \tag{3.15}$$

where load factor $\alpha = R_{load}\omega C_s$.

When working at amplitude resonant frequency ω_{resA}, with $X = \frac{1}{\omega C_s} = \omega L_s$, $\alpha = \frac{R_{load}}{X}$. By assuming $R_s \approx 0$. The secondary side input impedance from (3.11) is

$$Z_s = \frac{X^2}{R_{load} - jX} \tag{3.16}$$

The current through the load is

$$I_{load} = \frac{\omega M I_p}{X} \tag{3.17}$$

The voltage across the load is

$$U_{load} = \omega M I_p \alpha \tag{3.18}$$

The output power is

$$P_{out} = \frac{(\omega M I_p)^2}{X}\alpha \tag{3.19}$$

As can be seen from (3.17), the output current is independent of load variation.

When working at ω_{resP}, defining $X = \frac{1}{\omega C_s} = \omega L_s \frac{1+\alpha^2}{\alpha^2}$, $\alpha = \frac{R_{load}}{X}$. The circuit has following characteristics. The secondary side input impedance is

$$Z_s = \frac{R_{load}}{1 + \alpha^2} \tag{3.20}$$

The current through the load is

$$I_{load} = \frac{\omega M I_p}{X}(1 + \frac{j}{\alpha}) \tag{3.21}$$

The voltage across the load is

$$U_{load} = \omega M I_p \alpha + j\omega M I_p \tag{3.22}$$

The output power is

$$P_{out} = \frac{(\omega M I_p)^2}{X}\alpha(1 - \frac{1}{\alpha^2}) \tag{3.23}$$

In order to achieve a constant load current, the load factor is usually designed at $\alpha \gg 1$. Under this approximation, $\omega_{resA} \approx \omega_{resP}$ and the output characteristics are similar.

Tab. 3.1 Reflected impedance with different secondary compensation topologies

Secondary compensation	Amplitude or phase resonance		Reflected impedance to primary side	
Series Secondary	ω_{resA}	$\frac{1}{\sqrt{C_s L_s}}$	$\mathfrak{Re}(Z_r) = \frac{M^2\omega_{resA}^2}{R_{load}}$	$\mathfrak{Im}(Z_r = 0)$
	ω_{resP}			
Parallel Secondary	ω_{resA}	$\frac{1}{\sqrt{C_s L_s}}$	$\mathfrak{Re}(Z_r) = \frac{M^2}{L_s^2 R_{load}^2}$	$\mathfrak{Im}(Z_r) = -\frac{M^2\omega_{resA}}{L_s R_{load}^2}$
	ω_{resP}	$\sqrt{\frac{1}{C_s L_s} - \frac{1}{C_s^2 R_{load}^2}}$	$\mathfrak{Re}(Z_r) = \frac{M^2\omega_{resP}^2 R_{load} C_s}{C_s R_{load} R_s + L_s}$	$\mathfrak{Im}(Z_r) = 0$

3.1.2.3 Link efficiency optimization

Different design of secondary compensation capacitors and the resulting reflected impedance to the primary side is listed in **Tab. 3.1**. In summary, the series resonant secondary works as a voltage source and the parallel resonant secondary works as a current source.

Coil link efficiency η_{link} is defined as the ratio of the power that reaches to the load on the secondary side to the total power input on the primary side, and can be calculated as the multiplication result of primary side efficiency η_p and secondary side efficiency η_s. According to the equivalent circuit with reflected secondary impedance R_r in **Fig. 3.4**, the primary link efficiency, defined as the ratio of the power that reaches the secondary to the total input power on the primary side, can be expressed by the ratio of power P_{sec} dissipated on reflected secondary resistance to the total power P_{in} dissipated on both primary resistance and reflected resistance

$$\eta_p = \frac{P_{sec}}{P_{in}} = \frac{R_r}{R_r + R_p} \tag{3.24}$$

(3.24) is valid regardless of the compensation method of primary side.

Secondary link efficiency is defined as the ratio of the power dissipated on load to the total power that reaches the secondary circuit. For different secondary compensation networks, this efficiency is different. For series compensated secondary, link efficiency can be expressed as a simple resistance ratio, however, for parallel compensated secondary, because C_s shunts R_{load}, the voltage across two resistors is not in phase. For series compensated secondary:

$$\eta_{s-series} = \frac{P_{out}}{P_{sec}} = \frac{R_{load}}{R_{load} + R_s} \tag{3.25}$$

For parallel compensated secondary:

$$\eta_{s-parallel} = \frac{P_{out}}{P_{sec}} = \frac{L_s}{R_{load} C_s R_s + L_s} \tag{3.26}$$

Therefore the total link efficiency is calculated

$$\eta_{link} = \eta_p \eta_s \tag{3.27}$$

3.1.2.4 Optimal operational frequency

As shown in equations (3.24)-(3.26), the link efficiency is only affected by the secondary compensation, and independent of the primary compensation. To calculate the optimal operational frequency, a new factor reflecting the compensation network κ is defined as $\kappa = \frac{1}{\omega^2 C_s L_s}$ [112]. The optimal frequency can be calculated by solving $\frac{\partial \eta_{link}}{\partial \kappa} = 0$. The optimal values of κ for series and parallel compensation on the secondary side are determined as

$$\begin{aligned} \kappa_{opt,*S} &= 1 \\ \kappa_{opt,*P} &= 1 + \frac{1}{Q_2} + \left(\frac{kQ_2}{Q_1}\right)^2 \end{aligned} \tag{3.28}$$

where, Q_1 and Q_2 are the quality factors of primary side and secondary side respectively $Q_1 = \frac{wL_p}{R_p}$ and $Q_2 = \frac{wL_s}{R_s}$. The subscript $*S$ means the primary side can be in any compensation topology while the secondary side is with series compensation. The subscript $*P$ means the primary side can be in any compensation topology while the secondary side is with parallel compensation. From optimal κ, the optimal operational frequency to achieve high efficiency is found at phase resonant frequency. This is because when the compensation network works at phase resonant frequency, reactive power flow is minimized. The optimal frequency when the secondary side adopts series compensation network is

$$\omega_{opt-\eta,*S} = \omega_{resP} = \omega_{resA} = \frac{1}{\sqrt{C_s L_s}} \tag{3.29}$$

The optimal frequency for the parallel compensation on the secondary side is

$$\omega_{opt-\eta,*P} = \omega_{resP} = \sqrt{\frac{1}{C_s L_s} - \frac{1}{C_s^2 R_{load}^2}} \tag{3.30}$$

The efficiency at optimal frequency can thus be calculated respectively for series and parallel compensation topology on the secondary side

$$\begin{aligned} \eta_{link,*S} &= \frac{k^2 Q_1 \alpha}{\left(\alpha + k^2 Q_1 + \frac{1}{Q_2}\right)\left(\alpha + \frac{1}{Q_2}\right)} \\ \eta_{link,*P} &= \frac{k^2 Q_1 Q_2^2}{\left(1 + \frac{Q_2}{\alpha} + k^2 Q_1 Q_2\right)(\alpha + Q_2)} \end{aligned} \tag{3.31}$$

where, α is the load factor defined before as $\alpha = \frac{R_{load}}{wL_s}$. It's noted that the efficiency only depends on the secondary compensation and remains constant no matter how the primary compensation network changes.

3.1.2.5 Optimal load factor

Similar to calculating the optimal frequency, the optimal load factor can be found by solving $\frac{\partial \eta_{link}}{\partial \alpha} = 0$, the η_{link} here is the result from (3.31) which means the link works at optimal frequency. The optimal

load factor and the corresponding efficiency can be calculated

$$\begin{aligned} \alpha_{opt-\eta,*S} &= \frac{\sqrt{1+k^2Q_1Q_2}}{Q_2} = \frac{\sqrt{1+\Lambda}}{Q_2} \\ \alpha_{opt-\eta,*P} &= \frac{Q_2}{\sqrt{1+k^2Q_1Q_2}} = \frac{Q_2}{\sqrt{1+\Lambda}} \end{aligned} \tag{3.32}$$

In the equation above Λ is the variable of merit including both quality factor and coupling factor defined as $\Lambda = k^2Q_1Q_2$ [113]. The optimal efficiency under optimal load factor is found in identical expression for both series and parallel compensated secondary:

$$\eta_{link} = \frac{\Lambda}{\left(1+\sqrt{1+\Lambda}\right)^2} \tag{3.33}$$

From equation (3.33), it can be concluded, to improve the efficiency the increase of Λ is needed, which means to either increase coupling factor k or increase the quality factor Q_1 and Q_2, which can be realized by optimization of coil geometry and operation frequency.

3.1.3 Design of primary compensation networks

As shown in **Fig. 3.4**, the input impedance seen from the primary side is:

$$\begin{aligned} Z_{i,S*} &= \frac{1}{j\omega C_p} + j\omega L_p + R_p + Z_r \\ Z_{i,P*} &= \frac{1}{j\omega C_p + \frac{1}{j\omega L_p + R_p + Z_r}} \end{aligned} \tag{3.34}$$

where subscript $S*$ means the primary side has series compensation network while the secondary side can have compensation network in any form. Subscript $P*$ means the primary side has parallel compensation network while the secondary side can have compensation network in any form. By operating the whole circuit at the zero-phase angle frequency, i.e. $\mathfrak{Im}(Z_i) = 0$, the reactive power flow is eliminated, and VA rating of the power supply is minimized by operating at the zero phase angle frequency.

If the secondary is designed at the phase-resonant frequency, i.e. $\mathfrak{Re}(Z_r) = 0$, the primary capacitance only needs to compensate the primary self-inductance. The primary capacitance is obtained by $\mathfrak{Im}(Z_i) = 0$. The optimal primary capacitance, while secondary is phase-resonant, is shown in **Tab. 3.2**.

If the secondary is designed at the amplitude-resonant frequency, i.e. $\mathfrak{Re}(Z_r) \neq 0$ when secondary side is parallel compensated, the primary capacitance needs to compensate both the primary self-inductance and the reflected impedance. Calculating $\mathfrak{Im}(Z_i) = 0$, the primary capacitance values are listed in **Tab. 3.3**. With these primary capacitance values design, the input impedance seen from the primary side now is pure resistive:

$$\begin{aligned} Z_{i,S*} &= R_p + Z_r \\ Z_{i,P*} &= \frac{R_p + Z_r}{(1-\omega^2 C_p L_p)^2 + \omega^2 C_p^2 (R_p + Z_r)^2} \end{aligned} \tag{3.35}$$

Tab. 3.2 Primary compensation capacitance when working at secondary phase-resonant frequency w_{resP}

Primary and secondary compensation networks	primary compensation capacitor value
SS	$C_p = \frac{1}{\omega_0^2 L_p}$
SP	$C_p = \frac{1}{\omega_0^2 L_p}$
PP	$C_p = \frac{L_p}{(\frac{M^2 \omega_{resP}^2 R_{load} C_s}{C_s R_{load} R_s + L_s})^2 + \omega_0^2 L_p^2}$
PS	$C_p = \frac{L_p}{(\omega_0^2 M^2 / R_{load})^2 + \omega_0^2 L_p^2}$

Tab. 3.3 Primary compensation capacitance when working at secondary amplitude-resonant frequency w_{resA}

Primary and secondary compensation networks	primary compensation capacitor value
SS	$C_p = \frac{1}{\omega_0^2 L_p}$
SP	$C_p = \frac{1}{\omega_0^2 (L_p - M^2/L_s)} = \frac{1}{\omega_0^2 L_p (1 - k^2)}$
PP	$C_p = \frac{L_p - M^2/L_s}{(M^2 R_{load}/L_s^2)^2 + \omega_0^2 (L_p - M^2/L_s)^2}$
PS	$C_p = \frac{L_p}{(\omega_0^2 M^2 / R_{load})^2 + \omega_0^2 L_p^2}$

As shown in **Tab. 3.2** and **Tab. 3.3**, for series compensated primary (SS and SP), the primary capacitance is independent of load. In contrary, in the parallel compensated primary (PP and PS), the primary capacitance is sensitive to load variation, which means the capacitance needs to be actively adjusted to keep working at optimal efficiency when the load condition changes.

3.1.4 Motivation of using LCL-S compensation network

Based on the discussion before, the secondary compensation network defines how the output behaves, either as a current source or as a voltage source. In the application as APS, a constant output voltage is desired, therefore the series compensation secondary is chosen.

In addition, the work presented in this thesis considers that primary coils are all connected in series, in order to simplify the primary side electronics. The load condition of one secondary will be reflected to the common primary path, which means unstable voltage outputs could be caused by dependency among secondary sides. In order to decouple this dependency, current source behavior is required on

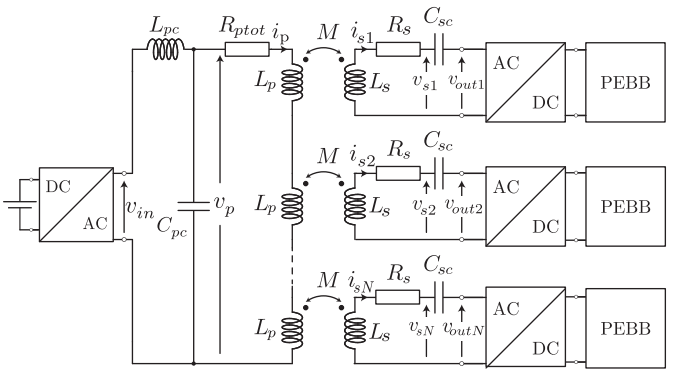

Fig. 3.5 IPT system with LCL-S compensation network (LCL compensation on the primary side and series compensation on the secondary side). The IPT system has series connected primary coils and multiple secondary coils and supplying auxiliary power to PEBBs.

the primary side. However, according to (3.35), in either series or parallel connected compensation network, the input impedance as well as input current depends on the reflected impedance from the secondary side. In contrary, LCL compensation as shown in **Fig. 3.5** behaves as a constant current source and provides benefits for supplying independent secondary [114].

Prior research on LCL has focused on the application with a single primary coil and optimization of compensation components [114]–[116]. However, application of distributed primary coils are not discussed and optimization of operating parameters such as input voltage, switching frequency, converter topology, which can be chosen in a wide range, are ignored. Therefore, a systematic design algorithm and analysis of the LCL-S compensation network for IPT system with multiple primary coils is needed.

3.2 Design of LCL-S Compensation Network

3.2.1 Technical requirements specifications

Components in the coil link including primary and secondary coils, LCL-S compensation network components need to be designed according to application specification. Many modular converter topologies would have several floating PEBBs and require relatively low amount of power to supply to each PEBB, e.g. from 10 W - 150 W for sensors, gate drivers, etc. This is a very broad range of specification, that is hard to address with one unique solution. For those reason, this chapter considers, without loss of generality, 5 stacked cells and 24 Vdc as average output voltage of each receiver. Ranges of variables of interests are summarized in **Tab. 3.4**. Considering using 220 Vac input and a PFC stage to supply DC voltage as input source, 400 V is chosen as input DC voltage before high frequency inverter.

In **Fig. 3.5**, L_p and L_s are primary side and secondary side coil inductance respectively. $R_{ptot} = NR_p$ and $L_{ptot} = NL_p$ are total equivalent winding resistance and total inductance of multiple primary coils in series, respectively. R_s is winding resistance on each receiver coil. L_{pc} and C_{pc} are compensation components on the primary side, and C_{sc} is the compensation capacitor on the receiver side. The

Tab. 3.4 Parameter Specifications

Design parameter	Variable	Range
Output power of each receiver	P (W)	10-150
Operating frequency	f (kHz)	50-500
Total input DC voltage	U_{in-DC} (V)	400
Output DC voltage of each receiver	U_{out-DC} (V)	24 ± 6
Coupling factor	k	0.02-0.25
Amount of primary coils	N	5

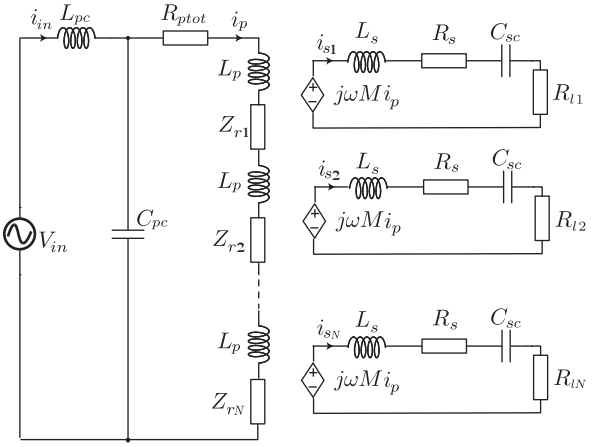

Fig. 3.6 Current controlled voltage source equivalent circuit of IPT system in **Fig. 3.5**.

relations describing the system in **Fig. 3.5** are:

$$\begin{aligned} V_p &= (R_{ptot} + j\omega L_{ptot})I_p - \sum_{i=1}^{N} j\omega M I_{si} \\ V_{si} &= j\omega M I_p - (R_s + j\omega L_s)I_{si} \end{aligned} \tag{3.36}$$

Where, $i \in [1, N]$. System (3.36) can be transferred into an equivalent circuit including current controlled voltage sources, as shown in **Fig. 3.6**. The voltage imposed to the secondary coils side is controlled by the current of primary side. The impedance of the secondary reflected to the primary Z_r is shown in **Tab. 3.1**. If the current going through the series connected primary coils could be kept constant, the different secondary coils will not influence each others' output voltage [117].

3.2.2 Source and load modeling

For a bridge inverter or rectifier with each leg operating at 50% duty cycle and phase shift of 180°, the voltage amplitude of AC voltage at fundamental frequency is

$$\begin{aligned} \hat{U}_{AC} &= \frac{4}{\pi} U_{DC} \quad \text{full bridge converter} \\ \hat{U}_{AC} &= \frac{2}{\pi} U_{DC} \quad \text{half bridge converter} \end{aligned} \tag{3.37}$$

On the secondary coil side, the equivalent AC load R_{load} is used to model the rectifier and the actual DC load. [118].

$$R_{load} = \frac{1}{2}\frac{\hat{U}_{out-AC}^2}{P_{out}} \tag{3.38}$$

Based on the relation between AC and DC voltage, the equivalent AC load is,

$$\begin{aligned} R_{load} &= \frac{8}{\pi^2}\frac{U_{out-DC}^2}{P_{out}} \quad \text{full bridge rectifier} \\ R_{load} &= \frac{2}{\pi^2}\frac{U_{out-DC}^2}{P_{out}} \quad \text{half bridge rectifier} \end{aligned} \tag{3.39}$$

3.2.3 Maximum efficiency

In our application, since the nominal required output power for each secondary side is fixed, the maximum efficiency instead of maximum output power becomes the optimization goal [119].

The efficiency at optimal frequency $\omega_{opt} = \omega_{resA} = \omega_{resP}$ has been calculated in (3.31):

$$\eta_{link} = \frac{k^2 Q_p \alpha}{\left(\alpha + k^2 Q_p + \frac{1}{Q_s}\right)\left(\alpha + \frac{1}{Q_s}\right)} \tag{3.40}$$

Based on the result of (3.40), the optimal load factor is determined by solving $\frac{\partial \eta_{link}}{\partial \alpha} = 0$. For similar and high coil quality factors Q_p and Q_s, the optimal load factor in (3.32) is [102]:

$$\alpha_{opt-\eta} = \frac{\sqrt{1 + k^2 Q_p Q_s}}{Q_s} \approx k \tag{3.41}$$

The maximum link efficiency under optimal frequency $\omega = \frac{1}{\sqrt{L_s C_{sc}}}$ and optimal load factor $\alpha = k$ is:

$$\eta_{link-max} = \frac{k^3 Q_p Q_s^2}{\left(1 + kQ_s + k^2 Q_p Q_s\right)(1 + kQ_s)} \tag{3.42}$$

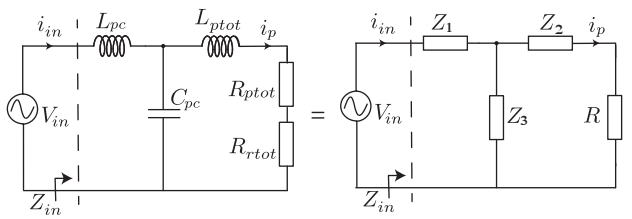

Fig. 3.7 Simplified equivalent circuit of series connected primary coils.

3.2.4 Voltage gain

The output voltage of the coil pair needs to meet the electric specifications. In order to calculate the secondary side output voltage, one needs to know the secondary side input voltage. As shown in **Fig. 3.6**, the secondary side input voltage is $j\omega MI_p$ which depends on the primary side characteristics. The primary side with LCL compensation network is shown in **Fig. 3.7**. With the aforementioned ideally compensated network at secondary coil side, the reflected impedance Z_r becomes purely resistive and total reflected resistance is:

$$R_{rtot} = \sum_{i=1}^{N} \frac{\omega^2 M^2}{R_{li} + R_s} \tag{3.43}$$

As shown in **Fig. 3.7**. The input impedance seen from the source side is:

$$Z_{in} = Z_1 + \frac{Z_3(Z_2 + R)}{Z_3 + (Z_2 + R)} \tag{3.44}$$

where, Z_1, Z_2 and Z_3 are purely inductive: $Z_1 = jX_1 = j\omega L_{pc}$, $Z_2 = jX_2 = j\omega L_{ptot}$, $Z_3 = jX_3 = \frac{1}{j\omega C_{pc}}$ and $R = R_{rtot} + R_{ptot}$.

The current going through the primary coil is calculated with Z_{in}:

$$I_p = \frac{U_{in}}{Z_{in}} \frac{Z_3}{Z_3 + (Z_2 + R)} = \frac{U_{in}}{(R + Z_2)(1 + \frac{Z_1}{Z_3}) + Z_1} \tag{3.45}$$

The primary current going through each primary coil should remain constant, i.e. I_p should be independent of R. Based on (3.45), the relation between Z_1 and Z_3 is determined:

$$Z_3 = -Z_1 \Rightarrow C_{pc} = \frac{1}{\omega^2 L_{pc}} \tag{3.46}$$

The output voltage on i^{th} secondary coil side with the assumption in (3.46) is derived as:

$$V_{out-i} = V_{in} \frac{k\sqrt{L_p L_s}}{L_{pc}} \frac{R_{li}}{R_{li} + R_s} \tag{3.47}$$

One should notice that output voltage is independent of the load condition of other secondary coils. In (3.47), once the input DC voltage is fixed, the primary side AC voltage V_{in} depends on the inverter topology and phase angle. Primary and secondary coils as well as the primary compensation inductor will be designed to achieve desired voltage gain.

3.2.5 Input impedance angle

In the previous discussion, the relation between Z_1 and Z_3 is found to meet the independent secondary outputs requirement. The relation with Z_2 defines the input impedance angle. Based on the relation in (3.46), substituting Z with jX in (3.44), and taking $Z_3 = -Z_1$ into consideration:

$$Z_{in} = \frac{X_1^2 R}{R^2 + (X_1 - X_2)^2} + j\frac{X_1^2(X_1 - X_2)}{R^2 + (X_1 - X_2)^2} \tag{3.48}$$

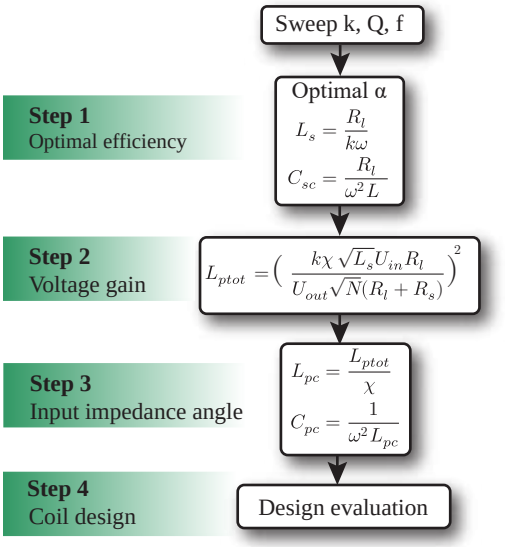

Fig. 3.8 The design flow of LCL-S compensation network.

The input impedance angle is:

$$tan(\theta) = \frac{Im(Z_{in})}{Re(Z_{in})} = \frac{X_1 - X_2}{R} \tag{3.49}$$

Desired input impedance can be achieved by adjusting X_2 and X_1. Defining the ratio of X_1 and X_2 as:

$$\chi = \frac{X_2}{X_1} = \frac{L_{ptot}}{L_{pc}} \tag{3.50}$$

χ determines the input impedance angle. Under this relation, the output voltage is:

$$V_{out} = U_{in} \frac{k\chi\sqrt{L_s}}{\sqrt{NL_{ptot}}} \frac{R_l}{R_l + R_s} \tag{3.51}$$

3.2.6 Design flow

The design flow of compensation network is summarized based on discussion in previous sections and is shown in **Fig. 3.8**. In step 1, based on the principle to achieve optimal load factor α, the secondary resonant components values are determined. In step 2, the primary side total inductance are selected to meet the output voltage requirement. In step 3, primary side compensation components are designed. The primary side compensation inductor and capacitor fully compensate each other achieve constant current through primary coil. The primary compensation inductor is selected to achieve certain input impedance angle.

3.2.7 Influence of the operating parameters on the coil link design

In this section, the analysis is on the component and link efficiency dependence of different operating parameters including coupling factor k, switching frequency f, equivalent coil resistance as well

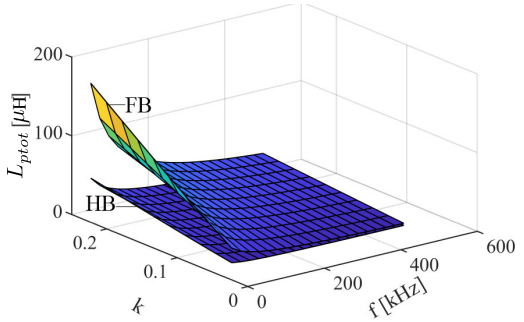

Fig. 3.9 Total coil inductance on the primary side as a function of k, f and inverter topology under ideal compensation.

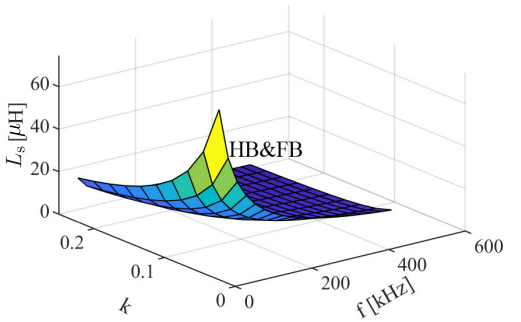

Fig. 3.10 Coil inductance on the secondary side as a function of k, f and inverter topology under ideal compensation.

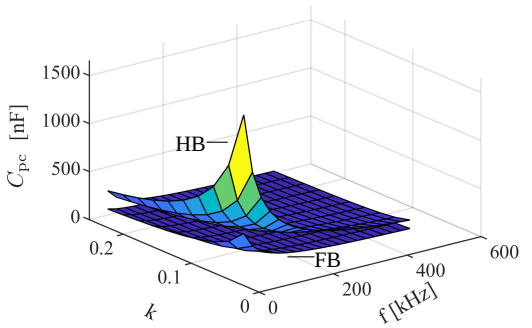

Fig. 3.11 Compensation capacitor on the primary side as a function of k, f and inverter topology under ideal compensation.

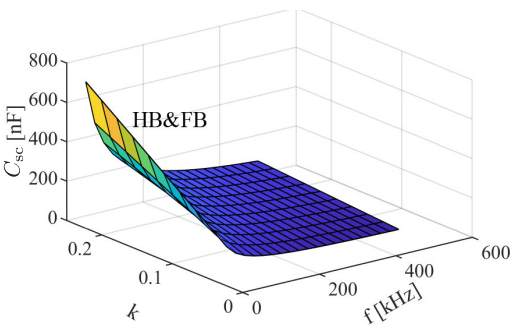

Fig. 3.12 Compensation capacitor on the secondary side as a function of k, f and inverter topology under ideal compensation.

as primary side inverter topology. HB is used as rectifier topology on the secondary side. In the following analysis, semiconductor losses are not considered and winding resistance is assumed as $20\sqrt{L}$ without considering high frequency effects.

According to the design approach presented in previous section, the values of achievable coupling factor k, and selected operating frequency f will influence the ideal components value and the maximum efficiency.

The dependency of various components on inputs are plotted in **Fig. 3.9** - **Fig. 3.12**, considering output power of 100 W at each secondary coil and parameters in **Tab. 3.4**. According to **Fig. 3.8**, the values of coil inductance and compensation components are calculated. Based on (3.33), link efficiency is determined and plotted in **Fig. 3.13**.

As shown in figures from **Fig. 3.9** to **Fig. 3.12**, the coupling factor and frequency will influence the design of both primary and secondary network, and the inverter topology only influence the design of the primary network. Higher frequency f would lead to smaller component values and higher efficiency. Furthermore, it is noteworthy that, with the electric specifications given in this application, smaller difference between primary and secondary coil inductance is achieved with FB inverter.

Furthermore, k, f and U_{in} should be as high as possible to get higher efficiency. In order to achieve certain efficiency, minimum k, f as well as $\frac{U_{in}}{U_{out}}$ can be calculated. As shown in **Fig. 3.14**, each operating

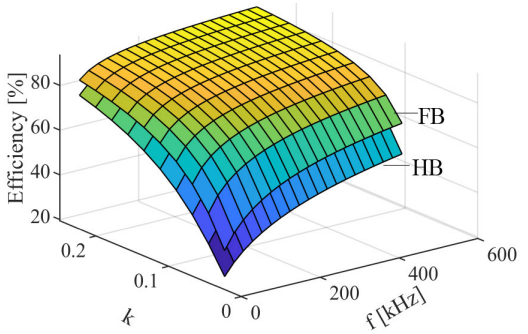

Fig. 3.13 Link efficiency as a function of k, f and inverter topology under ideal compensation.

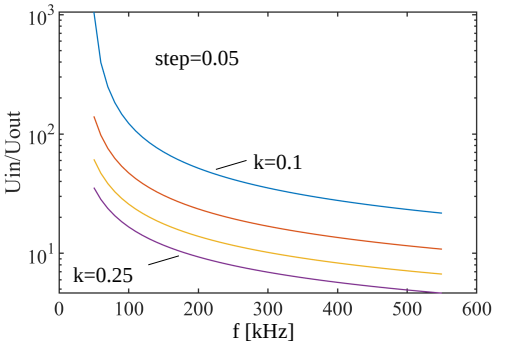

Fig. 3.14 Input output voltage ratio, k and f to achieve 90% efficiency.

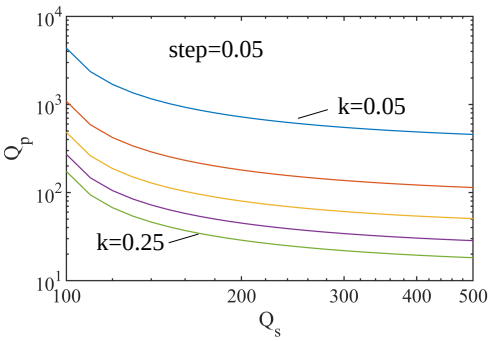

Fig. 3.15 Primary and secondary coil quality factors to achieve 90% efficiency.

point on this plot is identical to 90% link efficiency. In order to attain 90% efficiency, if k is small, higher switching frequency and higher input voltage needs to be implemented.

The link efficiency depends on the primary and secondary coil quality factors and coupling factor. Equivalent coil resistance R_p and R_p influence link efficiency by influencing quality factors. According to the design flow, the total link efficiency is simplified to:

$$\eta_{\alpha=k} = \frac{k^3 Q_p Q_s^2}{\left(1 + kQ_s + k^2 Q_p Q_s\right)(1 + kQ_s)} \tag{3.52}$$

The minimum Q_p and Q_s to achieve 90% efficiency for the optimized compensation network is plotted in **Fig. 3.15**. Minimum Q_p and Q_s could be the guidance in coil design procedure.

3.2.8 Simulation verification

Simulation with PLECS is used to verify the results of the proposed design approach. Network shown in **Fig. 3.16** is simulated. Based on specifications in **Tab. 3.4**, specifying switching frequency as 200 kHz, coupling factor as 0.2, output power of each secondary coil as 100 W and using FB inverter at input stage and HB rectifier at output stage. The primary inductance is calculated to be optimal at 4.61 µH and secondary inductance is 4.64 µH. The compensation capacitors are designed with aforementioned design rules. **Fig. 3.17** shows the voltage and current on primary side under full load condition before and after LCL compensation network.

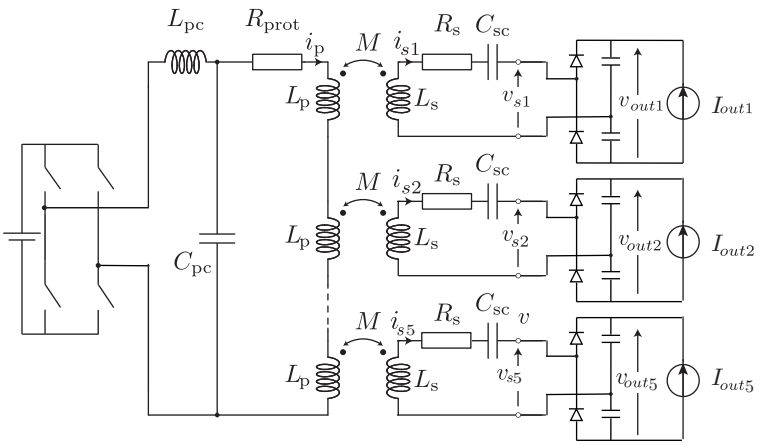

Fig. 3.16 Circuit schematic simulated in PLECS.

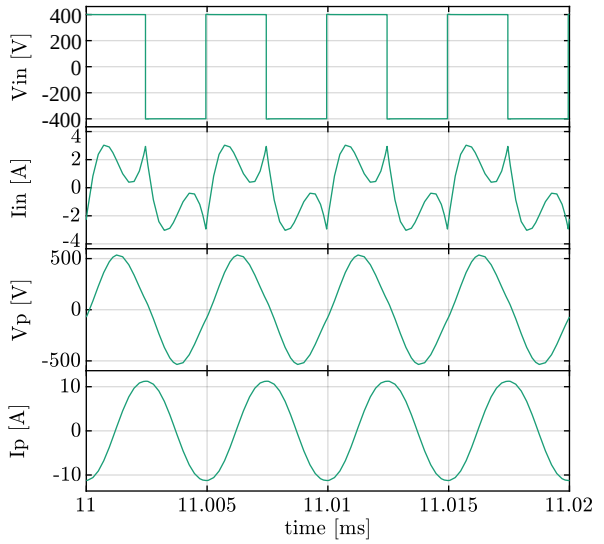

Fig. 3.17 From top to bottom: primary side input voltage before LCL network, current through primary compensated inductor, voltage across all the five primary coils and current through primary coils.

A controlled current source instead of a resistive load is placed at each rectifier output to adjust the load condition. In order to see the influence of load change on secondary and primary side, this current source changes according to the test scenario presented in **Fig. 3.18a**:

- At t_0, all the load currents are set to 0, simulation starts with primary working and all the secondaries are in no-load condition.
- At t_1, all the load currents are set to rated currents.
- At t_2, 5^{th} load current is doubled.
- At t_3, 4^{th} load current is halved.
- At t_4, 3^{rd} and 4^{th} load currents are set to 0.
- At t_5, primary DC link voltage drops to $0.9U_{DC}$.

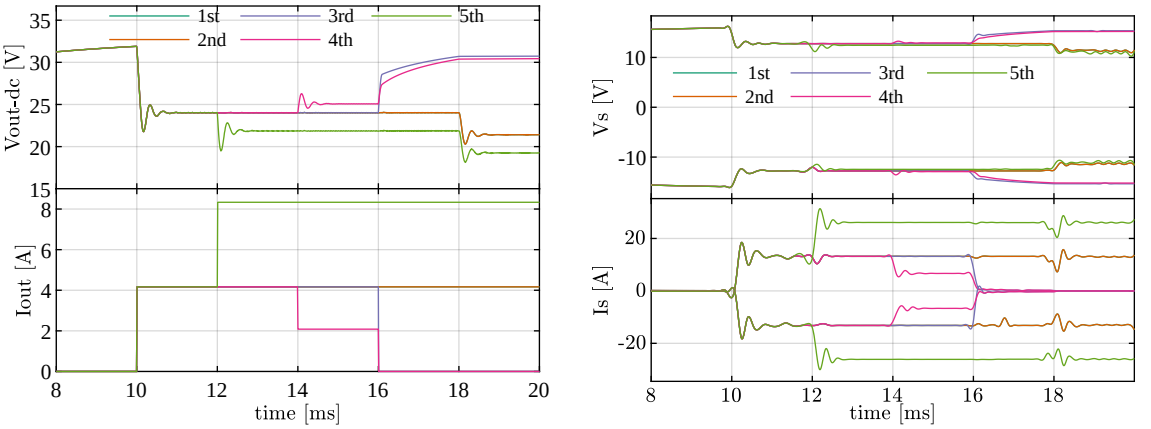

Fig. 3.18 (a) Output DC voltage (image on top) and load current (image on bottom) of each receiver. (b) Envelopes of AC output voltage (image on top) and current (image on bottom) of 5 secondary sides before their rectifier stage.

Fig. 3.18a shows the DC output voltage of 5 secondary coils. Following can be concluded: i) The output of each secondary coil only depends on the load condition on its side and is independent of load conditions of other secondary coils. In the scenario, even though the 3^{rd}-5^{th} loads change, the output voltage of the 1^{st} and 2^{nd} secondary coils remain constant. ii) Load change of one secondary coil leads to a slight increase or decrease in this secondary coil's output voltage. During period t_2-t_5, the voltage of 5^{th} receiver decreases 10% as its load doubles. During period t_3-t_4 , the voltage of 4^{th} receiver increases 8% as its load is halved. iii) The drop of primary input voltage causes same drop on the output voltage. After t_5, the output voltage of each receiver drops 10% as the input voltage drops 10%.

Fig. 3.18b shows the envelope of AC voltage before rectifiers and the envelope of AC currents through secondary side coils. AC voltage and current vary in the same pattern with the DC side voltage and current shown in **Fig. 3.18a**. Therefore similar analysis could be made for **Fig. 3.18b**.

3.3 Summary

In this chapter, four simple compensation networks are analyzed, inspired by which, the LCL-S compensation network is selected to satisfy the design requirements for IPT system with series connected primary coils in application as APS for PEBBs. LCL-S compensation network is designed to have optimal efficiency, pure resistive input impedance to have low reactive power, and to realize the independence among different secondary sides simultaneously.

The design approach considers both optimal compensating components design and operating parameters selection. By following the proposed design approach, each secondary side performs robust output voltage characteristic against the load variation of other secondary coil sides, which is proved by the simulation.

In addition, the parameter sensitivity analysis is performed and shows some inspiration for the coil design in the next chapters. Firstly, the coil design should be designed to achieve high k and Q in

order to achieve high efficiency. Secondly, the results show the higher frequency would lead to high coil link efficiency, however, the analysis so far doesn't take into account that the AC resistance of coil would also increase with higher frequency and it will compensate partially the benefits of operating at high frequency. In the next chapter the AC resistance dependence on frequency is included in the coil design. In the end, when the input voltage of IPT is higher than the output voltage of IPT, the optimal primary coil inductance and secondary coil inductance are closer when using a FB inverter than when using a HB inverter. Closer primary inductance and secondary coil inductance shows potential to have better coupling. Therefore FB inverter is used for further discussion in the next chapters.

4
Modelling and Design of PCB Windings

This chapter presents the modeling of PCB spiral windings, design optimization and analysis considering winding geometry and operating frequency. The coil pair discussed in this chapter has no magnetic or metal shielding. Analytic model considering the geometric distribution of the magnetic field is proposed to calculate with high accuracy equivalent electrical parameters of coils. For a defined design space and constraints, a large number of coils are designed in order to determine the coil link performances and select optimal winding geometries. Selected winding designs are prototyped and experimentally verified under different load conditions.

4.1 Circular Spiral Winding on PCB

Coil design and operating frequency are key factors impacting the efficiency of the inductive power transfer system. The geometry of the planar coil could be rectangular, double-D (DD), or circular. The DD shape is widely used in EV charging applications[120] because it has better performance against lateral displacement but shows higher power loss than single loop coils [121]. For applications where coils are installed in a fixed position, lateral misalignment is not a severe problem. Therefore, the DD coil is not the optimal choice. Comparing circular spiral coils with polygonal spiral coils, the former provides better coupling within the same surface area [80] and a higher optimal quality factor [122].

The circular spiral coil could be realized with litz wire [21] or copper trace on PCB. PCB tracks have much sharper edges and could challenge the dielectric design. However, PCB based IPT as shown in **Fig. 4.1** prevails in the consistency of parameters during manufacturing and easy installation. Even though there is plenty of analysis on PCB coil performance, PCB coil's potential in transferring low amounts of power (around a hundred watt) over the large gap using small size coils in MV applications is not fully explored. There are already preliminary works on PCB coil designs, including inductance, resistance and insulation coordination. For example, self inductance is modeled with current sheet method in [123] which has large error when space between traces is much larger than trace width. AC resistance model is given in [124] which needs FEM simulation to obtain magnetic field. In [125] authors have studied the insulation with air while in [126] insulation has been analyzed with solid dielectric materials including FR4, Polyesterimide and Teflon. However, no systematic design approach for PCB coils could be identified.

This chapter considers the coil composed of only PCB windings and without magnetic or metal shielding around the system. The main purpose is to present a systematic and generalized model-based design approach that outputs a database and from which users could design coil windings based on their own needs and specifications. The optimization approach offers several insights in designing IPT coils and considering air as the only dielectric material between primary and secondary. Firstly, the optimization approach explores the coil link performance in a wide range of coil geometries and

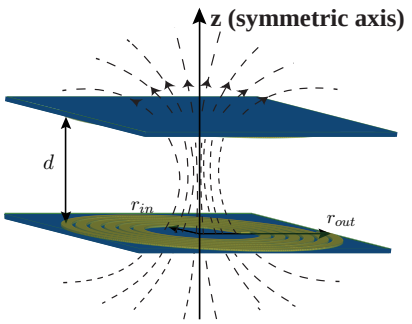

Fig. 4.1 An example of using PCB spiral windings to realize inductive power transfer through air. d is the air gap between the primary coil and secondary coil. r_{in} and r_{out} are the inner and outer radius of primary coil. The secondary coil could have a different geometry from the primary coil.

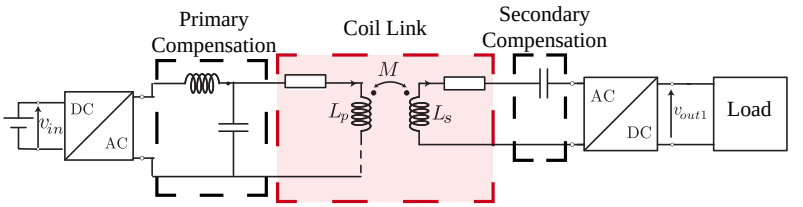

Fig. 4.2 Structure of auxiliary power supply for medium voltage converters. Multiple series connected coils are usually used but only one pair of coil is shown for the illustration.

the trade-off between the power density and efficiency is clearly demonstrated. Secondly, the influence of operating frequency on the performance of the coil pairs is shown, which permits selecting an optimal frequency, for the further system design. Finally, for the selected and prototyped coils, the limits of coil geometry to transfer a certain amount of power are determined through experimental characterization considering variation of distance between the coils as well as minor misalignment that would occur in practice.

4.2 Optimization Domain

The LCL-S compensation network as shown in **Fig. 4.2** is discussed in **Chap. 3**. It has to be noted that the optimization approach proposed in this chapter is generalized and the workflow is also valid for different compensation strategies. The different topologies and electric specifications influence only the filtering criteria. Therefore, the optimization result would differ with different compensation networks [112].

While the general medium voltage range up to 36 kV is considered as relevant, 6 kV system working voltage is taken as the case to illustrate the optimization approach. The insulation distance is defined based on this voltage from the standard IEC 61800-5-1 [127]. Other electric specifications used for the application considered in this chapter are listed respectively in **Tab. 7.1**. Output DC voltage of 36 ± 2 V is defined as reference which could be further regulated with additional DC-DC converters for supplying various loads inside the PEBBs. Similarly, 130 W output is considered as reasonable nominal power level demand for one power electronics building block in MV converters, including gate drivers, controllers, cooling fan etc.

Considering the trade off between the low switching loss on power electronics switches and high

Tab. 4.1 Design specifications

V_{in}	V_{out}	$U_{ins-rms}$	P_{out}	*thickness*
80 V	$36 \pm 2V$	6 kV	130 W	70 µm

Tab. 4.2 Design space of PCB coil geometries and operating frequency

Sweeping inputs	Characteristics	Value/Range	Units
Outer radius	r_{outp}, r_{outs}	10-75	mm
Copper trace width	w_p, w_s	1-20	mm
Space between adjacent copper turns	s_p, s_s	1-20	mm
Number of turns of one coil	n_p, n_s	$max = \frac{Rout}{w+s}$	-
Operating frequency	f	50-1000	kHz

efficiency on coil links, operating range is taken from 50 kHz to 1 MHz. Considering the mechanical constraints in typical MV converter assembly, maximum coil diameter is restricted to 150 mm. The geometries ranges studied in this chapter are shown in **Tab. 4.2**.

It should be noted that both the electric specifications and coil geometries restriction should be changed according to application requirements. Nevertheless, the proposed analytic model and optimization approach is generalized and can be adapted in other application scenarios.

4.3 PCB Spiral Coil Modeling

An accurate mathematical model of inductance and resistance is the basis for designing coils. In this section, the magnetic field is first mathematically modeled, followed by the modeling of self-inductance, AC resistance, and mutual inductance.

4.3.1 Modeling of external magnetic field

One of the common methods used in solving magnetic fields is to solve Maxwell's equations for rectangular cross sections by dealing with numerical integration [128]. Despite being slow and complicated, this method gives precise results. Another popular approach is the filament method, which considers coil as a dimensionless filament of negligible cross-section [129]. It gives a closed-form equation but has larger errors when the cross-sectional dimension is large. Here, a modified filament method is proposed, using two current loops on conductor edges to represent the current in one turn circular conductor. The proposed method intends to have smaller errors while keeping the calculation's simplicity.

The cross section of PCB based spiral coil is illustrated in **Fig. 4.3**. For simplicity, coaxial circles are typically used instead of spiral structure [126][102]. The external magnetic field H_{ex} in the i^{th} turn defined as $H_{ex,i,tot}$ refers to the magnetic field caused by current in other turns excluding the magnetic

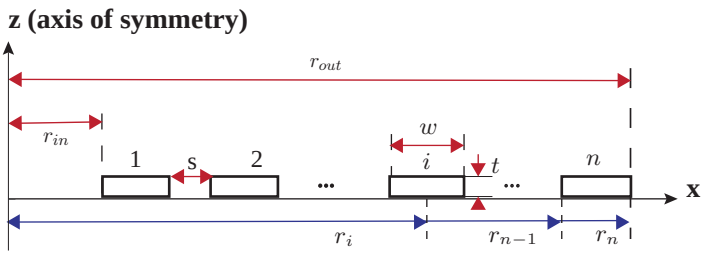

Fig. 4.3 The illustration of a coil winding geometry in a half symmetric plane. This coil has n turns, w as width of each turn and s as the gap between adjacent turns. r_{in} and r_{out} are the inner and outer radius of primary coil. The secondary coil could have a different geometry from the primary coil.

field caused by its own current [130].

$$H_{ex,i,tot} = \sum_{k=1}^{N} H_{i,k},\ k \neq i \tag{4.1}$$

Three simplifications are made in obtaining an analytic model. Firstly, since the thickness of the coil t is rather small (commonly used PCB thickness is 35 µm or 70 µm), as shown in **Fig. 4.3**, the external H field parallel along the e_x axis is ignored, and only the magnetic field in e_z direction is considered. Secondly, since in the defined frequency range (50 kHz-1 MHz), the skin depth is at least three times smaller than trace width in the design space ($\geq$ 1 mm), current in one trace is simplified to two dimensionless current loops at left and right edges. Thirdly, the nonuniform distribution of magnetic field inside the track is simplified to be constant and is represented by the magnetic field at the center point of the track. Taking n^{th} turn as an example, the average magnetic field in i^{th} turn caused by n^{th} turn, as shown in **Fig. 4.4** is [130]:

$$H_{ex,i,n} = \frac{1}{\mu_0}\frac{\mu I_l}{4\pi}\frac{1}{r_{n-l}+r_i}\left[K(k_l) + \frac{r_{n-l}^2 - r_i^2}{(r_{n-l}-r_i)^2}E(k_l)\right] + \frac{1}{\mu_0}\frac{\mu I_r}{4\pi}\frac{1}{r_{n-r}+r_i}\left[K(k_r) + \frac{r_{n-r}^2 - r_i^2}{(r_{n-r}-r_i)^2}E(k_r)\right] \tag{4.2}$$

In the equation above, I_l and I_r are the current on the left and the right edge, respectively. $K(k)$ and $E(k)$ are complete elliptical integrals of first and second kind to modulus k.

$${k_{l/r}}^2 = \frac{4r_{n-l/r}r - i}{(R+p)^2} \tag{4.3}$$

and,

$$\begin{aligned} K(k) &= \int_0^{\frac{\pi}{2}} \frac{d\theta}{\sqrt{1-k^2 sin^2\theta}} \\ E(k) &= \int_0^{\frac{\pi}{2}} \sqrt{1-k^2 sin^2\theta}\, d\theta \end{aligned} \tag{4.4}$$

In order to get I_l and I_r, two steps are followed. Firstly, currents are supposed to be equally concentrated on the left and the right edge $I_l = I_r = \frac{I}{2}$, where I is the total current inside the conductor. Initial magnetic field is obtained with (4.2). The electric field distribution along x axis is

$$\frac{\partial E_y}{\partial x} = -j\omega\mu H \tag{4.5}$$

Further, $J_{prox-edge}$, the current density at both edges under the external magnetic field is obtained

$$|J_{prox-edge}| = -j\omega\mu\frac{w}{2}\sigma H \tag{4.6}$$

In this equation, ω is the angular frequency of current excitation, $\mu = 4\pi\, e^{-7}$ is the magnetic permeability of copper, w is the width of copper trace, σ is the conductivity of copper and H is the external magnetic field.

The current density at both edges under skin effect is approximated as

$$J_{skin-edge} = \frac{I}{2t\delta} \tag{4.7}$$

where t is the thickness of copper trace and δ is the skin depth. Finally the current density on both edges is the result of two effects

$$\begin{aligned} J_{edge-left} &= J_{skin-edge} + J_{prox-edge} \\ J_{edge-right} &= J_{skin-edge} - J_{prox-edge} \end{aligned} \tag{4.8}$$

Under the filament approximation, the summation of the left edge current I_l and right edge current I_r is the entire current I. Current distribution is

$$\begin{aligned} I_l &= I\frac{J_{edge-left}}{J_{edge-left} + J_{edge-right}} \\ I_r &= I\frac{J_{edge-right}}{J_{edge-left} + J_{edge-right}} \end{aligned} \tag{4.9}$$

Finally, the magnetic field is solved with (4.2) and (4.9).

Comparing to the original filament method where the winding turns are represented by one current loop in middle of the conductor trace, the proposed method considers two current loops at edges of the each turn. Besides, the proposed method considers the redistribution of magnetic field with the knowledge of current density distribution. The accuracy of the proposed approach is validated with randomly selected coil geometry against FEM simulations. In **Fig. 4.4**, the result of a spiral coil of 6 turns with $w = 5\,\text{mm}, t = 0.07\,\text{mm}, R_{out} = 70\,\text{mm}$ is shown. The real magnetic field distribution is not linear. Comparing to the result with the filament method from [129], the result of proposed method better presents the mean value of the real distribution.

4.3.2 Modeling of self inductance

The current sheet method is commonly used for modeling the inductance, which considers multiple spiral turns as one single current sheet [123]. However, the error increases when the ratio between s and w is bigger than 3. The data-fitting technique for a predefined monomial model is also an option [123], but the existing model is only for polygonal spiral coils, not for circular coils.

In the following discussion, the spiral coil is modeled as coaxial circular conductors. The inductance of the circular spiral coil can be expressed as the sum of self inductance of each circular sheet and mutual inductance between each pair of sheets. This method intends to avoid error caused by large space between turns.

$$L_{spiral} = \sum_i L_i + \sum_{i,j} M_{i,j}, \forall i, j \in n \tag{4.10}$$

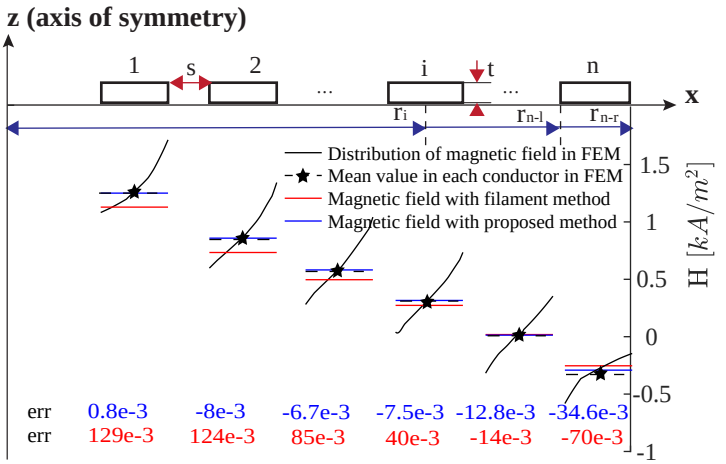

Fig. 4.4 Concentric circular conductors with rectangular cross sections and magnetic filed distribution with a current excitation of 1 A at 500 kHz for a 6-turn coil with $w = 5$ mm, $t = 0.07$ mm, $R_{out} = 70$ mm. The errors are absolute errors: err = modeling result - mean value of simulation result.

This summation method works for all the s and w ranges. The self inductance and mutual inductance in (4.10) are [122][131]:

$$L_i = \mu r_i \left[ln(\frac{2r_i}{w}) + 0.9 + 0.05\frac{w^2}{r_i^2} \right] \tag{4.11}$$

$$M_{i,j} = \frac{\mu(r_i + r_j)}{2} \left[ln(\frac{r_i + r_j}{w + s}) - 0.6 + 0.7(\frac{w + s}{r_i + r_j})^2 \right] + \left[0.2 + \frac{(r_i + r_j)^2}{12(w + s)^2} \right] \frac{\mu\omega^2}{2(r_i + r_j)} \tag{4.12}$$

Again, the analytic model of PCB coil inductance are checked against the FEM simulations for randomly selected coil geometries. **Fig. 4.5** shows the inductances extracted from ANSYS Maxwell 3D and analytic modeling for the coils with 6 turns and outer radius $R_{out} = 75$ mm. With the constraints of outer radius and number of turns, the maximum trace width is 9 mm. Trace width and space between turns are swept to generate more designs. According to **Fig. 4.5**, the analytic result correlates well with FEM result for all considered coil geometries.

4.3.3 Modeling of AC resistance

Unlike traditional inductor design, there is no empirical model calculating resistance of PCB spiral coils. Besides, unlike circular cross-section conductor [132], there is no closed-form analytic expression to calculate the resistance of a rectangular cross-section coil. Therefore, a hybrid FEM database and magnetic field calculation method is proposed in order to increase the accuracy in resistance calculation.

4.3.3.1 Orthogonality of conduction and proximity losses

In the rectangular cross-sectional conductors, the independence of conduction and proximity losses remains as in the round wires. The superposition of current densities due to skin effect and proximity

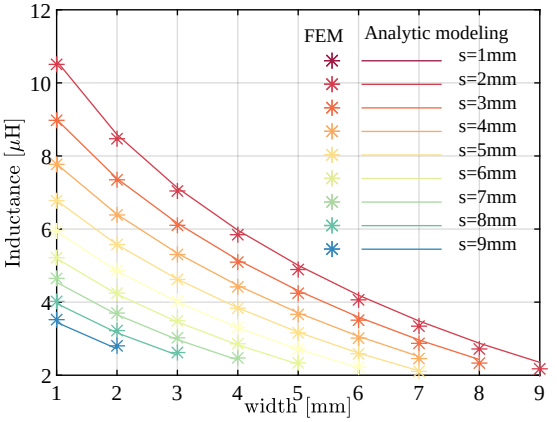

Fig. 4.5 Inductance extracted from FEM simulation and from analytic modeling. The studied coil has 6 turns and outer radius of 75 mm. The trace width and space between turns vary with a step of 1 mm.

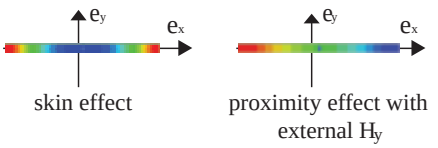

Fig. 4.6 Current density distribution caused by skin effect, proximity effect in a conductor track with rectangular cross section and infinite length in e_z direction.

effect is involved. In addition, considering that the PCB traces are thin, only the magnetic field in e_y direction is considered as shown in **Fig. 4.6** and the total loss P_{ac} for unit length can be calculated as

$$P_{ac} = \frac{1}{2\sigma}\int_S (J_{cond} + J_{prox,y}) \times (J_{cond} + J_{prox,y})^* dS. \tag{4.13}$$

where, J_{cond} is the current density induced by skin effect and distributed symmetrically with respect to both axes, as shown in **Fig. 4.6**. $J_{cond}(x, y) = J_{cond}(x, -y) = J_{cond}(-x, y)$. $J_{prox,y}$ is the current density induced by external magnetic field in e_y direction H_y. $J_{prox,y}$ is anti-symmetrical with respect to e_x, $J_{prox,y}(x, y) = -J_{prox,y}(-x, y)$. These properties imply that all the cross-term products in (4.13) is zero. Therefore (4.13) can be simplified as the superposition of conduction losses (caused by the influence inside the conductor including skin effect loss under high frequency excitation) and proximity loss (caused by the influence of other conductors).

$$P_{ac} = \frac{1}{2\sigma}\int_S \left(J_{cond}J_{cond}^* + J_{prox,y}J_{prox,y}^*\right) dS \tag{4.14}$$

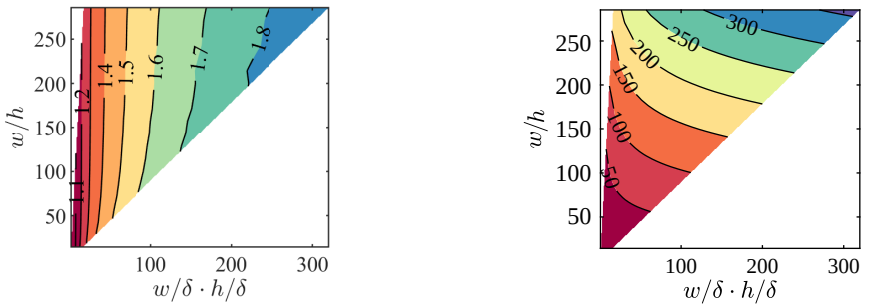

(a) (b)

Fig. 4.7 Dimensionless functions extracted from FEM simulation (a) Φ_{cond} (b) Φ_{prox}. Φ_{cond} is obtained by setting a current excitation through a straight conductor. Balloon boundary is set at the region edges. Φ_{prox} is obtained by setting a constant magnetic field in e_y direction. Variant magnetic vector potential is set at the simulation region edges.

4.3.3.2 FEM database to evaluate resistance

In rectangular cross-sectional conductors, expressions to evaluate both types of losses are given in [124]:

$$\begin{aligned} R_{condu.l.} &= \frac{1}{whs}\Phi_{condrec}(w/\delta, h/\delta) \\ R_{proxu.l.y} &= \frac{4\pi}{\sigma}\Phi_{proxrec}(w/\delta, h/\delta)\hat{H}_y^2 \end{aligned} \tag{4.15}$$

where H_y is the external magnetic field and are calculated with magnetic field model in **Sec. 4.3.1**. Φ are dimensionless functions which describe frequency and geometry dependency of resistance, which can be obtained by FEM simulation. With current I through the spiral coil, the power loss is:

$$P_{ac,u.l.} = \frac{1}{2}(R_{condu.l.} + R_{proxu.l.y})I^2 \tag{4.16}$$

Since Φ_{cond} and Φ_{prox} in (4.15) don't have closed-form analytic expressions, FEM is used to calculate the value of these functions. In ANSYS Maxwell 2D, the conductor is modeled as a straight conductor with infinite length. The geometry and frequency are swept according to **Tab. 4.2**. In addition, copper thickness t is swept from 0.035 mm to 0.21 mm.

It has to be noted that FEM is only used to generate database for Φ in (4.15) rather than directly for AC resistance because Φ has fewer free dimensions and requires a much smaller database.

In **Fig. 4.7a** and **Fig. 4.7b**, the x-axis $w/\delta \cdot h/\delta$ is the cross-section area of the conductor scaled by skin depth, which reflects the influence of high frequency. The value smaller than 1 means the frequency effect can be ignored. The bigger value means the stronger influence of the high frequency on the effective conducting area. The y-axis w/h represents the form factor of the cross-section, with the value close to 1, the cross-section is close to a square area. The function model can be obtained by importing these data into Matlab and using the curve fitting tool. The output of the curve fitting tool is dimensionless function Φ. In this thesis, our function is obtained with the Biharmonic interpolation method.

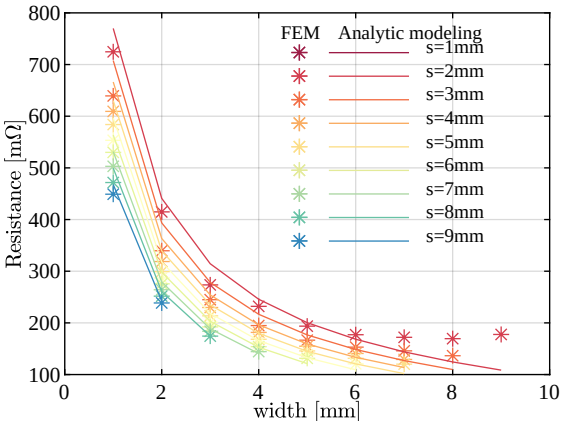

Fig. 4.8 Resistance at 500 kHz extracted directly from FEM simulation and from analytic calculation in (4.15). The studied coil has 6 turns and outer radius of 75 mm. The trace width and space between turns vary with a step of 1 mm.

4.3.3.3 FEM Verification

The modeling of resistance of spiral coil is verified with the same case for self inductance verification. As shown in **Fig. 4.8**, the modeling matches well with the FEM results in most cases. With the increase of the trace width ($w > 8mm$), the error becomes larger, which results from the simplification while modeling the magnetic field as well as the simplification by using concentric circles instead of spiral coils. However, considering that in reality, very wide PCB traces are rarely used in spiral coils, the proposed fast modeling of resistances is still applicable in most cases.

4.3.4 Modeling of mutual inductance

Power transfer requires at least two coils. As shown in **Fig. 4.9**, in this chapter, two coils are placed face to face on primary side and secondary side respectively with air between them. In MV application, the smallest distance d between them is determined by the insulation voltage taking into account type of insulation, overvoltage category and pollution degree. Mutual inductance is calculated based on method in [133], where the planar spiral coils are simplified to co-central loops and mutual inductance M is calculated as the summation of mutual inductance between each circular loops.

$$M = \sum_{i=1}^{M} \sum_{j=1}^{N} M_{i,j}(r_i, r_j, d) \tag{4.17}$$

As shown in **Fig. 4.9**, i and j are the respectively i^{th} and j^{th} turn in primary and secondary coils.

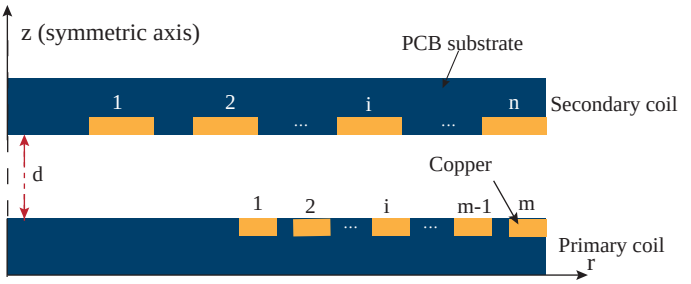

Fig. 4.9 A set of IPT PCB coils in z plane. Copper trace on the outer layer of PCB is the focus of this chapter and PCB substrate design is not discussed here. The air gap between primary coil and secondary coil is *d*. For illustration purpose, primary coil has *m* turns and secondary coil has *n* turns.

4.4 Design Process

In this section, the performance of various coil geometries within the design space in **Tab. 4.2** are evaluated based on the aforementioned mathematical model. The design procedure shown in **Fig. 4.10** is based on brute-force search in the entire design space. Before the start of design approach, the distance between primary and secondary coils in IPT system should be defined and this is addressed in detail thereafter in **Sec. 4.4.1**. In the design procedure, firstly, individual coils are characterized with the inductance model and resistance model proposed in **Sec. 4.3**. Secondly, coils are grouped into pairs, considering all the combinations. Mutual inductance of each pair is calculated with the analytic model in **Sec. 4.3** and based on the coil distance. Thirdly, the power transfer capability of each coil pair is evaluated as illustrated thereafter in **Sec. 4.4.2**. Finally, designs are filtered by the constraints illustrated in **Sec. 4.4.3**. Various coils within the design space in **Tab. 4.2** are evaluated based on the analytic modeling. Width of copper trace is swept from 1 mm to 20 mm, the space between spiral turns is swept from 1 mm to 20 mm and the outer radius of circular coil is swept from 10 mm to 75 mm. The minimum space of 1 mm is taken to avoid electric breakdown between coil turns [134]. For these ranges, 10 equal steps are used in between. The number of turns is from 1 to the maximum allowable turns with defined w, r_{out}, s. Each set of these variables characterize uniquely each single coil. In one coil pair, the primary and secondary don't need to be identical. In total, 1426 single coils with different geometries are designed and 1426^2 combination of coil pairs are explored considering 11 different operating frequencies. With 4 Intel i7 cores, 16GB RAM, it took 24 hours to finish the calculation of all the coils. The inductance and resistance of coils are obtained by modeling, namely, L_p, L_s, R_p, R_s, M. The figure of merits coupling factor and quality factor are defined as $k = \frac{M}{\sqrt{(L_p L_s)}}$, $Q_p = \frac{\omega L_p}{R_p}$, $Q_s = \frac{\omega L_s}{R_s}$. Furthermore, the current through coils, output voltage over the secondary coil, and coil link efficiency are calculated.

4.4.1 Insulation distance

Insulation distance is determined by interpolation from Table 8 and Table 9 in standard IEC 61800-5-1 [127]. The clearance distance for basic insulation between two coils is defined according to the working voltage, the impulse voltage, the temporary overvoltage and the recurring peak value of working voltage. As shown in **Tab. 4.3**, the r.m.s. value of working voltage is 6 kV. The impulse voltage and temporary overvoltage are determined by this working voltage. The impulse voltage also depends on the overvoltage category. With the overvoltage category II, the impulse voltage is 24.8 kV,

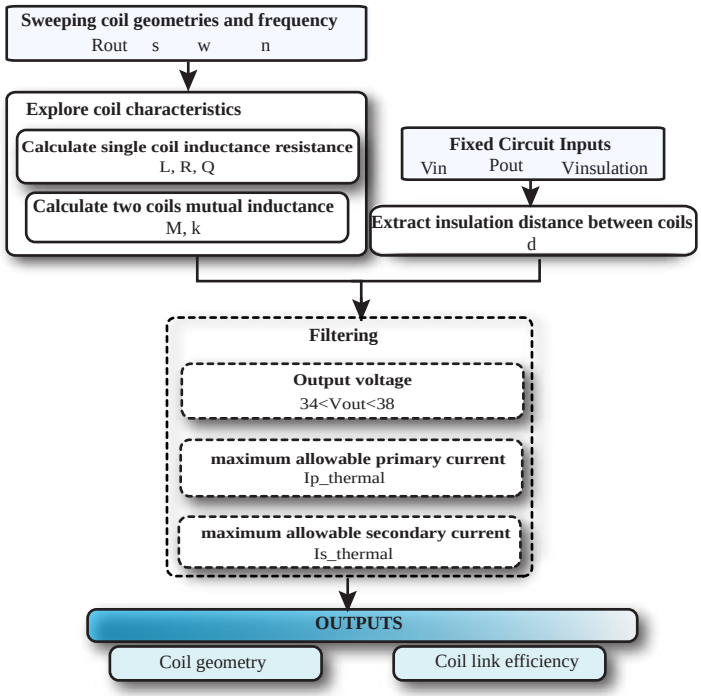

Fig. 4.10 Design procedure to optimize coil pairs in IPT system. The output of this procedure is all the possible primary and secondary coil geometries which meet application requirements. The variable notations in this flow chart correspond to those in **Sec. 4.2**.

and temporary overvoltage is 24 kV. The final clearance distance takes the maximum value among the three distances. However, in practical design considering the complex environment, an extra safety margin is always recommended. Finally, 60 mm is taken as the distance between two coils to realize basic insulation for the 6 kV system. It should be noted that the standard used to define insulation distance should be selected based on different applications.

4.4.2 Power transfer characteristics of coil links

In the following discussion, AC voltages and currents are all in r.m.s values, and the subscript p refers to primary side, while s indicates secondary side. Equivalent model of coil link is shown in **Fig. 4.11**. The coil link efficiency is the product of the efficiency of primary side and secondary side. Provided ideal compensation

$$\eta_{coillink} = \eta_p \eta_s = \frac{R_r}{R_r + R_p} \frac{R_l}{R_l + R_s} \tag{4.18}$$

Tab. 4.3 Minimum clearance distance required to provide basic insulation

System working voltage	6 kV	Minimum clearance distance	28.4 mm
Impulse voltage of overvoltage category II	24.8 kV	Minimum clearance distance	32.8 mm
Temporary overvoltage	24 kV	Minimum clearance distance	54.84 mm

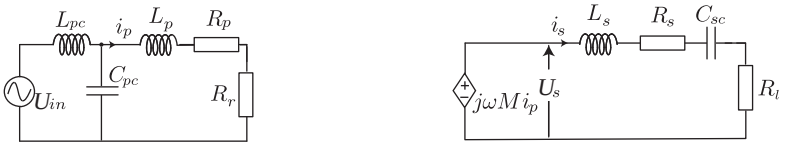

(a) (b)

Fig. 4.11 Equivalent model of IPT system with LCL-S compensation network (a) primary side equivalent model (b) secondary side equivalent model.

Tab. 4.4 Thermal resistance of PCB coil

Name	Value	Description
θ_{Cu}	$0.25\frac{^\circ Ccm^2}{W}$	Thermal resistance of $1cm^2$ copper
θ_{FR4}	$67.43\frac{^\circ Ccm^2}{W}$	Thermal resistance of FR4 substrate in $1cm^2$ and thickness of $0.155cm$
θ_{SA}	$1000\frac{^\circ Ccm^2}{W}$	Thermal resistance from $1cm^2$ PCB surface to air

where, $R_r = \frac{\omega^2 M^2}{R_l + R_s}$ is the reflected resistance of secondary on the primary side. R_l is the equivalent AC load and R_s is the resistance of secondary coil .

The voltage across the secondary coil is:

$$U_s = j\omega M I_p \tag{4.19}$$

After a half bridge rectifier on the secondary side, the DC output voltage is obtained

$$U_{dc} = \frac{\pi}{\sqrt{2}} \frac{U_s R_l}{R_l + R_s} \tag{4.20}$$

4.4.3 Design constraints

By pairing all possible coil pairs, different relations are generated between input and output voltage. The output voltage for each coil pair is shown in **Fig. 4.12**, with many combinations producing output voltage outside the desired range. Useful coil pairs need to be extracted for the analysis. With the current and voltage outputs obtained in the previous section, the coil designs are filtered by two criteria, namely the output voltage range and heat dissipation limit.

The output voltage at the rated power is limited in the range 34 V - 38 V. The coil pairs that violate this voltage range are filtered out and not will not be analyzed further.

Regarding heat dissipation, natural convection is considered so far. With natural cooling, thermal resistances are shown in **Tab. 4.4**. Since $\theta_{Cu} \ll \theta_{SA}$, the thermal resistance of primary and secondary coil are dominated by the copper coverage surface $\pi(R_{out}^2 - R_{in}^2)$ and copper thermal resistance θ_{SA}. Since the thickness of FR4 is minimal ($\approx 1.55mm$), the heat is approximately dissipated equally through

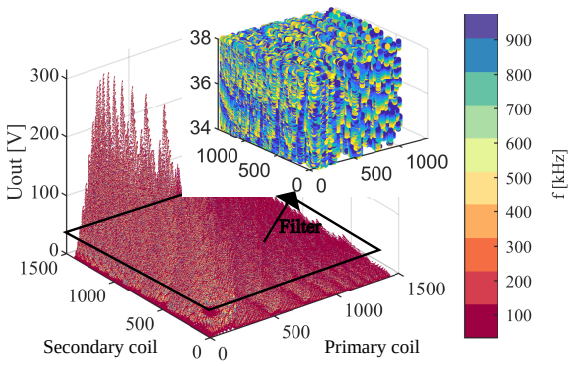

Fig. 4.12 Output voltages of all the coils under operating frequency range from 50 kHz to 1 MHz are shown. After filtering by design constraints, 18868 designs are left and are shown in the zoom-in view.

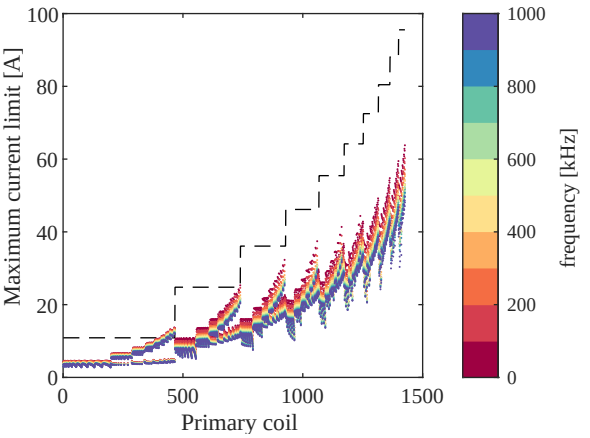

Fig. 4.13 Two different current limitations: black dashed represent the current limitation extracted from standard IPC-2221 [135]; colorful dots represent current limit calculated by conductor loss. Four parameters are swept from inner loop to outer loop following the order: n, r_{out}, s, w. Four parameters increase as the coil numbering rises.

both sides of the PCB board, thus

$$R_{th} = R_{th-uppersurface} + R_{th-lowersurface} = \frac{\theta_{SA}}{\pi(R_{out}^2 - R_{in}^2)} \frac{1}{1 + \frac{1000}{1067}} \frac{w}{w+s} \tag{4.21}$$

The current limited by the heat dissipation capability is

$$I_{cal} = \sqrt{\frac{T}{R_{th} R_{coil}}} \tag{4.22}$$

where R_{coil} is the resistance of coil obtained from analytic modeling; $\triangle T$ is the allowed temperature rise.

Another current restriction comes from standard IPC-2221 [135], where the same current limit are used under variant current excitation frequency. By curve fitting, the maximum current in the external copper layer is:

$$I_{std} = (width \cdot thickness)^{0.725} 0.048 \;\; T^{0.44} \tag{4.23}$$

The current limited by thermal dissipation capability takes the minimum value between the I_{std} and I_{cal}. The comparison of I_{std} and I_{cal} is shown in **Fig. 4.13**. I_{std} extracted from the standard is usually higher than the calculated value I_{cal}.

4.5 Design Results

In the entire design space in **Tab. 4.2**, $1426^2 \times 11$ coil pair designs were explored. Taking k and Q as the evaluation criteria, the influence of variation in coil geometries and frequencies are illustrated.

4.5.1 Influence of Coil geometry

High coupling factor k and high quality factor Q_p, Q_s are the figure of merits to achieve high coil link efficiency. Therefore, they are considered as main performance indicators for coils. Several important coil geometry properties are explored. Their influence on k, Q and coil link efficiency are analyzed. The results shown here are all at an operating frequency of 500 kHz.

- Surface area of coil

  The surface area here is defined as $\pi\, r_{out}^2$. The surface area influences significantly the coupling factors between two coils and the quality factor of each coil. As shown in **Fig. 4.14**, when the surface area increases, the maximum reachable k and Q also increase. A large outer radius also brings high achievable efficiency.

- Inner radius of winding

  To minimize eddy current effects and get higher coupling, majority of previous studies recommend to eliminate the most inner turns by leaving a hole in the middle of the spiral coil [136], [137]. The relation between the coil inner radius and k, Q is presented in **Fig. 4.15**. The 3D plot includes the consideration of combinations of different primary and secondary coils. On the other hand, the 2D plot considers only the combination of identical primary and secondary coils. From the 2D plots, it is apparent that Q is expected to drop sharply after the peak. With the decrease in different outer radius, the optimal inner radius for peak Q is decreasing. For the ten outer radius [10, 17.2, 24.4, 31.7, 38.9, 46.1, 53.3, 60.6, 67.8 75] mm, the corresponding inner radius to achieve highest Q are [5, 8.2, 11.4, 14.6, 17.9, 21.1, 24.3, 27.6, 30.8, 36] mm.

- Space-width ratio

  The space between each turn affects Q. A narrow space brings higher inductance, but it also means a stronger proximity effect leading to higher coil resistance. Therefore an optimal range exists to achieve a maximum Q. Based on our database, $\frac{s}{w} \leq 1.5$ is a reasonable optimal range.

- Number of turns and trace width of winding

  Based on our data set, the optimal w to achieve Q and k are scattered over the entire design

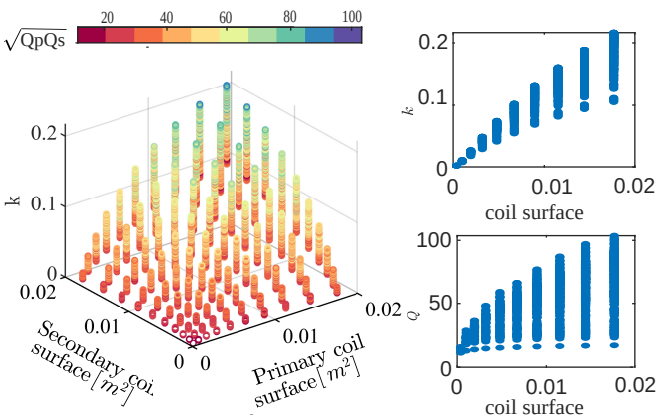

Fig. 4.14 The relation between the coil surface area, coupling factor and quality factor. The 3D view is on left. On the right, 2D plots are shown with identical primary and secondary coils.

space. For the turns number n, there is no general optimal range to achieve maximum k.

In order to see the optimal design range of each geometry parameter, a radar plot is shown in **Fig. 4.16**, where each leg of the radar plot is a different design parameter. The design points on each leg define the optimal range for this parameter. For example, the outer radius are all at 75 mm, the $\frac{s}{w}$ ratio is less than 2, inner radius and turns number are scattered in a larger range in the design space and no optimal design range is observed. This shows that the larger outer radius, the higher performance. And $\frac{s}{w}$ is a delicate parameter which has a upper limit of optimal design range.

4.5.2 Influence of operating frequency

The results discussed in this section consider only the filtered designs. In **Fig. 4.17**, there is a clear trend that in the defined frequency range, quality factor increases as frequency increases, which is explained as the increase of coil resistance caused by high frequency is not comparable to the increase of inductive reactance.

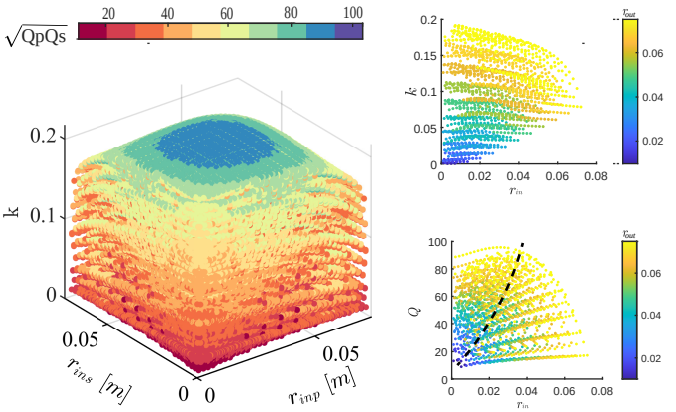

Fig. 4.15 The relation between the coil inner radius, coupling factor and quality factor. The 3D view is on left. On the right, 2D plots are shown with identical primary and secondary coils.

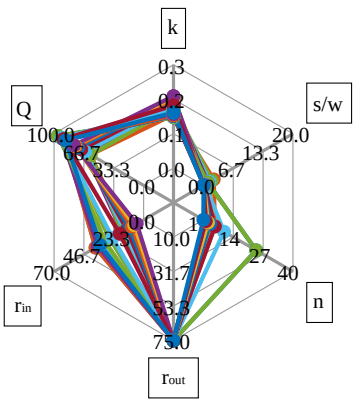

Fig. 4.16 Radar plot for designs in 500 kHz with two optimal goal k, Q as well as interesting parameters in each leg. Each color represents one design.

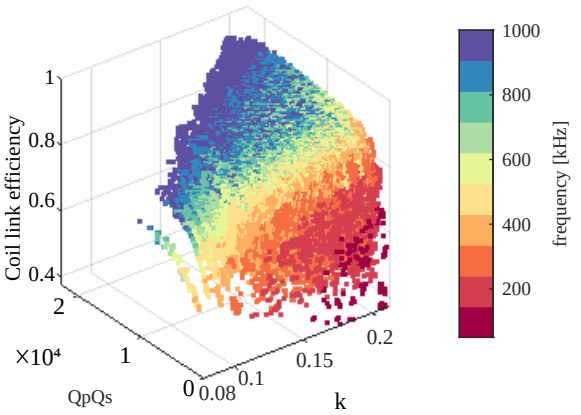

Fig. 4.17 The relation between frequency, coupling factor k, quality factor Q_pQ_s and coil link efficiency. Higher frequency leads to higher Q in the defined frequency range. The designs which have small k show stronger limit on achievable maximum Q. Higher k and Q lead to higher efficiency.

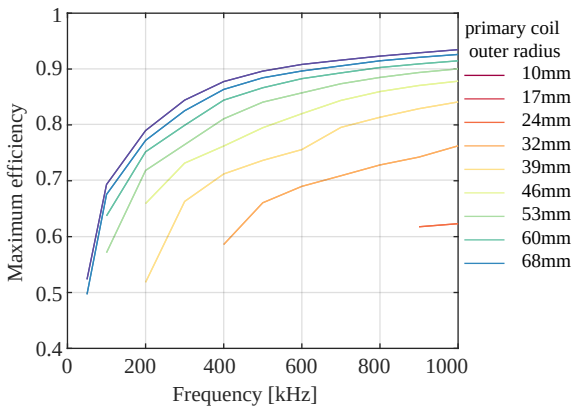

Fig. 4.18 Maximum achievable coil link efficiency under different operating frequencies and different outer radius within the design space.

In **Fig. 4.18**, although the maximum attainable coil link efficiency increases as the frequency keeps increasing, 500 kHz is chosen over 1 MHz for the experimental demonstration thereafter. Because switching at 500 kHz offers a wide choice for semiconductors, silicon devices as well as wide band-gap devices are all usable in this frequency range.

4.5.3 Pareto front

As shown in **Fig. 4.19**, trade-off between high coil link efficiency and power density exists in the IPT coil design. The coil link efficiency is from the primary coil to the secondary coil and exclude the compensation network and converters. The power density is defined as $\frac{2P_{out}}{(S_p+S_s)d}$, where P_{out} is the output power, S_p and S_s are the surface area of primary and secondary coils and d is the distance between two coils. The Pareto front for each frequency is clearly visible.

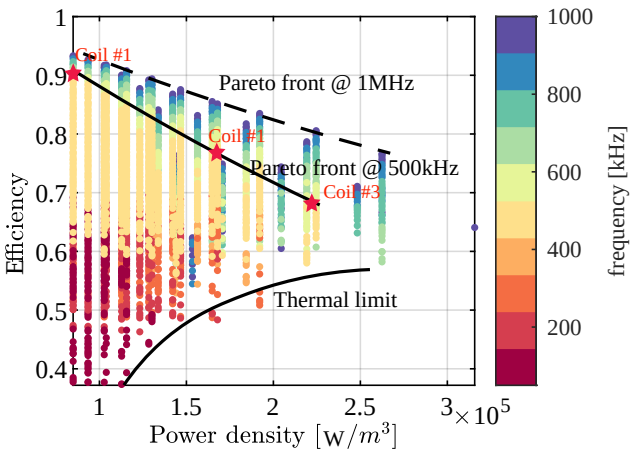

Fig. 4.19 Pareto plot of coil link efficiency and power density in the full range of design space. Three designs under 500 kHz operating frequency are selected for prototyping and marked as star in the figure.

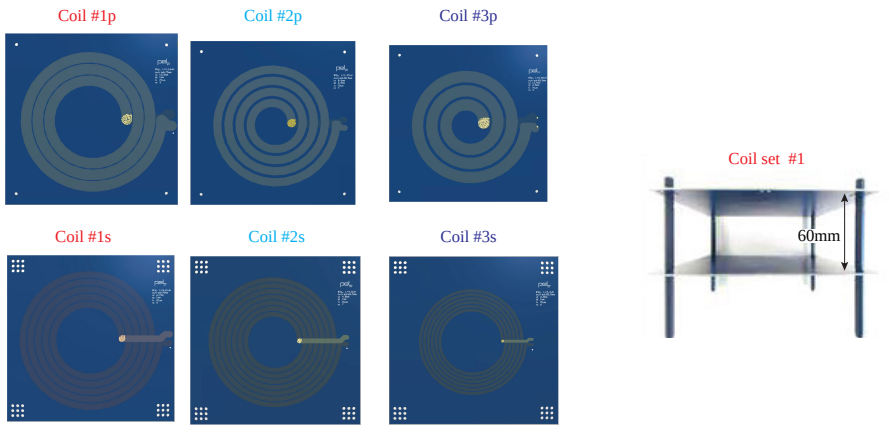

Fig. 4.20 Top view of 6 prototype coils and front view of coil set 1 with primary coil on bottom and secondary coil on top. Spaces between two coils are controlled by the length of spacers.

4.6 Experimental Verification

In **Fig. 4.19**, three designs on the Pareto front of 500kHz are selected for prototyping and the geometries of three coil sets are shown in **Tab. 4.5**. Designs are selected to verify different metrics:

- coil 1 has the highest efficiency.
- coil 3 has the highest power density.
- coil 2 takes the trade-off between efficiency and power density.

The prototype of coil pairs are shown in **Fig. 4.20**.

4.6.1 Modeling verification

The inductance and resistance modeling is verified with test using BK 895 LCR meter which has 2 % accuracy. The test is executed at 500 kHz. The resistance and inductance values obtained from both analytic modeling and test are shown in **Tab. 4.6**. The analytic model of self and mutual inductance

Tab. 4.5 Parameters of the prototyped coils

Specifications	Characteristics	Prototype I	Prototype II	Prototype III	units
primary coil outer radius	r_{outp}	75	68.5	68.5	mm
primary coil trace width	w_p	10.5	8.6	12.4	mm
primary coil turns gap	s_p	1	2.9	2.9	mm
primary coil turns number	n_p	3	4	3	-
primary coil space-width ratio	$\frac{s_p}{w_p}$	0.1	0.33	0.23	-
primary coil quality factor	Q_p	70.15	61.75	61.75	-
secondary coil outer radius	r_{outs}	75	68.5	55.5	mm
secondary coil trace width	w_s	6.7	4.8	2.9	mm
secondary coil turns gap	s_s	1	1	1	mm
secondary coil turns number	n_s	5	7	6	-
secondary coil space-width ratio	$\frac{s_s}{w_s}$	0.14	0.2	0.34	-
secondary coil quality factor	Q_s	70.7	65.8	56.1	-

Tab. 4.6 Modeling and test result of inductance and resistance of 3 coil pairs

Coil pair		$L_p[\mu H]$	$L_s[\mu H]$	$R_p[m\Omega]$	$R_s[m\Omega]$	$M[\mu H]$
1	Analytic model	1.117	3.017	50	134	0.279
	Test	1.12	3.02	48	126	0.274
	Error	$< 1\%$	$< 1\%$	3.6%	6.5%	$< 1\%$
2	Analytic model	1.18	4.736	60	226	0.302
	Test	1.24	4.74	60	240	0.3
	Error	5.3%	$< 1\%$	$< 1\%$	4.2%	$< 1\%$
3	Analytic model	0.59	4.129	30	231	0.165
	Test	0.628	4.13	42	195	0.16
	Error	6.5%	$< 1\%$	26%	18%	$< 1\%$

shows good match with the test results. The largest error of resistance 26% appears at the third prototype primary coil. This is due to the drop of resistance model accuracy for trace width larger than 10 mm. If looking into the absolute error, 26% of coil resistance corresponds to 12 mΩ which is small comparing to parasitic resistance in peripheral circuit.

The test of mutual inductance under different distances are also performed and results are shown in **Fig. 4.21**. The analytic model of mutual inductance shows high accuracy. Moreover, in order to explore the influence of lateral displacement between two coils which could happen due to wrong installation or vibrations, the test with a lateral displacement of 5 mm in each direction are executed. The misalignment in the direction xy induces the largest discrepancy and its results are shown in **Fig. 4.21**. It can be seen that small lateral displacements have negligible influence on mutual inductance.

4.6.2 Power test with a single coil pair

The first coil pair detailed in **Tab. 4.5** is tested with test-bench shown in **Fig. 4.22**. The coil set is tested with an air gap of 60 mm, load resistor of 10 Ω, input voltage of 80 V and operating frequency

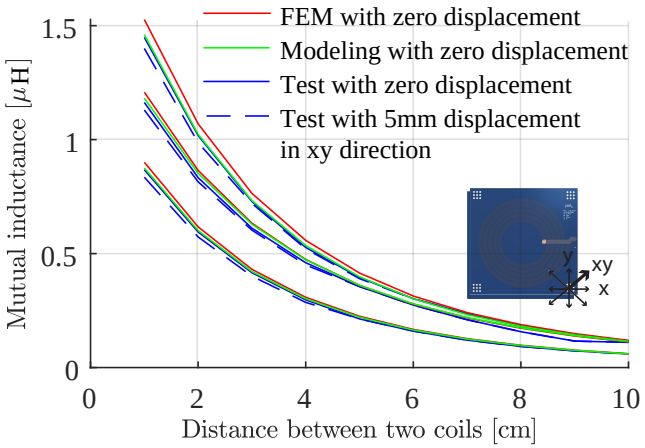

Fig. 4.21 Mutual inductance for three different coil sets under different transfer air gaps with zero or 5 mm lateral displacement in xy direction. Along with the increase of distance between primary and secondary coil, the mutual inductance drops quickly. Test result, FEM result and modeling result correlate well with each other.

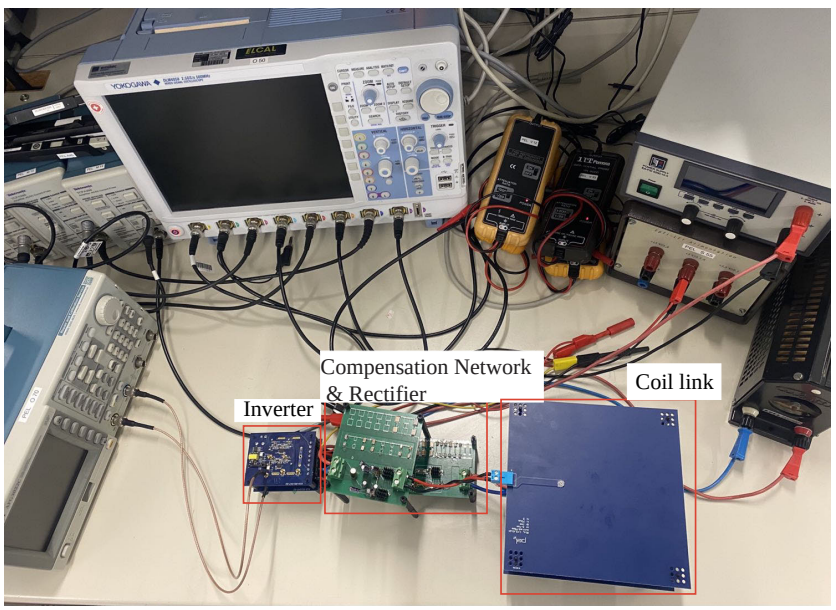

Fig. 4.22 Test setup of a inductive power transfer system composed of a 80 V DC source, the coil link and a rheostat as the load.

of 500 kHz. Other components in the test bench are as follows. The primary coil is connected to a GaN HEMTs based full bridge inverter (Infineon, EVAL-1EDF-G1-HB-GAN). The secondary coil is connected to Schottky diode based passive half bridge rectifier (ST, STPS30M60DJF). Tektronix TCPA300 (DC-100 MHz) current sensors are used to measure current. Pewatron differential probes are used to measure voltage. The LCL compensation network is used on primary side and series compensation network is used on secondary side. TDK MLCC capacitors are used due to its low ESR. TDK SPM6550CT type inductors are used for its high power and high frequency capability.

The current and voltage waveforms for this IPT system are shown in **Fig. 4.23**. With an input DC

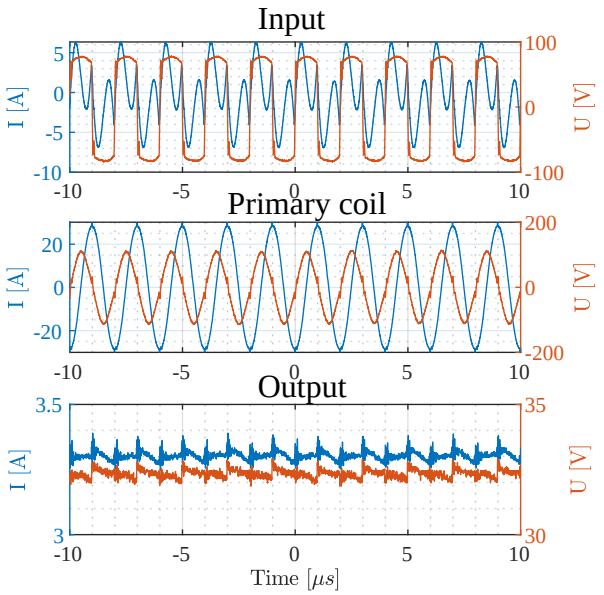

Fig. 4.23 Power test waveforms for coil pair 1. From top to bottom: Voltage and current after full bridge inverter; Voltage and current across the primary PCB coil; DC voltage and current after half bridge rectifier.

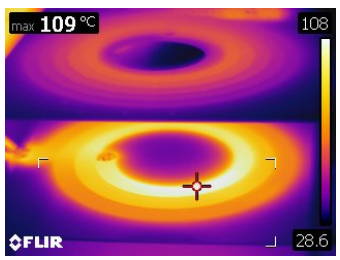

Fig. 4.24 Thermal image of coils in steady state.

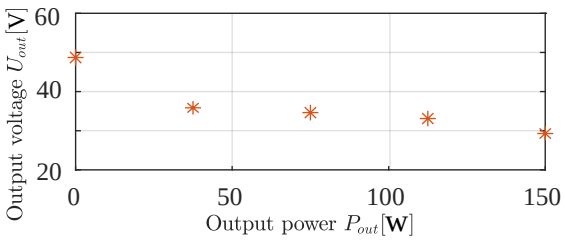

Fig. 4.25 Output voltage under various load condition for coil pair 1 with 60 mm air gap between primary and secondary coil. The load condition changes from no load condition to 150 W.

voltage of 80 V, 34 V at output is expected, however the real output voltage is 33 V. This could be explained by the parasitic resistance in the power loop and error tolerance of compensation components.

The thermal image in the steady-state is shown in **Fig. 4.24**. It can be seen that the hottest point appears in the innerest turn in primary coil, which corresponds to the modeling of magnetic field distribution in the coil. According to **Fig. 4.24**, the maximum temperature is 109 °C. In our design, the allowed maximum temperature is 125 °C. However, in our thermal model average temperature is calculated instead of highest temperature and the expected average temperature of primary coil according to (20) is 99 °C. Later in this thesis, a detailed thermal model including all the local surface temperatures is developed.

Test under different load conditions is executed. As shown in **Fig. 4.25**, the output voltage decreases as output power increases. Load condition influences the output voltage and this is because the non-zero coil resistance would share the secondary induced voltage with load. In the no load condition, the reflected impedance to the primary side is now dramatically decreased, and therefore the primary

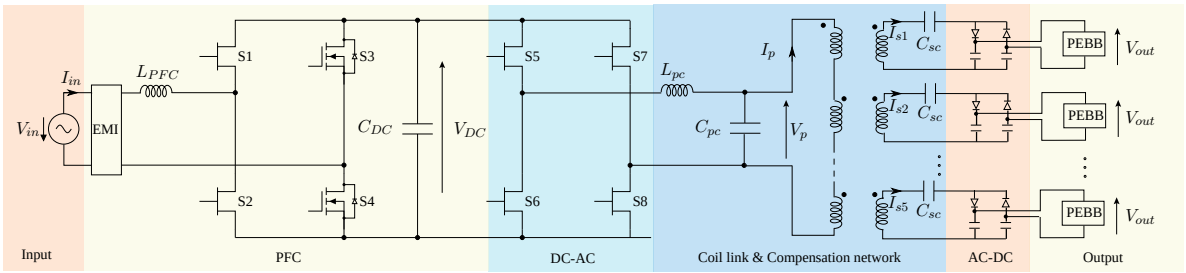

Fig. 4.26 The auxiliary power supply for PEBBs using IPT technology. Primary coils are connected in series and secondary coils are supplying modular PEBBs with independent outputs.

current increases. The induced secondary voltage increases accordingly. The current prototype is designed with safety margin to handle the no-load output voltage. Above 25% load (37.5 W), the voltage variation is within 6 V.

In conclusion, a coil prototype considering the application of auxiliary power supply in MV converters is tested with 80 V DC input, 10 Ω load, 60 mm air gap between primary and secondary coils. 33 V 110 W is obtained at output. The efficiency of the entire IPT system based on PCB coils without ferrite is 67%, including loss on the front and back power electronics converters and loss on compensation components.

4.6.3 Power test with multiple coil pairs

Following the APS structure proposed in **Chap. 3**, multiple outputs sturcture is tested together as shown in **Fig. 4.26** where the primary coils are connected in series and secondary coils are connected distinct loads. The power test is done to verify the independent outputs of the system.

The primary side converter is supplied from single phase supply and works as a constant voltage source generating ±400 V square wave voltage with 50% duty cycle and 500 kHz frequency. The AC-AC converter has two stages including the PFC stage regulating input to 400 V DC and open loop full bridge inverter stage supplying primary coils. GaN devices are applied for both Totem-pole PFC and inverter in favor of low losses. More details can be found in the master thesis [138].

For the IPT system, the output DC voltage depends on having a full bridge or half bridge topology. As discussed in **Chap. 3**, the passive half bridge is used on secondary output stage. The schottky diodes STPS30M100DJF-TR with rating 100V 30A are used to achieve low losses. The capacitor needs to be large enough to limit the 1 MHz ripples on output voltage. With nominal output ratings, 15 µF MLCC capacitors with voltage rating of 600 V are used to limit voltage ripple within 5%.

4.6.3.1 Test under nominal load

The power test have been done with five identical coil pairs with their primary coils connected in series and secondary coils supplying independent resistive loads. The primary coils get power from a single primary side converter. The distance between primary coil and secondary coil is 60 mm. The test setup is shown in **Fig. 4.27**.

The test results of one of the coil pairs are shown in **Fig. 4.28**. The output voltage is around 33 V and 108 W is transferred to each load. The voltage ripple is less than 5% of nominal value. The disturbance

observed on the voltage across primary coils are due to the measurement noises since the current through primary coils is rather clean.

4.6.3.2 Test under change of load condition

The application of LCL-S compensation network ensures independent operation of each coil pair and realizes stable output voltage on each load despite of load change on other secondary coils. This is verified by a test with load change on one secondary coil in **Fig. 4.27**. The output voltage from four coil pairs (No.2 to No.5) are shown in **Fig. 4.29**. During the test, at time t_0, the test setup is powered on with full load at each secondary coil. At time t_1, the resistive load of coil pair No.3 is fully removed. The voltage of coil No.3 increases to 60 V. In the meantime, as can be seen, the current through primary coils and output voltage on other loads (2nd, 4th, 5th outputs) are constant while the 3rd load is removed, which verifies coil pairs have independent outputs.

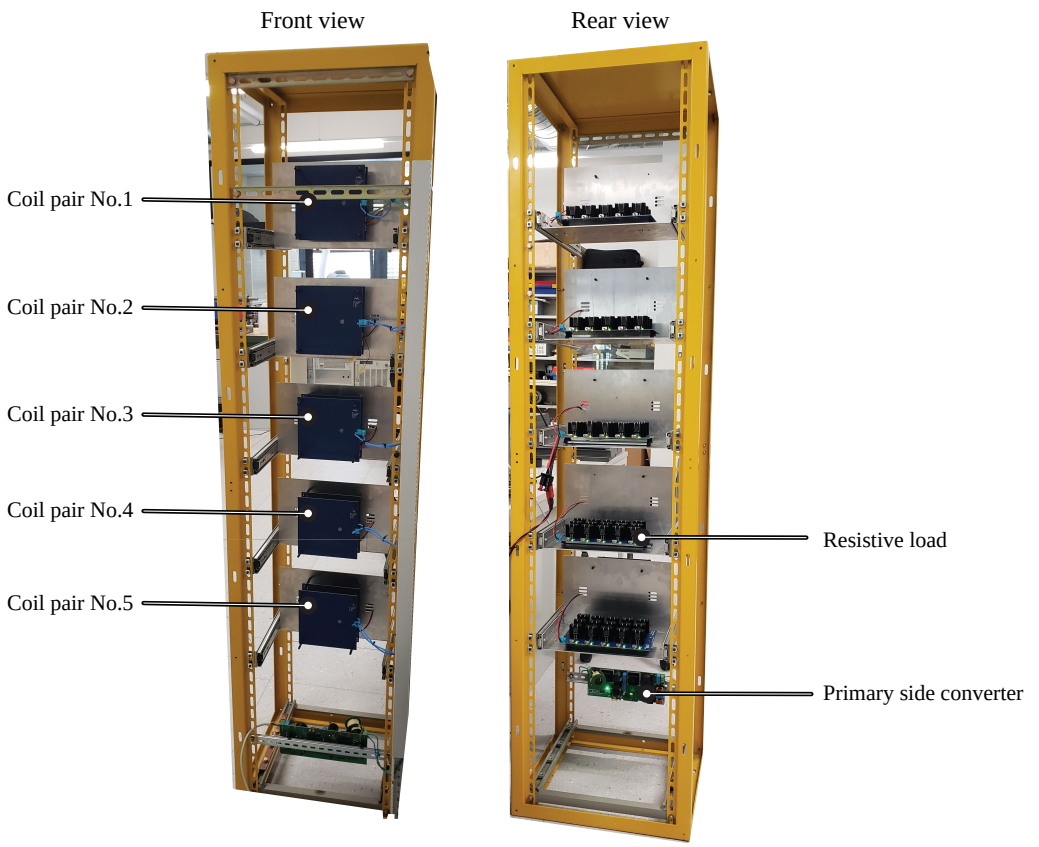

Fig. 4.27 IPT system test setup including PFC, DC-AC inverters, compensation networks, coil links, rectifiers and resistive loads. Five IPT coils pairs have their primary coils connected in series and secondary coils connected to independent loads.

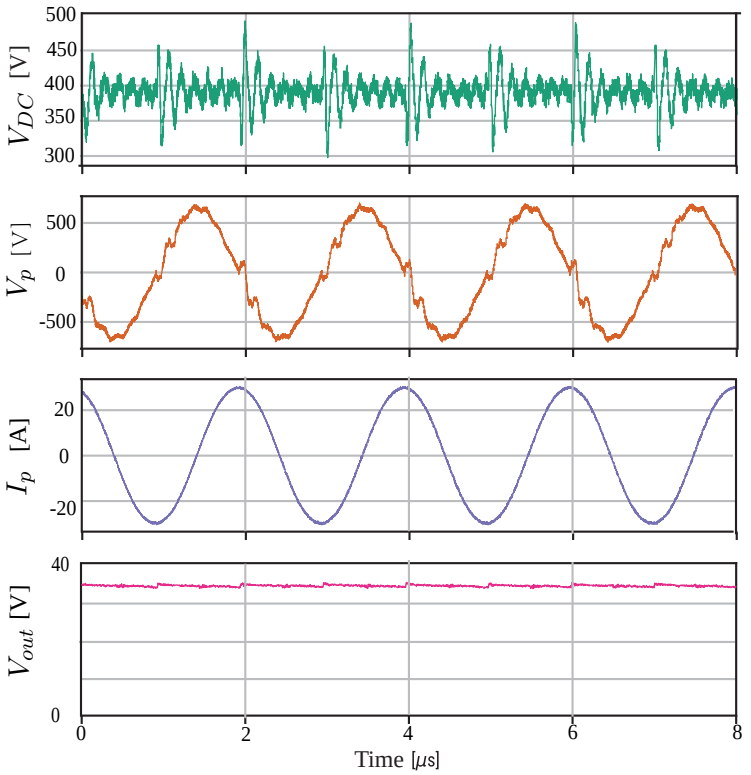

Fig. 4.28 Test waveforms of one coil pair. From top to bottom, they are: input DC voltage before the inverter; voltage across the five series connected primary coils; current through primary coils; output DC voltage at the load side of coil pair No.3.

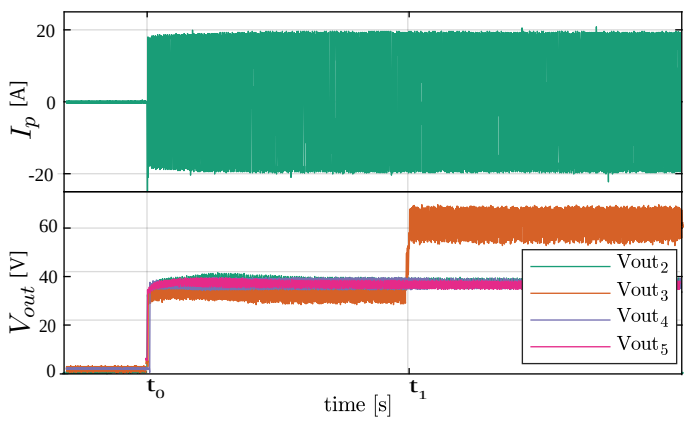

Fig. 4.29 From top to bottom: current through primary coils; output DC voltage from secondary coil to fifth coil.

4.7 Summary

This chapter focuses on the PCB coil design without ferrite in an IPT system. The main contributions of this chapter are: Firstly, an improved magnetic field distribution model for coils with rectangular cross-section offers a fast calculation approach. The model is more accurate than the filament method and faster than the FEM simulation. Secondly, the proposed model for self and mutual inductance and resistance can be used to do fast characterization of PCB coils. The accuracy of the model is especially high for trace width below 10 mm. Thirdly, by doing analysis in coil geometries we found the optimal range of $\frac{s}{w}$ is less than 1.5, and larger coil outer radius lead to high efficiency. Finally, by simply setting the design specifications and constraints, the proposed design approach could assist users with developed filters, allowing intuitive and easy navigation through a broad design space with high design freedoms. As a demonstration, a coil pair capable to transfer 110 W via 60 mm air gap is selected on Pareto front and prototyped. Firstly, the test on a single coil pair is done, and then the IPT system with five coil pairs are tested. Five primary coils are connected in series and secondary coils are supplying separate loads. The test verifies the independent outputs among coil pairs.

The coil in this chapter is composed of only PCB winding, and magnetic flux is scattered around the coil. In the next chapter, the discussion is on the cases where ferrite is added on the coil's backside offering low magnetic reluctance path and leading to a higher coupling efficiency between two coils. New models are proposed and new optimal designs are explored.

5
Modeling of PCB Windings with Ferrite on Its Backside

When ferrite is added to the backside of coils, it can significantly impact their performance. This chapter explores the influence of ferrite on IPT performance, including its effect on the coupling performance of the coil pair and losses on the coils. Various ferrite shapes are compared to optimize the coupling factor and quality factor, and the ferrite shape that exhibits the best performance is selected for the modeling process. The model, which can predict inductance and resistance of a single coil with ferrite and mutual inductance of two coils, is built with ANN. The accuracy of the model is verified with abundant FEM simulation results and with the test result on the prototype coil pair from ***Chap. 4****.*

5.1 Ferrite Effect on the Coil Pair

Magnetic materials such as ferrite are commonly used in commercial inductive power transfer products. The examples for EV charging and phone charging are shown in **Fig. 5.1**. Magnetic materials have high permeability, and by using them properly, the stray field can be reduced, and the coupling between primary and secondary coils is increased, which leads to a more compact IPT system. This is especially beneficial for applications where space is limited and size considerations need to be taken into account. Additionally, magnetic materials can act as a magnetic shield to reduce leakage of inductive field to the surrounding power conversion system, and prevent interference from external magnetic fields. While different magnetic materials can be used depending on the specific requirements and constraints of an inductive power transfer application, this thesis utilizes ferrite as the magnetic material based on the discussion in **Sec. 2.2.3**.

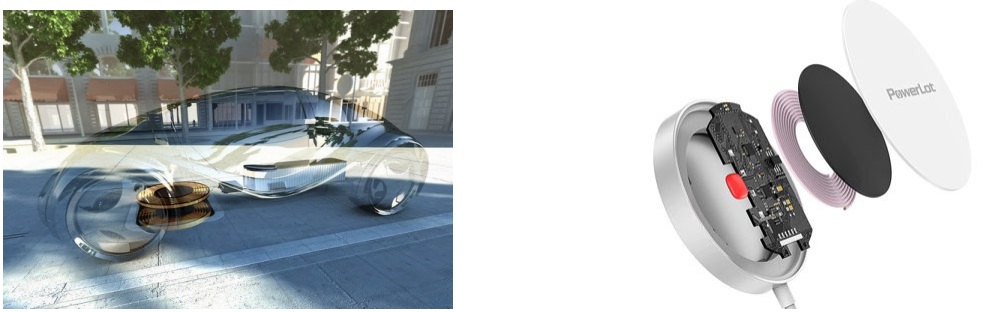

(a) (b)

Fig. 5.1 Inductive charger (a) for electric cars from Siemens (b) for mobile phones from Powerlot.

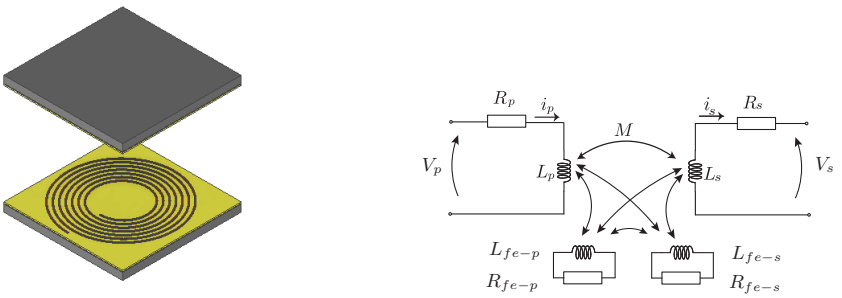

(a) (b)

Fig. 5.2 PCB coil pairs with ferrite plates on their backside (a) coil structure (b) illustration of ferrite interaction with coils (image current in ferrite).

The optimization design of an IPT system has to consider the figure of merits: coupling factor k and quality factor Q. The ferrite plate as shown in **Fig. 5.2a** will alter the magnetic field around the coil and can be modeled by the method of current images: when the ferrite plate surface area is infinitely big or much larger than the winding coverage area, the ferrite on the back side of a conductor can be modeled by an image conductor which carries the same current [139]. The image current generates magnetic field on the windings, leading to the increase of self inductance of the winding. In the meantime, the image current will introduce proximity effect on the winding and leads to high winding losses. As shown in **Fig. 5.2b**, the image current in the primary and secondary side ferrite can be modeled as inductors (L_{fe-p}, L_{fe-s}) which are coupled to the coil windings and resistors (R_{fe-p}, R_{fe-s}) reflecting the ferrite losses. In this section, the ferrite effect on the coil's coupling performance and loss in the system is qualitatively analyzed.

5.1.1 Ferrite effect on coupling between primary and secondary coils

The mutual inductance M between two coils would be influenced by the coil distance. In the meantime, unlike the case where there is no ferrite on the winding's backside and the self inductance is minimally influenced by this distance, due to the coupling between ferrite and windings, the self inductance of one coil L_p and L_s is largely influenced by the distance between two coils as well.

In a coil pair system with ferrite on their backside, when there is only current in the primary winding, the ferrite on the secondary side influences the flux distribution and therefore influences the self inductance of primary coil. This is modeled as the coupling between the primary coil L_p and secondary side ferrite L_{fe-s} as shown in **Fig. 5.2b**. Providing that the ferrite is closely fixed to the secondary winding's backside, the different distance between coils means the different distance between primary coil and secondary ferrite, which would influence their coupling. Similarly, when there is only current injected into the secondary winding, the self inductance also changes with the distance between two coils. Therefore with ferrite in the coil system, both self and mutual inductance should be discussed under different distances.

5.1.2 Ferrite effect on winding resistance

Besides coupling factor, the quality factor $Q = \frac{\omega L}{R}$ is another figure of merit to achieve high efficiency coil link. The per unit length resistance in copper windings depends on the current distribution in

coils' cross-section which is influenced by skin effect and proximity effect. The skin effect depends only on the geometry of the cross-section of coil turns. The proximity effect is caused by external magnetic field on the windings. When there is no ferrite in the system, the external magnetic field is only induced by the other turns in the same side or the opposite side windings as discussed in **Chap. 4**. When there is ferrite on the windings backside, external magnetic field on the coil windings is distorted, and therefore winding resistance is different from the coil without ferrite around it.

5.1.3 Ferrite loss

In ferrite, the hysteresis loss due to the repeated magnetization and demagnetization, and the eddy current loss induced in ferrite, constitute the total losses of ferrite. The total losses can be characterized through empirical Steinmetz equation [140]. This can be applied because the excitation of the coils is sinusoidal and without DC premagnetization of the material. The total losses are calculated by integrating loss density over the volume of ferrite core. The loss density inside the ferrite is

$$P_{\text{lossdensity,fe}} = C_m f^x B^y (Ct_2 \cdot T^2 - Ct_1 \cdot T + Ct)[\frac{W}{m^3}] \tag{5.1}$$

where, frequency f is in [Hz], flux density B is in [T] and operating temperature T is in [$^\circ C$]. Taking ferrite material 3F36 as an example, the Steinmetz parameters of frequency from 500 kHz to 800 kHz are extracted from its data sheet: C_m = 1.12e−4, x = 2.1952, y = 2.7199, Ct_2 = 8.926e−5, Ct_1 = 1.172e−2, Ct = 1.282. In the temperature range from 25$^\circ C$ to 120$^\circ C$, the temperature influence "$Ct_2 \cdot T^2 - Ct_1 \cdot T + Ct$" is in range [0.9, 1.2]. In this chapter, the temperature influence is considered to be 1, and the Steinmetz equation for 3F36 ferrite material becomes

$$P_{\text{lossdensity,fe}} = 1.12e-4 f^{2.20} B^{2.72}[\frac{W}{m^3}] \tag{5.2}$$

In (5.2), under constant frequency, the loss density is influenced only by magnetic flux density B. When the current changes from 1 A, based on Maxwell equations, the magnetic flux density B changes proportionally and therefore the ferrite loss density and total ferrite loss change to the power of 2.72. In the same time, the copper loss changes with the current to the power of 2. Hence, the ferrite loss is increasing faster than the copper loss when the current through the winding increases.

5.2 Ferrite Geometry Discussion

There are various realizations of ferrite geometries including surface shapes and thickness. This section aims to compare the different shapes and thickness of ferrite and find the optimal solution. Quality and coupling factors are taken as the figure of merits to evaluate coil performance.

5.2.1 Ferrite shapes comparison

Three different ferrite geometries are considered here: the round surface planar ferrite, the rectangular surface planar ferrite and ferrite strips. Ferrite strips can usually be seen in high power range applications and the ferrite arrangement could be optimized for better cooling and lower mass [141]–[143], however ferrite partially covering the coil surface sacrifices coupling factor and efficiency. On contrary, the round surface and rectangular surface ferrite plates exhibit high coupling factor.

Various ferrite shapes are simulated and tested with the proposed PCB based IPT coils from **Chap. 4** for the comparision purpose. The winding geometry parameters are repeated in **Tab. 5.1**. Round ferrite plate, rectangular ferrite plate and ferrite strips are shown in **Fig. 5.3** and the geometry parameters are listed in **Tab. 5.2**. The simulation and test are done with operational frequency at 500 kHz. With Ansys Maxwell, the coupling factor, copper loss and ferrite loss are evaluated. The ferrite material 3F36 is used due to its optimal operating frequency up to 1 MHz, high maximum B reaching 420 mT at 100˚C, 1200A/m, and a flat losses responses over a wide temperature range from 0˚C to 120˚C, as discussed in **Sec. 5.1.3**.

5.2.1.1 Flux distribution of different ferrite shapes

The view on flux distribution could give an intuitive understanding of ferrite effect on coils. FEM could be used to simulate the magnetic field distribution inside ferrite. With the coil pair in **Tab. 5.1** and the electric specifications and the IPT system structure in **Chap. 4**, the nominal current on the primary side is 20 Arms and the current on the secondary coil is 6 Arms. In the simulation, two windings are injected with 20 A and 6 A separately to simulate both the primary and secondary current through coil winding. The distance between two coils is set to 20 mm which is the minimum achievable distance considered in this thesis, and shows the strongest coupling effect between two coils. FEM simulations are done with Maxwell 3D with eddy current solver. The boundary conditions use the default boundaries: Natural and Neumann boundaries. The automatic adaptive meshing is used with 30 maximum number of passes, 0.5% energy error is the convergence criteria.

With 500 kHz current in the coil windings, the flux density distribution in different ferrite shapes are shown in **Fig. 5.3**. In the rectangular ferrite plate, the iso-flux lines are circular at the center and gradually transition to a square shape near the edges. The flux is concentrated on the corner due to the edge effect [144], which also results in the highest magnetic flux density B_{max} = 95.8 mT appearing on the ferrite strips on one corner. The unsymmetrical distribution is a result of the windings being in an unsymmetrical spiral shape instead of a co-circular shape. In the circular ferrite plate, the iso-flux-line is in circular shape, and the flux is concentrated underneath the inner turns of winding. In the ferrite strips, the flux has band shape, and the maximum flux density appears at the corner of the ferrite strip. The integration of flux inside different ferrite shapes are shown in **Fig. 5.3** as well. The high total flux would lead to higher inductance but more losses. It can be seen that the total flux in the square ferrite is the largest among the three shapes and almost doubles the total flux in the strips, which could be explained by the fact that the strips occupy only about 50% area of the coil surface area.

Tab. 5.1 Coil geometries under simulation with different ferrite shapes

Specifications	Characteristics	values	Characteristics	values
	Primary coil		Secondary coil	
outer radius	r_{outp} [mm]	75	r_{outs} [mm]	75
trace width	w_p [mm]	10.5	w_s [mm]	6.7
turns gap	s_p [mm]	1	s_s [mm]	1
turns number	n_p	3	n_s	5
PCB thickness	$th - pcb_p$ [μ m]	95	$th - pcb_s$	95
inductance without ferrite	L_p [μH]	1.12	L_s [μH]	3.02

Tab. 5.2 Ferrite geometry parameters for three shapes: round, square and strip ferrites

shape	Geometry characteristics	values	units
Round ferrite plate	radius r_{fe}	75	mm
	thickness t_{fe}	5	mm
	volume V_{fe}	88	cm^3
Square ferrite plate	side length l_{fe}	150	mm
	thickness t_{fe}	5	mm
	volume V_{fe}	112	cm^3
Ferrite strips	length × width $l_{fe} \times w_{fe}$	150×10	mm^2
	space between strips s_{fe}	10	mm
	thickness t_{fe}	5	mm
	volume V_{fe}	64	cm^3

5.2.1.2 Coupling and quality factors at different distances

FEM simulations are done for the same coil pairs under different distances to evaluate the coil pair performances. Considering 6 kV working voltage of the converter, and considering the insulation coordination between primary and secondary coils could be realized by either solid insulation or air insulation, the distance from 20 mm to 100 mm between primary and secondary coils is a reasonable range and is simulated in FEM. Coupling and quality factors of coil links with different ferrite shapes are shown in **Fig. 5.4**. First of all, by looking at the trend with different distances, we can conclude that when the coils are placed further to each other, the coupling of two coils $k = \frac{M}{\sqrt{L_p L_s}}$ decreases as shown in **Fig. 5.4a**, while the quality factor of both primary and secondary coil Q_p, Q_s slightly increase as shown in **Fig. 5.4b** and **Fig. 5.4c** due to the decrease of winding loss. Losses in both winding and ferrite decrease with larger distance as shown in **Fig. 5.4d** and **Fig. 5.4e** because coupled flux induces high proximity loss in winding, and higher flux density in ferrite induces higher core loss.

Considering coupling factors, as shown in **Fig. 5.4a**, it can be seen that the rectangular shape has the highest coupling factor, while the ferrite strips offer lowest coupling factor. This can be explained by the volume area of ferrite plates as shown in **Tab. 5.2**. Considering quality factors, as shown in **Fig. 5.4b** and **Fig. 5.4c**, round shape and rectangular shapes show better performance than ferrite strips. It is important to observe that the core loss is much smaller than the copper loss thanks to the low flux in ferrite. In addition, there are larger core losses in the strip cores than the round and rectangular shape cores, which can be explained by the high peak flux density in ferrite strips.

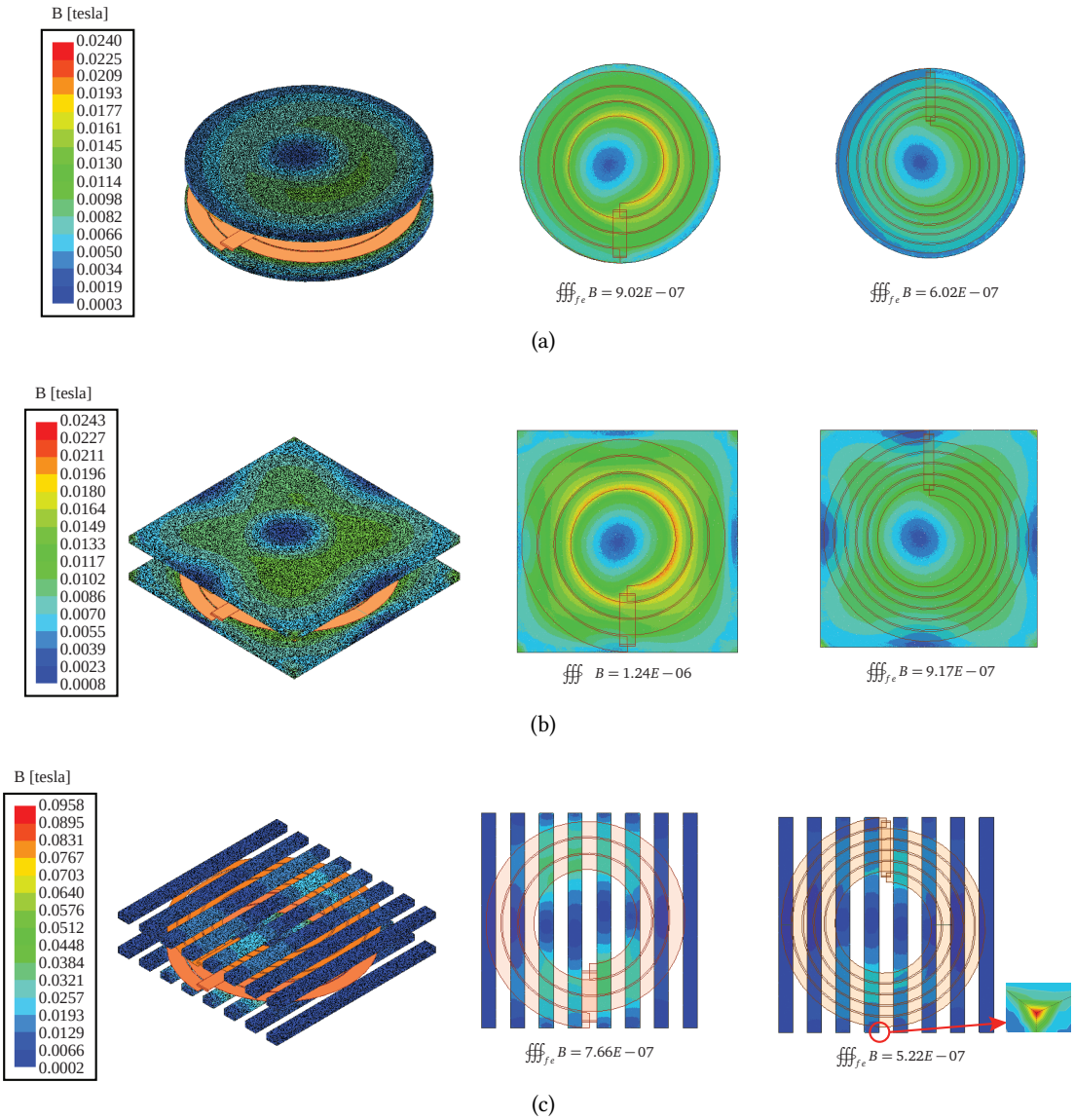

Fig. 5.3 The flux density in the ferrite of one coil pair system with different ferrite shapes under 500 kHz current and 20 mm distance between primary and secondary coil (a) round shape ferrite (b) rectangular shape ferrite (c) ferrite strips.

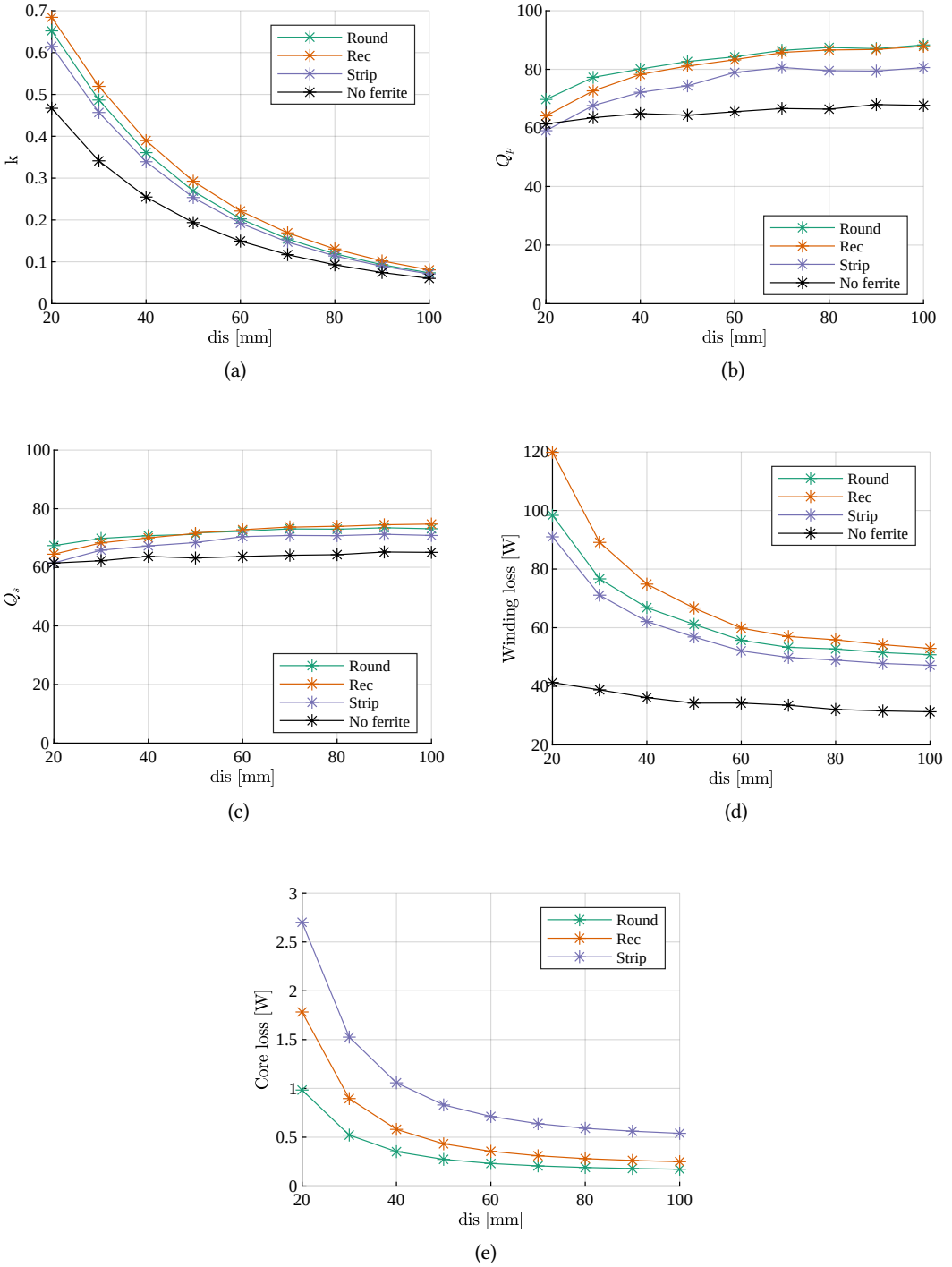

Fig. 5.4 FEM simulation of one coil pair system with different ferrite shapes under 500 kHz current (a) coupling factor (b) quality factor of primary coil (c) quality factor of secondary coil. (d) total losses in both primary and secondary winding (e) total losses in both primary and secondary ferrite.

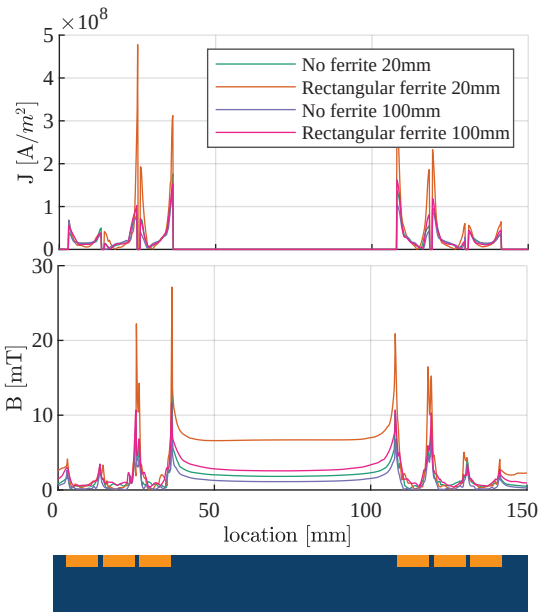

Fig. 5.5 The current density and magnetic flux density distribution along the cross section of the primary coil. Four cases are shown: without ferrite and with rectangular shape ferrite on the coils back side with coil distance of 20 mm and coil distance of 60 mm.

Extra comparison is done with the coil without ferrite. As can be seen in **Fig. 5.4a**, the adding of ferrite regardless of ferrite shapes shows higher coupling factor comparing to coils without ferrite in presence. The coil pair with ferrite demonstrates also high quality factor as shown in **Fig. 5.4b** and **Fig. 5.4c**. Based on the discussion in the previous section, the presence of ferrite would cause current crowding effect inside the windings and therefore increase the winding loss as shown in **Fig. 5.4d**. The current crowding effect is illustrated in **Fig. 5.5**, the current distribution along the primary winding cross section as well as the magnetic flux density distribution is shown, where the square ferrite shape is used. The spikes of current density happens on the surface of each turn of copper winding and is much higher with the existence of ferrite than the coil without ferrite.

Based on the results presented in **Fig. 5.4**, it's evident that the round shape ferrite and rectangular shape ferrite are dominating in performances. In addition, round ferrite plates take up less volume and therefore allow more space for the layout of other components on the PCB. Therefore round shape ferrite is chosen to be placed on the back side of PCB winding fully covering the winding area.

5.2.1.3 Verification of FEM simulation results with impedance analyzer

The previous discussion is based on the FEM simulation, in this section, the impedance obtained with FEM simulations are verified with impedance analyzers. The rectangular shape ferrite shown in **Tab. 5.2** is manufactured and tested. The self inductance of each coil and mutual inductance of the coil pair is measured by BK 895 (1 MHz LCR meter), by Bode 100 impedance analyzer and by the power choke analyzer as shown in **Fig. 5.6**. For LCR meter, the test is done under 500 kHz with 1 Vrms test voltage. The test accuracy under 500 kHz for 1 µH to 1 mH is 0.65%. With Bode 100, the test is done with impedance adaptor, the impedance is derived by evaluating the internal source voltage and the output voltage. The series inductance and series resistance are then calculated from

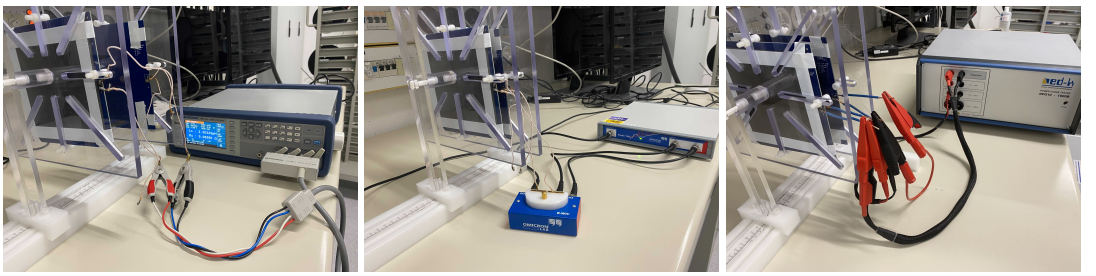

(a) (b) (c)

Fig. 5.6 Test setup (a) test with LCR meter (b) test with Bode 100 (c) test with power choke analyzer.

$Z = R + j\omega L$. The sweeping frequency is from 50 Hz to 1 MHz, and the value at 500 kHz is extracted and then compared with the result from LCR meter. The power choke tests object under DC voltage and inductance is acquired by the incremental speed of current with an accuracy around 1%.

The inductance test results together with FEM simulation result are shown in **Fig. 5.7**. The tests with three different measurement equipments show high correlation which means the test result is trustworthy. The difference between test and FEM results is within 7% for both primary coil and secondary coil. In addition, what can be clearly seen in this figure is the dramatic decline of both self and mutual inductance with the increase of distance between coils. The decline of the self inductance is within 30% and stems from the longer distance between one coil and the ferrite in another coil. The mutual inductance shows a phenomenal and sharp drop to almost zero which results from the loose coupling between two coils at long distance.

The AC resistance of the coil is tested with LCR meter and Bode 100 impedance analyzer. During test, the excitation is added on the winding of one coil, and the winding on the other coil is left open circuit. During the test, extra wire is connected to the windings to do the test and is causing extra resistance around 15 mΩ and therefore this resistance caused by additional wire is taken into consideration and reduced in the test resistance. The resistance caused by loss on ferrite is omitted and the tested coil resistance is compared with winding resistance. This is because the FEM results show that the loss in ferrite is more than one hundred times smaller than the winding loss when the input current is smaller than 1 Arms. The tested resistance together with FEM result is shown in **Fig. 5.8**.

As shown in **Fig. 5.8**, the test results match well with FEM results. The error between the FEM and test results is within 5%. In addition, the test results have shown good correlation between the Bode 100 and LCR meter. It's worth noting that when the the distance is smaller than 30 mm, 1 mm of distance variance could cause more than 5 mΩ resistance difference.

Similar to the test on rectangular shape ferrite, the LCR meter is used to characterize round shape ferrite and ferrite strips as well. And the results are shown in **Fig. 5.9**. Based on the test on coils with different ferrite shapes, we can conclude that the LR characteristics extracted from FEM are trustworthy.

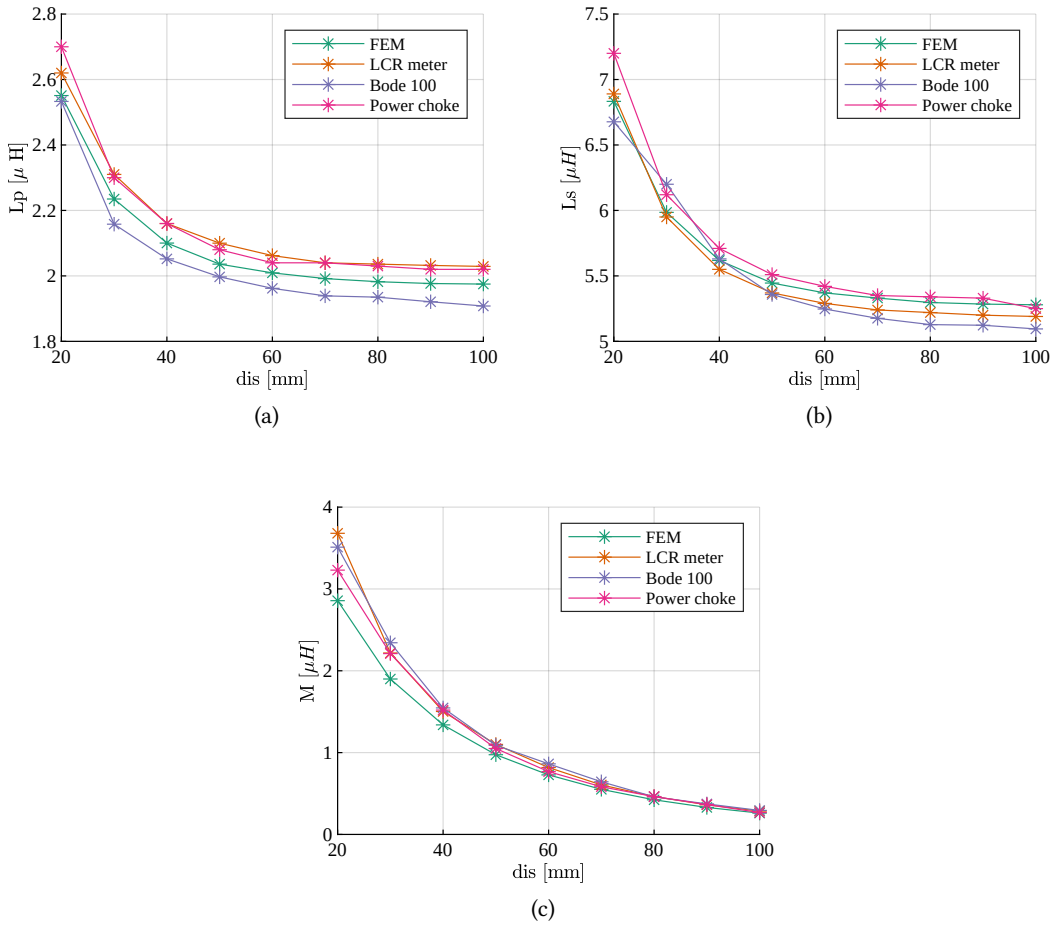

Fig. 5.7 FEM result and test result of coils with rectangular ferrite plates (a) primary coil inductance (b) secondary coil inductance (c) mutual inductance of the coil pair.

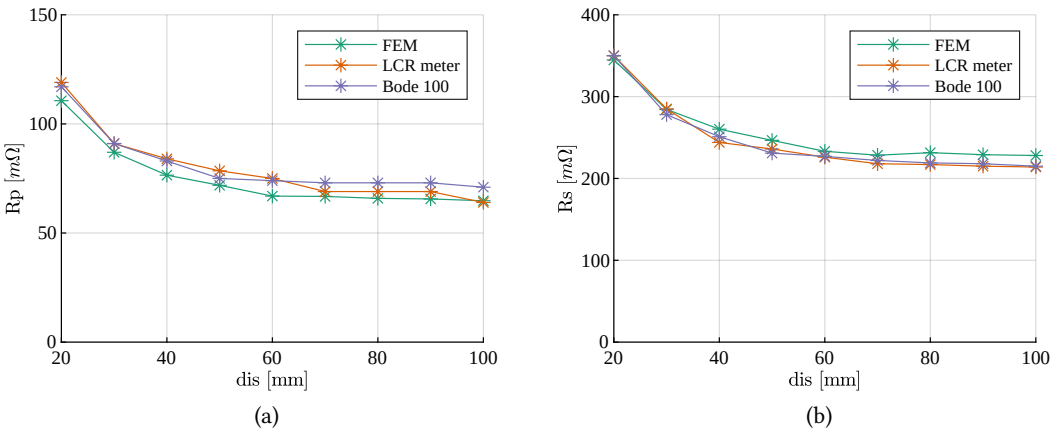

Fig. 5.8 Resistance at 500 kHz FEM result and test result of coil pair with rectangular ferrite plates (a) primary winding resistance (b) secondary winding resistance.

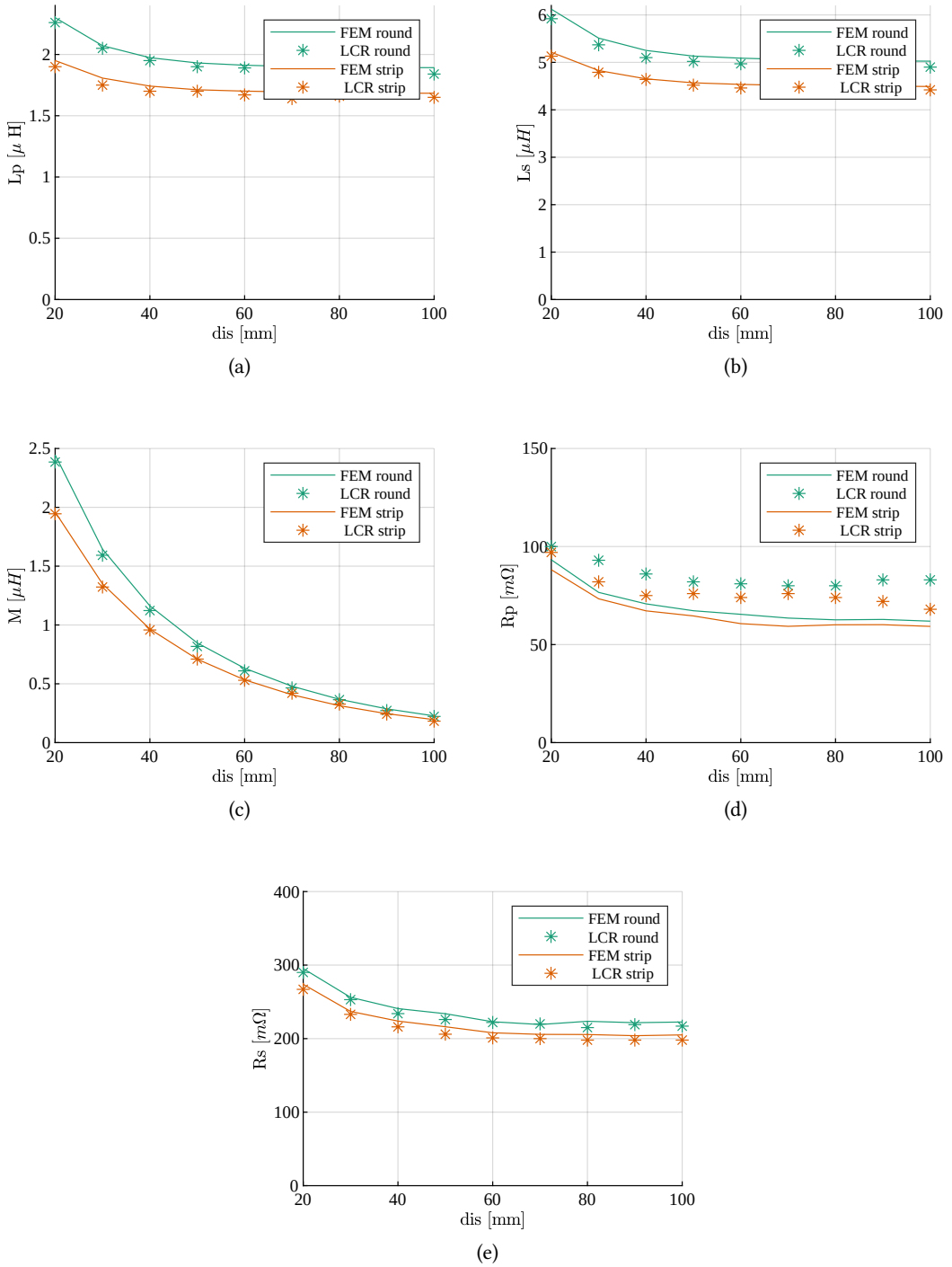

Fig. 5.9 FEM result and test result of coils with round ferrite plates and with ferrite strips (a) primary coil inductance (b) secondary coil inductance (c) mutual inductance of the coil pair. (d) primary winding resistance (d) secondary winding resistance.

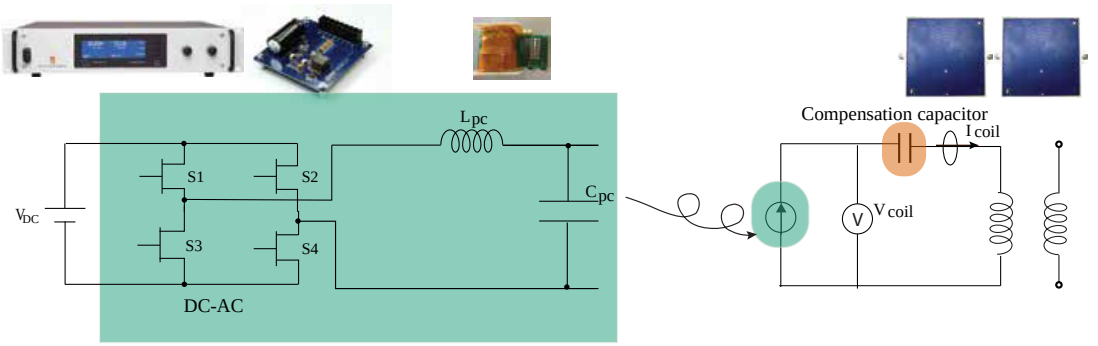

Fig. 5.10 The test bench composed of controlled current source (composed of DC voltage source, GaN based inverter and the LCL resonant network), compensation capacitor and the coil pair under test.

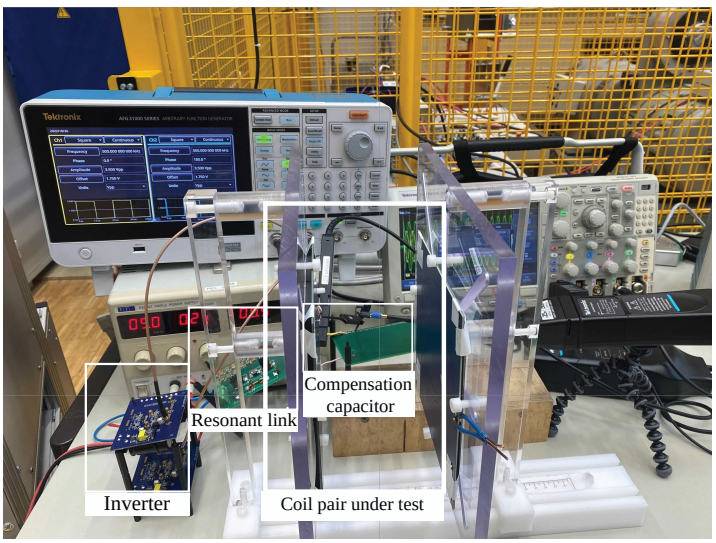

Fig. 5.11 The photo of the test bench illustrated in **Fig. 5.10**.

5.2.1.4 Verification of FEM simulation results with power test

The test with impedance analyzer is used to verify winding resistance extracted from FEM, while ferrite losses are ignored. This is because with impedance analyzer, the excitation current through coil pair is below 1 Arms and the loss in ferrite is hundred times smaller than the winding loss. In this section, the current through coil is increased by power test and the total losses in both winding and ferrite obtained from the simulation are verified. Same as the test with impedance analyzer, while one coil is connected to the power supply, the other coil is left open circuit. The power test is done by connecting the primary and secondary coil respectively to the controlled current source composed of DC voltage source, GaN based inverter and the LCL resonant network as shown in **Fig. 5.10** and **Fig. 5.11**. Sourced from the DC voltage source, the GaN inverter outputs voltage in square waveform at 500 kHz operating frequency. The LCL resonant link design with resonance frequency of 500 kHz converts the square waveform to a sinusoidal waveform, and outputs constant current to the coil winding. The Tektronix IsoVu isolated probe is used for voltage sensing. Tektronix TCP305A with amplifier TCPA300 is used for current sensing. Tektronix MDO3104 oscilloscope is used.

The coil pair with 5 mm thick rectangular shape ferrite plates is tested. The loss is measured by

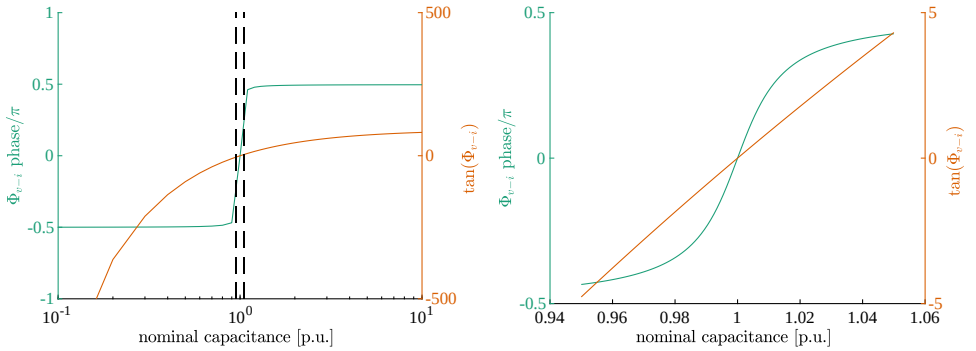

Fig. 5.12 The sensitivity to compensation capacitance. Left axis: phase difference between voltage and current; right axis: sensitivity of loss error (a) the nominal capacitance is from 0.1 to 10, the dashed lines mark the boundary of $tan(\Phi_{v-i}) < 5$ (b) the zoom in of figure (a) with the $tan(\Phi_{v-i}) < 5$.

averaging the product of the sensing winding voltage and the current through the winding. During the measurement process, phase error is unavoidable due to the different delay times of the voltage and current probes. In the case of testing the loss of a coil, a little phase discrepancy error in measurement will cause significant loss error for the following reasons. Normally the reactance of coil under high frequency is much larger than the resistance, the phase angle difference between tested voltage and current is close to 90°. Under sinusoidal excitation, the sensitivity to voltage and current phase difference and the measurement error is $\triangle P_{loss} = tan(\Phi_{v-i}) \times \triangle\Phi_{v-i}$ [145], where $\triangle P_{loss}$ is the loss error; Φ_{v-i} is the phase angle difference between the voltage and current over the test object; $\triangle\Phi_{v-i}$ is the phase measurement error. From this equation, it can be concluded that, under a constant phase measurement error $\triangle\Phi_{v-i}$, in order to reduce the test power error $\triangle P_{loss}$, $tan(\Phi_{v-i})$ should be minimized.

In order to measure accurately the power loss on the coil, it's necessary to minimize the measured voltage and current phase difference. A compensation capacitor can be placed in series to the coil as shown in **Fig. 5.10** and instead of measuring the voltage over the coil, the voltage across the series branch of the compensation capacitor and the tested coil is measured. It's hard to perfectly compensate the coil with commercially available capacitors ($C = \frac{1}{w^2 L}$), therefore the sensitivity of the compensation capacitance needs to be analyzed. Taking the primary coil as an example which has inductance of 2 µH and resistance of $70m\Omega$ under 500 kHz, the sensitivity of phase difference between the voltage and current as well as the loss error sensitivity to the compensation capacitor is shown in **Fig. 5.12**, where the capacitance is refereed to its base value $\frac{1}{w^2 L}$. The sub-figure (b) is the zoomed in version of sub-figure (a). It can be seen that when the compensation capacitance is within the range ±6% to the base value, $tan(\Phi)$ is smaller than 5. Eventually, the compensation capacitance used here is tested to be 52.4 nF which equals to 1.03 p.u.

The measured voltage and current in both with and without compensation capacitor situations are shown in **Fig. 5.13**. The frequency spectrum of voltage and current, and the phase difference between current and voltage is shown in **Fig. 5.14**. The phase difference Φ_{v-i} at 500 kHz is reduced from 0.483 rad to 0.403 rad and $tan(\Phi_{v-i})$ is reduced from 18.7 to 3.1. Therefore with the compensation capacitor,

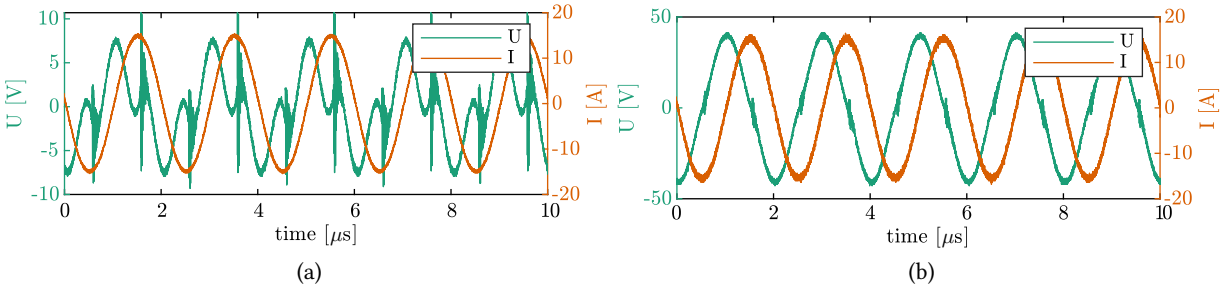

Fig. 5.13 The voltage and current waveform with different compensation network (a) with compensation capacitor (b) without compensation capacitor.

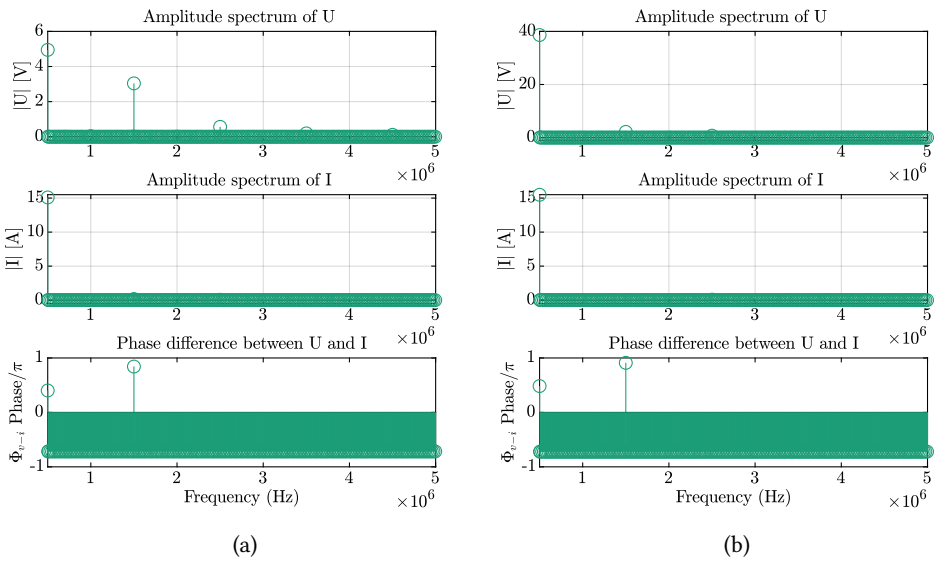

Fig. 5.14 Fourier analysis of the voltage and current through coils (a) with compensation capacitor (b) without any compensation capacitor.

the power loss measurement error is reduced five time and is now $\triangle P_{loss} = 3.1 \times \triangle \Phi_{v-i}$.

In the setup shown in **Fig. 5.11**, in addition to the resistance of coil, there are parasitic resistance introduced by the compensation capacitor, wires and connection points and the injection resistance from the current probe. In order to measure this parasitic resistance, the coil is short circuited and the rest circuit between the voltage probes are tested with LCR meter. The current source circuit is disconnected from the test circuit and the current probe stays in the test circuit and two terminals of coil is short circuited. The results show a parasitic resistance of 37 mΩ. The measured power loss on the coil includes both the loss on the coil and the parasitic resistance. The loss on coil is obtained by deducting the loss on parasitic resistance from the tested loss.

In order to verify the accuracy of power loss results from FEM, the comparison between FEM results and power test results are shown in **Fig. 5.15**. The results show good correlation between the loss from FEM and the tested loss.

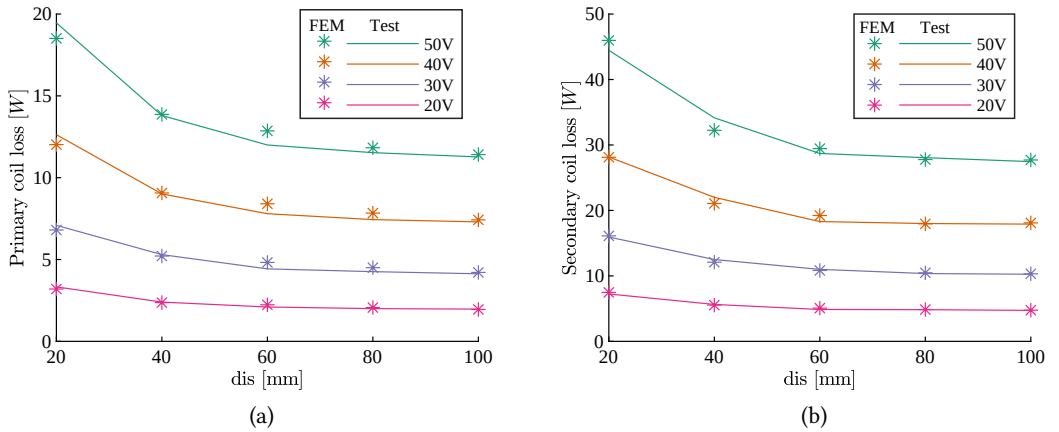

Fig. 5.15 Loss over one coil. '-' lines represent power loss tested by integration of product of measured current and voltage. '*' stars represent power loss calculated by the product of resistance simulated in FEM and tested current (a) current excitation through primary coil (b) current excitation through secondary coil.

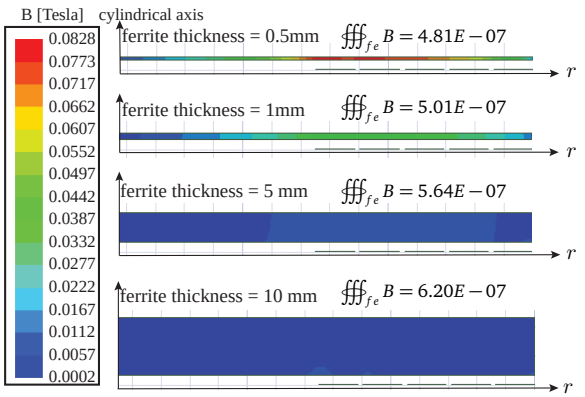

Fig. 5.16 The magnetic flux density distribution at 0 degree inside ferrite plate on the back side of the secondary coil and the integration across the ferrite cross-section area.

5.2.2 Ferrite thickness comparison

With the same shape and surface area of ferrite, the thickness of ferrite would influence the penetration of flux. With the same winding geometry, ferrite thickness from 0.1 mm to 10 mm is simulated in FEM under three different distance between coils. In order to speed up the simulation, the Maxwell 2D FEM simulation in cylindrical coordinate system is used. The balloon boundary condition is used. The automatic adaptive meshing is used with 20 maximum number of passes and 1% energy error as the convergence criteria. In **Fig. 5.16**, the flux density B in the half cross section area of round ferrite plate with different thickness on the secondary coil side is shown, as well as the integration of magnetic field in the ferrite. Thicker ferrite results in a higher total flux within the material, as more flux prefers to take the low reluctance path through the lateral surface of the ferrite. Nevertheless, it is worth noting that the increase in total flux is relatively small compared to the corresponding increase in ferrite thickness. In the meantime, magnetic flux density B is higher in the thinner ferrite.

Coupling and quality factors extracted from FEM are shown in **Fig. 5.17**. From subfigure (a), it

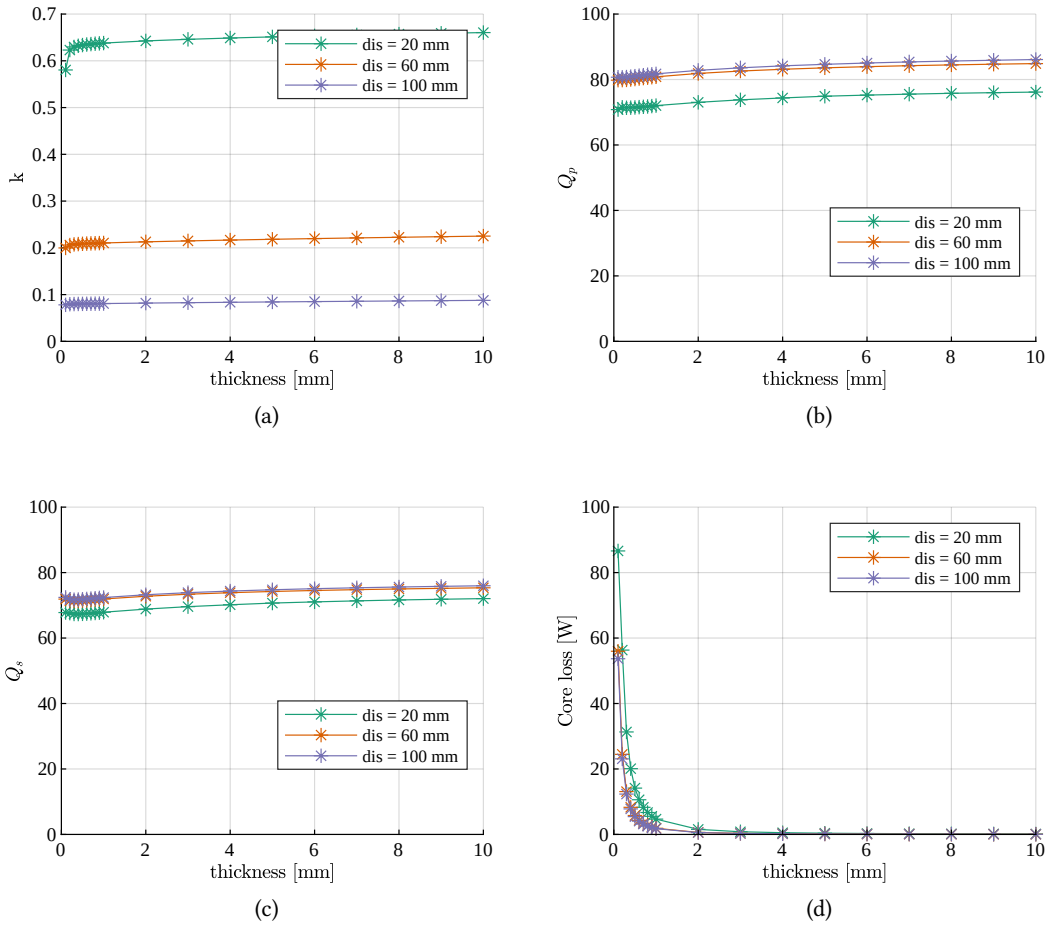

Fig. 5.17 FEM result of the coil pair with different ferrite thickness (a) Coupling factors (b) quality factor of primary coil (c) quality factor of secondary coil (d) losses in ferrite.

can be seen that with the increase of thickness, the coupling between coils is slightly better, which corresponds to the observation in **Fig. 5.16** that when the ferrite is thicker, there are more flux through it. As shown in **Fig. 5.17b** and **Fig. 5.17c**, under the same distance, the quality factor of coils increases with thicker ferrite. When the distance between two coils is higher, the quality factor increases with the same ferrite thickness, which matches with the analysis in **Fig. 5.4**. As shown in **Fig. 5.17d**, the core loss decreases dramatically with the the increase of ferrite thickness. This can be explained by that, there is high magnetic flux density B in the thinner ferrite especially when the thickness is lower than 1 mm, and the power loss is approximately proportional to the $B^{2.72}$ for 3F36 material. Therefore, even though the ferrite volume is low in thin ferrite, the total loss is still high. In **Fig. 5.17**, the turning point for both coupling factor and loss appear around 0.6 mm to 1 mm of thickness, the power transfer efficiency is dramatically lowered for thicknesses below 0.6 mm which corresponds to existing findings [146]. Ferrite with thickness more than 1 mm offers better coupling and introduces lower core losses to the IPT coil link.

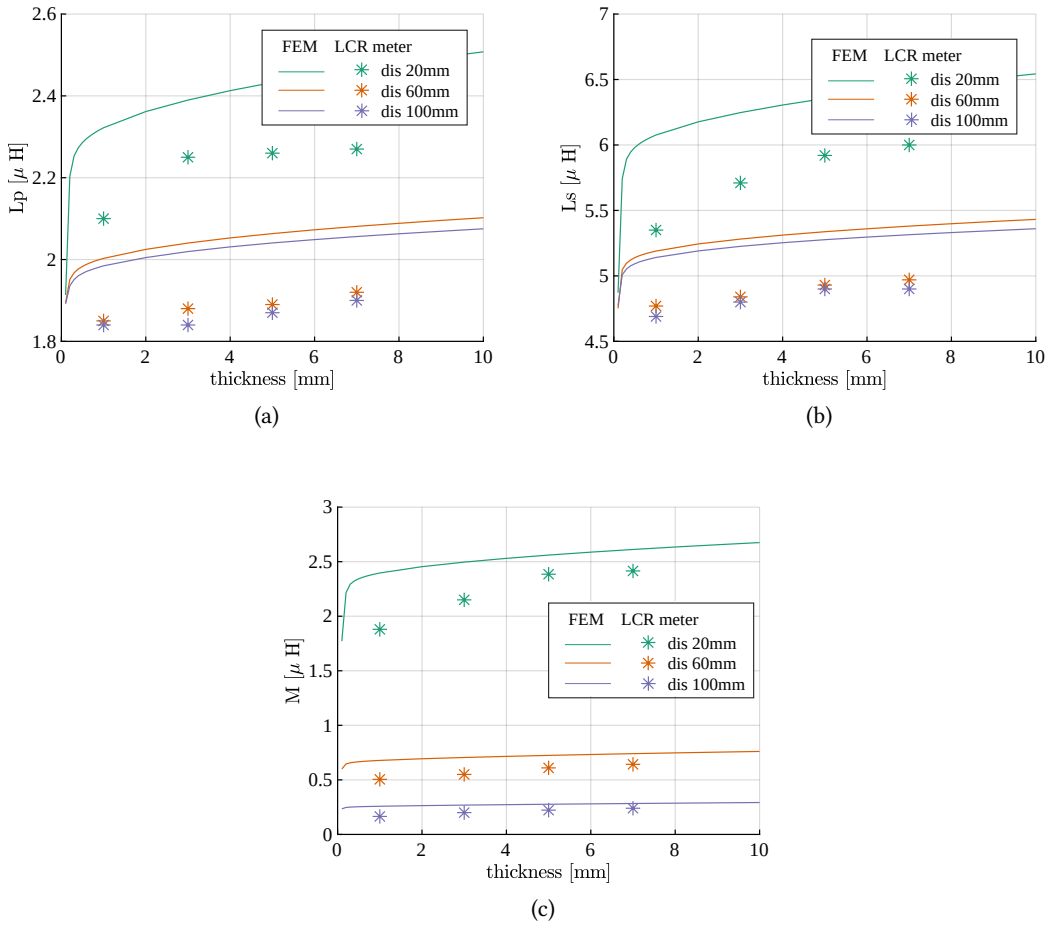

Fig. 5.18 FEM result and LCR test test result at 500 kHz (a) primary coil inductance (b) secondary coil inductance (c) mutual inductance.

5.2.2.1 Verification of FEM simulation results with impedance analyzer

The coils with different ferrite thicknesses are prototyped, and are tested with impedance analyzer in order to verify the results from FEM. The comparison between FEM and test results are shown in **Fig. 5.18** and **Fig. 5.19**. The difference of inductance is less than 0.2 μH for primary coil and less than 0.7 μH for secondary coil. The difference between FEM and test results for winding resistance is less than 25 $m\Omega$ for primary winding and 50 $m\Omega$ for secondary winding. When compared to the results for rectangular shape ferrite in the last section, the difference between FEM simulation and test resistance is relatively larger, this is because the FEM simulations are done in 2D, and therefore the spiral windings are simplified to co-axial circular windings. Based on the test results, the analysis in **Sec. 5.2.2** under different thickness and distance holds true.

In this section, the ferrite geometry is optimized as the first step of optimization of coils. Ferrite geometry's effect on coupling coefficient, coil losses and core losses are evaluated through FEM simulation. The accuracy of FEM results is verified by experimental test on one coil pair with different ferrite geometries. And the test could be easily repeated on other coil and ferrite shapes. For our

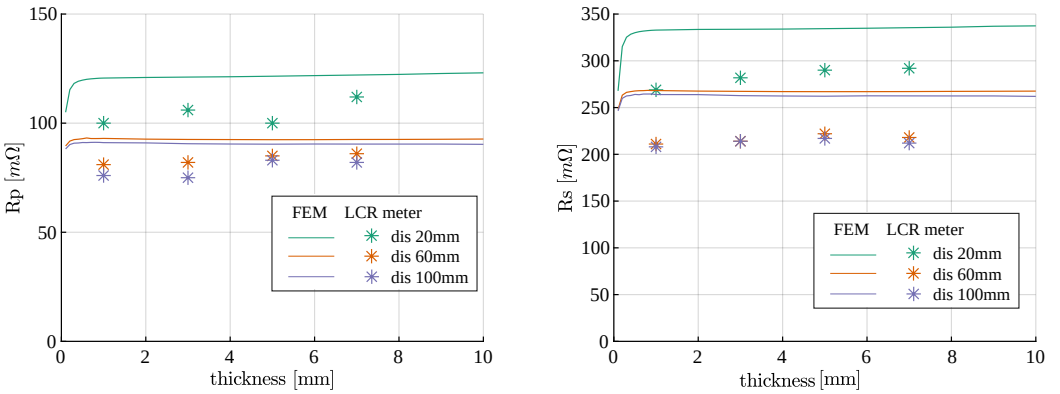

Fig. 5.19 FEM result and LCR test test result at 500 kHz (a) primary winding resistance (b) secondary winding resistance.

application, 5 mm thick round shape ferrite that covers the winding surface area is selected for the future discussion and modeling, due to its effect on high coupling and quality factors at large distance.

5.3 Models Based on ANN

An accurate electromagnetic model is complex especially for a loosely coupled system where a large air gap is present in the magnetic path, as shown in **Fig. 5.2**. Authors in [147] model the impedance of planar transformers with small air gaps on the magnetic path under Ampere's Law. In order to model the flux distribution around loosely coupled coils with large air gap, the method of current images is proposed to model the field distribution by replacing the magnetic substrate with another image current. However, this is under the assumption that the magnetic slab is semi-infinite [148]. Even though the effect of finite thickness of magnetic substrate on planar inductors is adapted [149][150], the magnetic substrate is still assumed to have infinite large surface area, as shown in **Fig. 5.20**(b). Work presented in [151] and [152] models the mutual inductance of loosely coupled coils based on the method of current images, however the ferrite plate needs to be twice as large as the outermost radius of winding to be able to neglect the non-uniform magnetic field around the edges of ferrite plate [153]. When the ferrite surface is as small as the winding surface, as shown in **Fig. 5.20**(c), with a large gap between primary and secondary winding, the crowded field around ferrite edges would cause error in the method of current images, and more flux is leaked to the backside of coils. Therefore the method of current images doesn't apply anymore. In addition, the method of current images couldn't differentiate ferrite surface shapes, for example rectangular shape or round shape. So far, finite-element method (FEM) simulation [154] or finite-element analysis with an integration over the entire system [155] are usually used to model the flux distribution as well as to predict coil characteristics such as inductance and resistance. Authors in [156] build the model by using FEM to obtain additional compensation coefficient to modify the method of current images. In [154], [157], FEM is directly used to simulate and evaluate the coil pair characteristics.

In the previous discussion on ferrite geometry in **Sec. 5.2**, the accuracy of results from FEM simulations are verified by impedance analyzers and through power test, and therefore FEM simulation results can

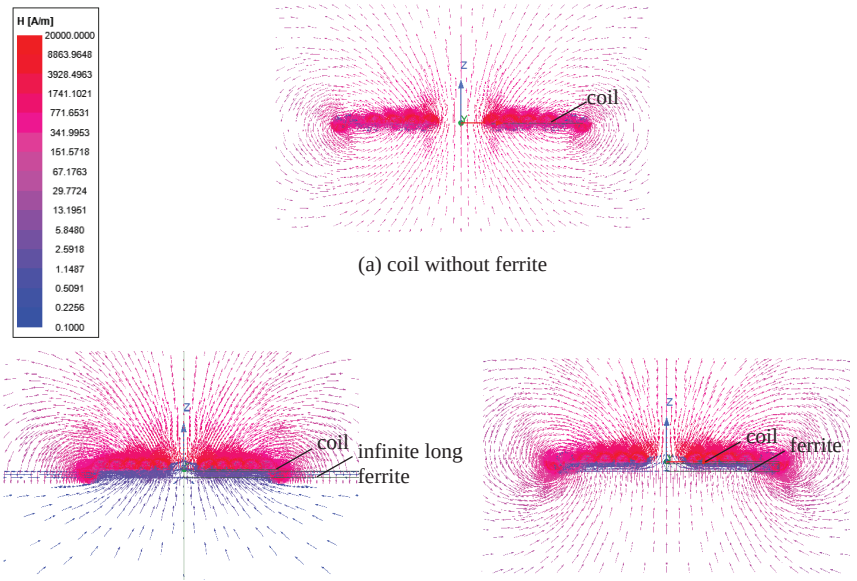

(a) coil without ferrite

(b) coil with infinite big ferrite plate

(c) coil with round ferrite plate

Fig. 5.20 Magnetic field around one planar PCB coil under 20 Arms 500 kHz excitation in three cases (a) PCB coil in the air without any ferrite around it (b) coil with an infinite long ferrite on the backside in contact with PCB coil (c) coil with an finite round shape ferrite plate place on the backside in contact with PCB coil.

be used to build up the coil model. FEM can be directly implemented into optimization flow to predict coil magnetic characteristics as discussed in [157]–[159], which typically means that FEM would be called in each optimization iteration step. When the design requirement changes, design optimization would need to rerun FEM simulation multiple times to generate new optimization designs. Since FEM simulation is the most time-costly stage in the design procedure, if the data-base from FEM simulation can be well saved for later-on optimization over coils, the model can be quickly called and time would be significantly saved for design optimization. Machine learning (ML) can take usage of this database from FEM, and effectively model nonlinear problems such as characteristics of IPT coils.

Supervised ML aims at designing a predictor (model) which predicts the values or categories from a finite set of labeled training data. In practice, given a set of training examples, ML learns a model that maps inputs x to a desired output y. And the performance of the model should be good on test data which are different to training data. The most popular implementation of supervised ML is ANN which imitates the biological brains and composed of neurons and excitations. The multi-layer perception structure of an ANN structure is shown in **Fig. 5.21** where the network of neurons are organized into layers. Neurons are densely connected between adjacent layers with weights w and bias b.

In power electronics, ANN has been used in control strategies [160], and in highly integrated systems related to multi-physics interaction [161], multi-parameter and multi-objective optimization [162]. Due to the lack of mathematical model of loosely coupled planar coils with ferrite on coil backside, ANN is deployed to learn from FEM dataset and generate models for future prediction of coil characteristics. Authors in [163] have optimized double D coils with data driven method by modeling the constant outputs ratios when there is coil misalignment with artificial neural network (ANN). With the ANN model, the design process can be accelerated significantly.

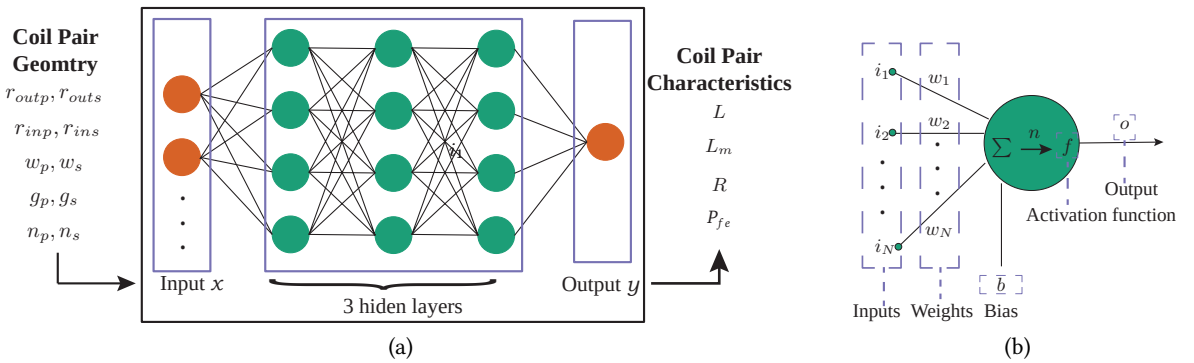

Fig. 5.21 (a) Multi-layer perception with five layers. Layer 1: input layer with multiple inputs. Layer 2-4: hidden layer with multiple neurons on each layer. Layer 5: Output layer one output. (b) Structure of the multi-input neuron.

Tab. 5.3 Design space of PCB coil geometries

Features	Characteristics	Value/Range	Units
Outer radius	r_{outp}, r_{outs}	< 90	mm
Inner radius	r_{inp}, r_{ins}	> 0	mm
Trace width	w_p, w_s	< 10	mm
gap-width ratio	gwr_p, gwr_s	< 1.5	mm

5.3.1 Model construction

Fully connected multilayer ANN is used to build the magnetic model to predict the characteristics of coil pairs. The input of ANN are coil geometries as shown in **Tab. 5.3**. The outputs of ANN are primary and secondary inductance L_p, L_s, mutual inductance L_m, primary and secondary resistance R_p, R_s and core loss $\hat{P}_{fe-p}$, $\hat{P}_{fe-s}$ under unity current.

In order to speed up the simulation process with a low computational cost, a rotational symmetry model is constructed in 2D FEM, as shown in **Fig. 5.22**. The simulation is solved with eddy current solver. A vacuum region is built 1000 times larger than the IPT coil pair and balloon boundary is used on the vacuum region. Current excitation is set on the cross-section surface of each turn. The initial mesh is generated automatically by Maxwell triangular adaptive uniform mesher. Tetrahedra elements are refined 30% per pass during adaptive analysis until the convergence criteria are satisfied. The adaptive process has 20 maximum number of passes, 1% energy error and at least two converged passes as the convergence criteria.

5.3.1.1 Pre-processing

1) Data collection: The training datasets cannot include every design variety, and carefully selecting training datasets can increase the accuracy of ANN model. In each 2D design, the number of turns and distance between two coils is fixed in each simulation. In the meantime, the other geometry parameters including turn width w, width-gap ratio gwr, coil outer radius r_{out} are swept in the design space to generate training datasets. The design of experiments are shown in **Fig. 5.23** following Central Composite Design and Latin Hypercube Sampling Design [164]. In total, in FEM simulation, three distance 20 mm, 40 mm and 60 mm are simulated, and under each distance, 6000 different coil

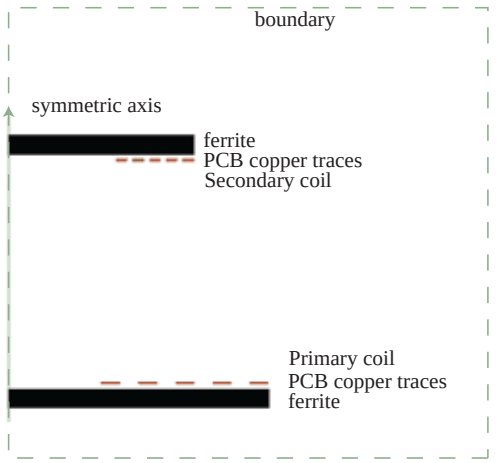

Fig. 5.22 The model in Ansys Maxwell 2D with rotational symmetrical axis.

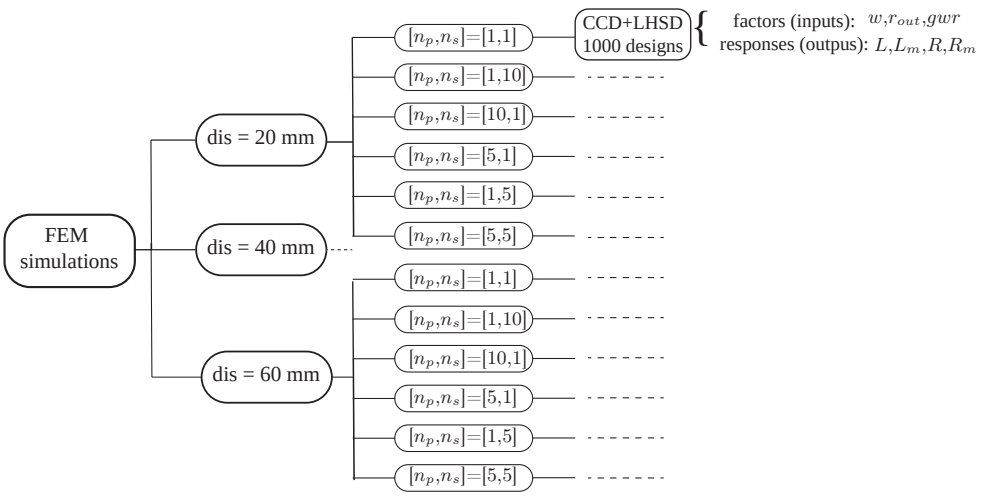

Fig. 5.23 Design of experiments. Coil pairs under three distances are simulated with MAXWELL 2D eddy current solver, and under each distance 6000 training datasets with different winding geometries are obtained.

pair geometries are simulated in FEM and from there 12000 single coil data are exported as training datasets to ANN.

2) Invalid values: The geometries which exceed the geometry ranges are considered as invalid values and are removed from training datasets. This operation reduces quantity of training data sets from 12000 to 7440.

3) Outliers: The outliers in the data is detected by applying the inter-quartile range rule, i.e. samples are considered as outliers outside of range $[Q_1 - 1.5IQR, Q_3 + 1.5IQR]$, where Q_1 is the first quartile and Q_3 is the third quartile through the list of all data. This operation reduces quantity of training data sets from 7440 to 5705.

5.3.1.2 Feature engineering

Ten geometries parameters are input features for each model. Ten geometries are not fully independent from each other, for example with r_{out-p}, w_p, gwr_p and n_p, the inner radius r_{in-p} is determined. However, ten inputs features instead of eight independent features are used, in order to improve the abundance of features and so to increase the ANN model accuracy. In addition, as the different features are on different scales, data for each feature is normalized into range [-1, 1], which helps the models converge faster for a given learning rate.

5.3.1.3 Model implementation and hyper parameter tuning

A multilayer fully connected feed forward neural network as shown in **Fig. 5.21** is chosen to estimate the coil characteristics. The chosen structure is composed of one input layer, three hidden layers and one output layer. On each neuron, the inputs of the neuron is processed as the weighted summation of outputs from neurons in the previous layer:

$$n = \sum_{j=1}^{K} w_j i_j + b \tag{5.3}$$

Then the input n passes through the activation function to generate the neuron output o, the activation function used in this work is tangent sigmoid transfer function which is defined as:

$$f(n) = \frac{2}{1 + e^{-2n}} - 1 \tag{5.4}$$

The back propagation algorithm first propagates the input forward through the network to obtain the estimation at output. With the loss function and chain rule, the gradient of each layer is calculated backward through the network from the last layer to the first layer. Finally the weights and biases are updated with gradient descent optimization rule. The mean square error between the targets and the estimation is used as the loss function (performance function) $F_{loss} = \frac{1}{N}\sum_{j=1}^{N}(T_j - O_j)^2$, which is to be minimized by adjusting the network parameters including weights w and bias b.

While calculating the gradient descent vector, instead of the steepest descent algorithm, Levenberg-Marquardt is used for the update of parameters $\mathbf{x}$:

$$\mathbf{x_{k+1}} = \mathbf{x_k} - [\mathbf{J^T}(\mathbf{x_k})\mathbf{J}(\mathbf{x_k}) + \mu\mathbf{I}]^{-1}\mathbf{J^T}(\mathbf{x_k})\mathbf{e}(\mathbf{x}) \tag{5.5}$$

where $\mathbf{x_{k+1}}$ is a vector composed of the weights and bias parameters after $k+1$ iteration, $\mathbf{x_k}$ is from last iteration. $\mathbf{J}$ is the Jacobian matrix, $\mathbf{I}$ is identity matrix. $\mathbf{e}$ is the error vector obtained by transferring the loss function into the form of sums of squares of nonlinear functions $F_{loss}(\mathbf{x}) = \mathbf{e^T}(\mathbf{x})\mathbf{e}(\mathbf{x})$. μ is the learning rate which is updated in each iteration.

The hyper parameters are tuned by hand, and in the end we set: initial learning rate μ_0 to be 0.001; the decrease ratio of learning rate to be 0.1; the increase ratio of learning rate to be 10; maximum iterations to be 1000; training stops if the validation performance degrades for 6 consecutive iterations. In summary, the ANNs are trained with the parameters in **Tab. 5.4**.

5.3.2 Model verification

One thousand datasets are generated as test datasets with optimal space-filling design under each distance. Once the model is trained, the test datasets are fed into the trained models' input and the

Tab. 5.4 Specifications of ANN training algorithm

Training Fcn	Levenberg-Marquardt back-propagation
Performance Fcn	Mean squared error
Output dimensions	1
Input dimensions	10, $[r_{out-p}, r_{in-p}, width_p, gap_p, n_p, r_{out-s}, r_{in-s}, width_s, gap_s, n_s]$
hidden layer size	[20, 20, 20]
Train ratio	70
Validation ratio	30

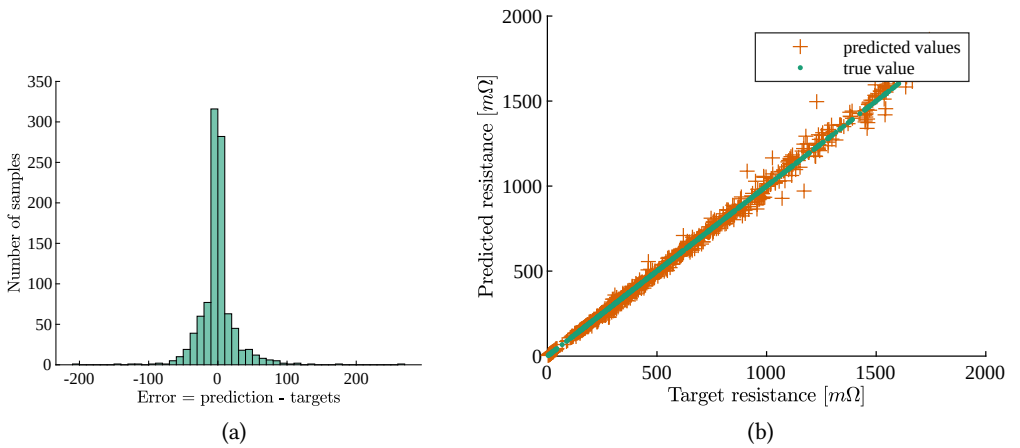

Fig. 5.24 Performance of ANN model of resistance R at 60 mm distance on test dataset. (a) Error histogram (b) Regression curve between the predicted response and targets.

predicted responses are obtained from the models. In order to get a better performance model, the network is trained 5 times with the same training data, and the one with the lowest error compared to the test data is used as the final model. The model's effectiveness is first validated: taking the model for AC resistance R at distance of 60 mm as an example, the performance is shown in **Fig. 5.24**. In **Fig. 5.24a** the error between target values and predicted values $Error = Prediction - targets$ is centered around zero and symmetrical, which means the prediction model brings almost no bias. **Fig. 5.24b** shows a linear fit line, where we can observe that the predicted values lie around the regression line with the regression values of 0.98.

The model's accuracy is also evaluated: mean percentage error is calculated for each model and results are shown in **Tab. 5.5**. It can be seen that the error is between 7% and 15%. Considering that in our application where the nominal inductance value is below 5 µH and the resistance is below 0.5 Ω, in the manufacturing and installation process, this error can be mitigated by controlling the parasitic inductance and resistance in the IPT system, therefore this design error is acceptable.

In addition to further verify the model accuracy, the coil pair with geometries shown in **Tab. 5.1** is tested with LCR meter, and the test results and predictions from the model are shown in **Tab. 5.6**. The error with test is within 15%. The generation of ANN model is summarized in **Fig. 5.25**, this model is later implemented into optimization tool in **Chap. 7**.

Tab. 5.5 Error on the test data

Error	L	L_m	R	$P_{loss-fe}$
20 mm	12.6%	7.3%	7.4 %	7.3%
40 mm	13.5%	13.5%	14.6%	13.6%
60 mm	13.6%	14.8%	13.5%	11.7%

Tab. 5.6 Comparison of test and modeling result of one coil pair prototype

		L_p	L_s	L_m	R_p	R_s
60 mm	test results	1.9 µH	4.9 µH	0.62 µH	80 mΩ	220 mΩ
	model results	2.0 µH	5.2 µH	0.7 µH	83 mΩ	241 mΩ
	error	5.3%	6.1%	12.9%	3.7%	9.5%
40 mm	test results	1.9 µH	5.1 µH	1.15 µH	85 mΩ	245 mΩ
	model results	2.1 µH	5.4 µH	1.26 µH	86 mΩ	270 mΩ
	error	10.5%	5.8%	9.6%	1.2%	10.2%
20 mm	test results	2.3 µH	6 µH	2.42 µH	100 mΩ	295 mΩ
	model results	2.4 µH	6.3 µH	2.59 µH	112 mΩ	285 mΩ
	error	4%	5%	7%	12%	5.6%

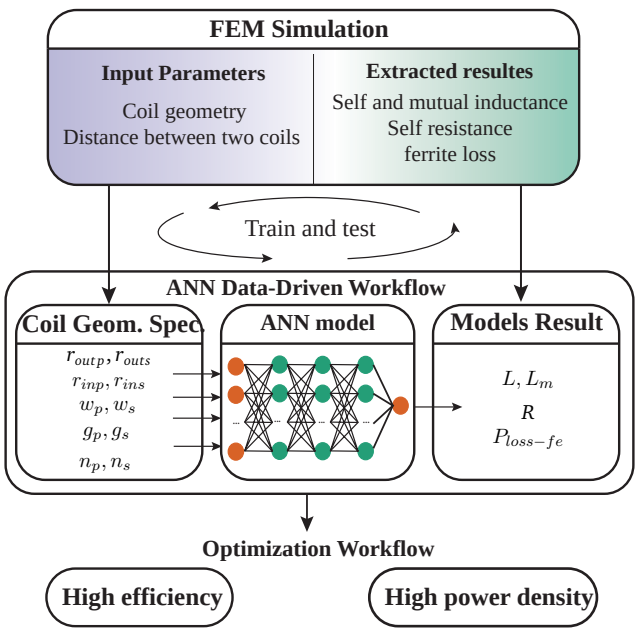

Fig. 5.25 Design flow: FEM generate data base; ANN trains the parameter models with labeled data base from FEM; Genetic Algorithm generate optimal designs based on ANN models.

5.4 Summary

This chapter focuses on the examination of the ferrite effect on coil pairs. It begins with a comprehensive analysis of different coil geometries, involving surface shapes and thickness. The findings demonstrate that round and rectangular-shaped ferrite, with a thickness exceeding 1 mm, exhibit superior performance in terms of coupling and quality factors.

Subsequently, a magnetic model is proposed, on the coil pairs with round-shaped ferrite with a 5 mm thickness. This model predicts key coil link characteristics, including coil inductance, winding resistance, and core losses, for coil pairs with arbitrary winding geometries. The development of this magnetic model is based on ANN together with FEM data, with thorough pre-verification of the FEM data's accuracy. Initial verification of the model's accuracy is accomplished using data obtained from FEM simulations and with the test result of one coil prototype.

The proposed magnetic model can be easily integrated into the optimization tool and can realize fast computation of arbitrary winding geometry without using FEM. When the optimization specification changes, the inductances of new optimal designs can be explored rapidly without extra simulation effort. However, the resistance model of winding geometry is developed for fixed operation frequency at 500 kHz. When the frequency changes from the frequency in this manuscript, the magnetic model needs to be extended to predict the coil winding resistance at other frequencies. This extension can be realized by enlarging the FEM data-base at other frequencies.

6
Thermal Model of the Coil

This chapter analyzes the heat dissipation paths in a coil system, based on which a thermal model is proposed to predict the steady state temperature rise in different parts in a coil system. Because of the symmetrical characteristic of the coil, the model involves radial and axial direction dissipation path. The model achieves accurate prediction by updating the convection coefficient and radiation resistance in iterations. In addition, the model's generality and accuracy are verified with test on coils with different geometries. The proposed model doesn't require running simulations, making it quick to execute and easy to implement into optimization tool.

6.1 Thermal Modeling

In a coil with PCB windings, there are five layers of different materials: coating of PCB, PCB copper, PCB substrate, ferrite and the enclosure. Power loss of 3F36 ferrite material increases significantly when temperature is over 100 °C. In the PCB, the glass transition temperature of FR4 layer is around 150 °C, and the maximum operating temperature of the coating material is around 125 °C. An accurate thermal model is necessary to predict the temperature rise in these critical points in coil systems to make sure the coil function normally.

6.1.1 Thermal network

In a coil system, heat is transferred in three different mechanisms: conduction, convection, and radiation. Inside each layer, the heat is transferred in the radial direction as shown in **Fig. 6.1**. Between adjacent layers, the heat is transferred in axial direction. On the surface of coil system, the heat exchange with air is through convection and radiation. While building the thermal network for a coil system, the coil system is modeled as axially symmetrical structure and the modeling is only done on half plane of the cross section, as shown in **Fig. 6.2**.

The coil is modeled as a thermal resistance network, with the ambient temperature as the boundary condition. To predict the temperature in the planar coil, the first step is to define the thermal network, with which temperature matrix for the coil system can be predicted as:

$$[T] = [T_{amb}] + [P][Z] \tag{6.1}$$

where, Z is the thermal admittance matrix and is based on the coil geometry and material characteristics.

In order to obtain the thermal admittance matrix, the first step is to clarify the nodes distribution inside a coil system. As shown in **Fig. 6.2**, in each layer of the system, there are a row of nodes. And

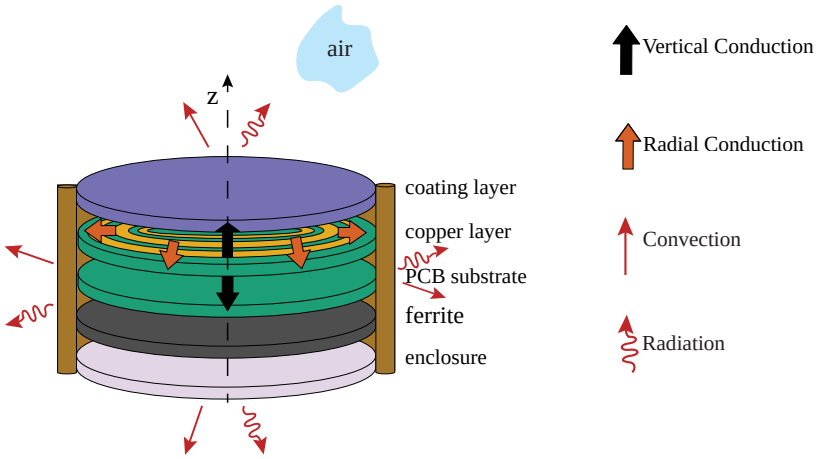

Fig. 6.1 Thermal flux dissipation paths in one coil.

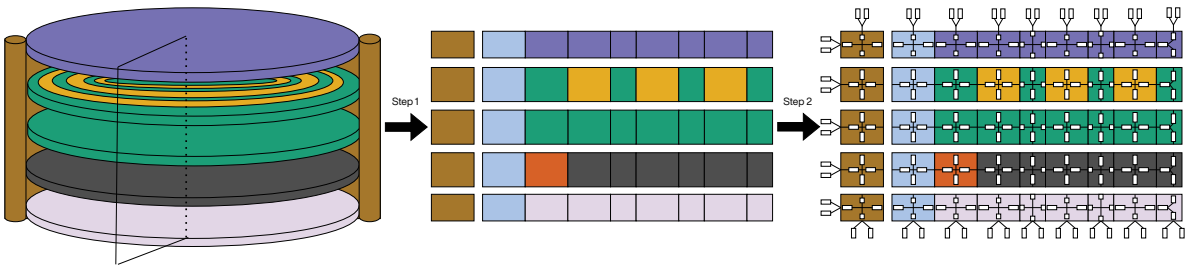

Fig. 6.2 Construction of the thermal network. Form left to right: original coil structure, nodes defined by layers and turns in a coil system, thermal resistance connected to nodes.

in each row of nodes, the number of nodes depends on the number of turns of coils. At each node, four resistances are connected to it from radial and axial directions. The nodes are linked together by their conduction resistance. Moreover, convection and radiation resistances are attached to the surfaces of the coil. Thermal resistances at each node need to be calculated based on the local geometry and local material.

6.1.1.1 Conduction resistance

Inside the coils, the thermal resistances are defined by conduction effect. The heat transfers in either axial or radial direction through either planar walls or radial walls:

1. The heat pass in the axial direction from the copper and ferrite through coating, PCB board, and back layers through planar walls.
2. The heat spread in the radial direction from the hot spots through the objects to the enclosure through radial walls.

Following the two directions, at each node, four conductive resistances are built, numbered from R1 to R4 as shown in **Fig. 6.3**. The resistances are characterized by the local geometry, including: r_1: Inner radius from the center of the device to the rectangle; r_2: Outer radius from the center of the device to the rectangle; H: Height of the rectangle that corresponds to the thickness of a device layer; L: Length of the rectangle. It is computed as $L = r_2 - r_1$. R1 and R3 are radial conductive resistances

Tab. 6.1 Thermal conductivity of different materials involved in a coil system.

Material	k (thermal conductivity) [W/mK]
Coating material	0.2 [165]
Copper (PCB winding)	401 [165]
FR4 (PCB substrate)	0.25 [166]
MnZn Ferrite	5 [167]
ABS/ASA plastic (enclosure)	0.14 [168]
Aluminum (back-plane)	237 [165]

and R2 and R4 are planar conductive resistances. The calculation of resistance follows the instructions presented in **Sec. A.1**.

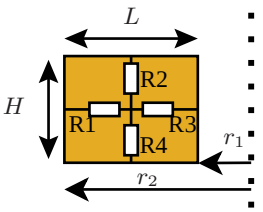

Fig. 6.3 Four resistances are constructed at each internal node.

$$R1_{th,cond} = \frac{ln(r_2/(r_1 + L/2))}{2\pi Hk} \tag{6.2}$$

$$R3_{th,cond} = \frac{ln((r_1 + L/2)/r_1)}{2\pi Hk} \tag{6.3}$$

$$R2_{th,cond} = R4_{th,cond} = \frac{H/2}{k\pi \cdot (r_2^2 - r_1^2)} \tag{6.4}$$

It can be seen from the equations above that the conduction resistance depends only on the geometry and thermal conductivity of each material, and it is independent from temperature change. The summary of the thermal conductivity k of materials involved in our coil system is shown in **Tab. 6.1**.

6.1.1.2 Convection

Natural air cooling is used in the proposed IPT system. The convection thermal resistances are placed on the exposing surfaces of the coil and in parallel with radiation thermal resistances as shown in **Fig. 6.2**.

The convection resistances are different when the hot surfaces are facing different directions, which is analyzed in details in **Sec. A.2**. Distinction is made while building convection resistance between the upper surface of the device, the lower surface and the side surface.

The calculation of convection resistance follows **Sec. A.2**. When the coil is horizontally placed, as shown in **Fig. 6.4**, regarding the upper surface, the Nusselt number in case of a "Top surface of hot plate" is used. Convection coefficient h is then determined and thermal resistance is

$$R_{th,conv} = \frac{1}{A_{up}h_{up}} = \frac{1}{h_{up} \cdot \pi(r_2^2 - r_1^2)} \tag{6.5}$$

where $\pi(r_2^2 - r_1^2)$ is the local surface area.

For the lower surface, correlations of Nusselt number in case of a "Bottom surface of hot plate " are

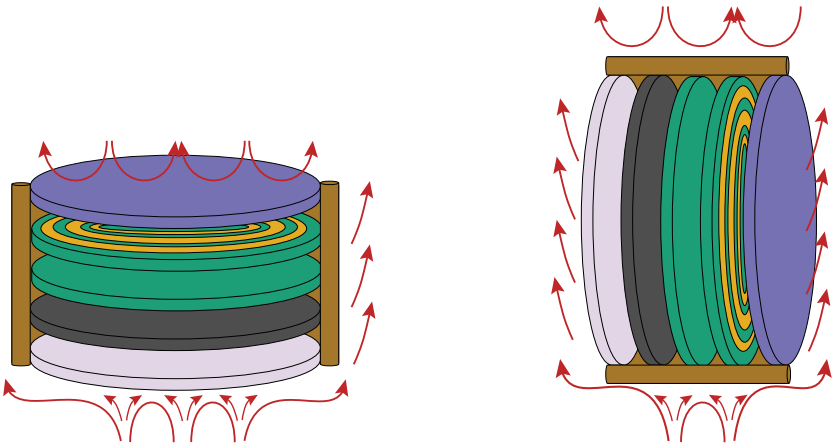

(a) (b)

Fig. 6.4 (a) Convection on the coil surface when the coil is placed horizontally in air. (b) Convection on the coil surface when the coil is placed vertically in air.

used. Convection coefficient h is then determined and thermal resistance is

$$R_{th,conv} = \frac{1}{A_{low} h_{low}} = \frac{1}{h_{low} \cdot \pi(r_2^2 - r_1^2)} \tag{6.6}$$

where $\pi(r_2^2 - r_1^2)$ is the local surface area.

For the side surface, the convection thermal resistance is

$$R_{th,conv} = \frac{1}{A_{side} h_{side}} = \frac{1}{h_{side} \cdot 2\pi r_2 \cdot H} \tag{6.7}$$

where $2\pi r_2 \cdot H$ is the local surface area. When the coil is vertically placed, as shown in **Fig. 6.4b**, the geometry parameters in (6.5)-(6.7) stay the same, and only the convection coefficient h changes.

The convection resistances depend on convection coefficient, and convection coefficient depends on the local temperature, as discussed in **Sec. A.2**. In reverse, the change of convection resistance leads to the change in temperatures. Therefore convection resistance and temperatures are coupled, and during modeling, both should be updated through iterations until convergence.

6.1.1.3 Radiation

For natural cooling conditions, the radiation effect could be as significant as the convection effect. In **Fig. 6.5**, the heat flux transferred from per unit area of the surface through convection and radiation is shown. The room temperature is set at 293.15 K. The surface temperature range is from 293.15 K to 373.15 K. The emissivity is selected as 1, since the plastic enclosure have emissivity close to 1 [169]. Considering that under natural cooling with air, the convection coefficient is usually under 30. The convection coefficient from 1 to 30 is plotted in comparison to radiation effect. As can be seen from **Fig. 6.5**, radiation effect is almost nearly as significant as convection effect when the convection coefficient is 10. Therefore the radiation effect could not be ignored in this temperature range.

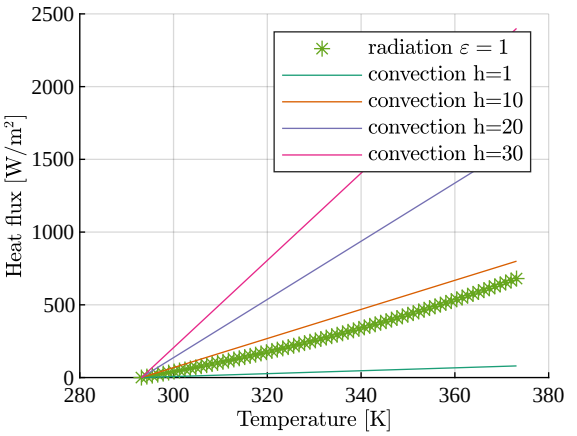

Fig. 6.5 Heat flux transferred from per unit area through convection and radiation under different surface temperature from 293.15 K to 373.15 K. Room temperature is 293.15 K.

Tab. 6.2 Emissivity of different surface materials in a coil system.

Material	coating material	unoxidized polished aluminium	ABS/ASA plastic (enclosure)
ε (emissivity)	0.9 [169]	0.05 [170]	0.92 [169]

The radiation thermal resistance is found on the surfaces of the coil, in parallel with convection resistance.

$$R_{th,rad} = \frac{T_s - T_{amb}}{(T_s^4 - T_{amb}^4)\varepsilon\alpha A} \tag{6.8}$$

where A is the same local surface area as the ones for the convection thermal resistance calculation. σ is the Stefan-Boltzmann constant, ε is the emissivity coefficient of the surface which indicates the radiation of heat from an object according to Stefan-Boltzmann Law. In the thermal modeling of coils, each surface exposing to air is considered separately as shown in **Fig. 6.6**. The surface emissivity coefficient is taken as constant and is taken at 40 °C. The emissivity coefficients of different surface materials in a coil system is shown in **Tab. 6.2**.

It can be seen from (6.8) that the radiation resistance is coupled with the surface temperature T_s, therefore during modeling process, the radiation resistance needs to be updated iteratively with surface temperature until convergence.

6.1.2 Modeling process

The heat transmission rate on the surface and the temperature on surfaces are cross dependent parameters. Convection and radiation rates through surfaces are dependent on the local surface temperature, and in reverse, the temperature on the surface is changing with convection and radiation rates. In the modeling, the temperature is calculated in iterations until the temperatures on surfaces converge as shown in **Fig. 6.7**. The initial temperature on the coil surfaces is set to T_{amb} + 20°. The convection coefficient and radiation resistance are calculated under this temperature. Through the thermal resistance network and with the knowledge of power loss in copper and ferrite, the temperature at each node of the coil system is calculated. The updated surface temperature is then

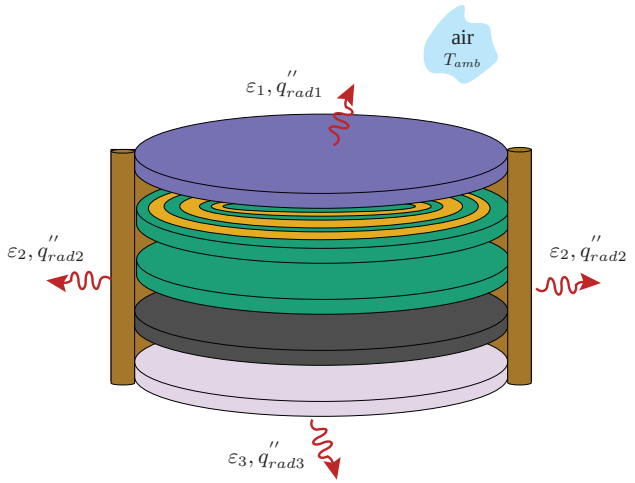

Fig. 6.6 Radiation on the coil surfaces dependent on the emissivity of material, surface and room temperature.

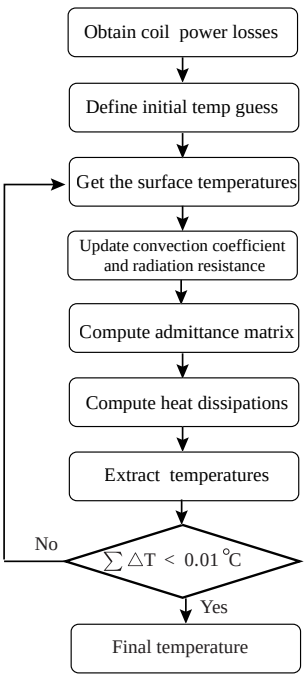

Fig. 6.7 Calculation flow to predict the temperature at stable state.

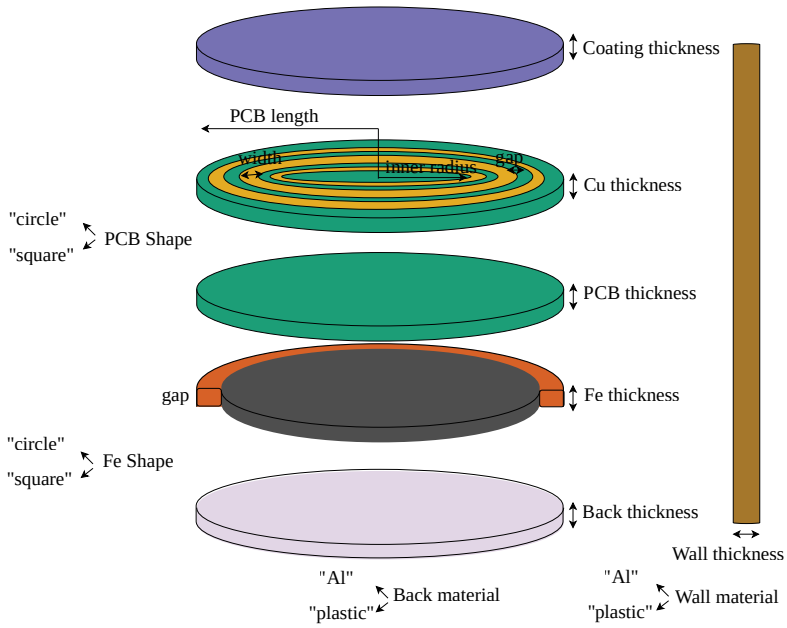

Fig. 6.8 Free input geometric coil parameters in the calculation flow.

used to calculate the new heat dissipation coefficients. The iteration continues until the convergence happens in five consecutive cycles. The convergence criterion is that the difference between predicted average temperature on the surface and the prediction temperature from last iteration is less than 0.01 °C. The modeling can be scaled to different component materials and geometries. All the free geometric parameters in the model are shown in **Fig. 6.8**.

6.2 Experimental Verification

The thermal models have taken into consideration several variables: coil positions, coil geometries and ambient temperature, etc. This section will verify the accuracy and generality of the thermal models with several tests. The thermal model is verified with one coil with geometries listed in **Tab. 6.3**. Four type k thermocouples are used to measure temperatures. One thermocouple is inserted between the PCB layer and ferrite layer, and one is inserted between ferrite layer and enclosure. Another two thermocouples are on the the top surface of PCB and on the bottom of enclosure respectively.

The coil is tested under room temperature 21 °C in both vertical and horizontal positions. The coil is connected to a high frequency current source at 500 kHz, 4 A rms, as shown in **Fig. 6.9**. The loss in the PCB winding and in the core is simulated with FEM simulation and found to be 3.61 W and 0.7 mW. The copper loss is distributed according to turns length ratio. The temperature on the third turn of PCB traces are measured with thermocouples. It takes around 1.5 hours for the coil temperature to stabilize. In the simulation, it takes 10 and 11 iterations respectively for the surface temperatures to converge in the horizontal and vertical cases. The final convection coefficient of the PCB surface is 7.3 for the horizontal case and 6.9 for the vertical case.

From **Fig. 6.10**, it can be noted that the temperature for vertical and horizontal placed coils are slightly different: the bottom temperature is slightly higher when the coil is horizontally placed, which can be explained by the low convection coefficient on the bottom surface. The highest temperature is on the copper trace which is due to the fact that major power loss is from copper. The heat is conducted from copper layer to PCB substrate, and to ferrite, to enclosure. Therefore the temperature decreases from copper to the enclosure back and side walls. In addition, the predicted temperatures at four locations are close to the measured surface temperatures and the biggest prediction error for this coil is 3 °C.

Another two coils with different geometries are tested in vertical position to verify the geometry generality of the modeling method. The coil geometries are listed in **Tab. 6.4**. Coil 1 is tested with room temperature at 21 °C. The coil is connected to 20 A DC source which generates 8.64 W losses in copper traces. Coil 2 is tested with ambient temperature at 21 °C and 45 °C respectively. Coil 2 is connected to 10 A DC source which causes 13.8 W on copper traces. The temperatures on the innerest turn on top and bottom surface of coil are measured and shown in **Fig. 6.11**.

Tab. 6.3 The coil geometry under thermal test.

	Characteristics	Coil
PCB parameters	PCB edge length [mm]	120
	winding inner radius [mm]	33.5
	number of turns	5
	width of each turn [mm]	2.7
	gap between turns	1.73
Ferrite	shape	round
	thickness [mm]	5.08
PCB coating	thickness [mm]	≈ 0
Backplane	material	Plastic
	thickness [mm]	2

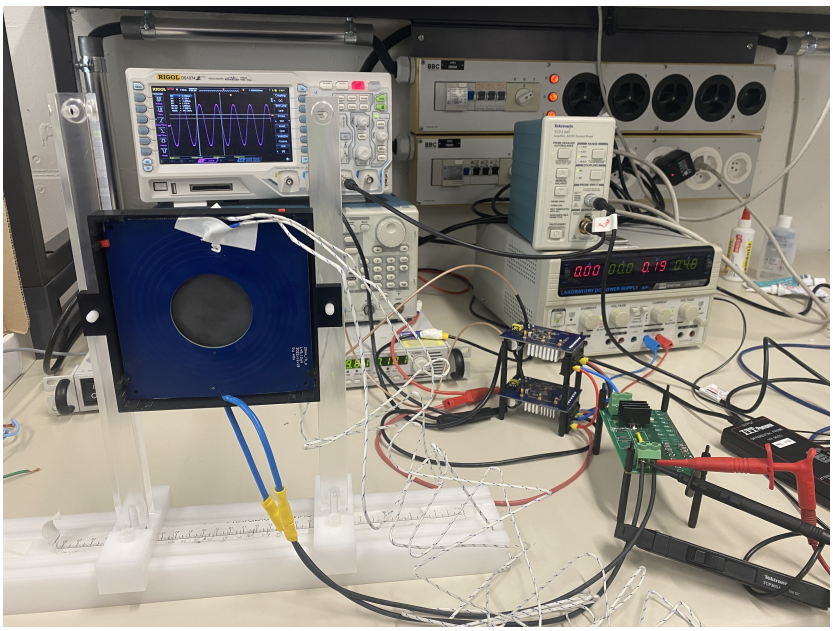

Fig. 6.9 The coil under test connected with high frequency current source.

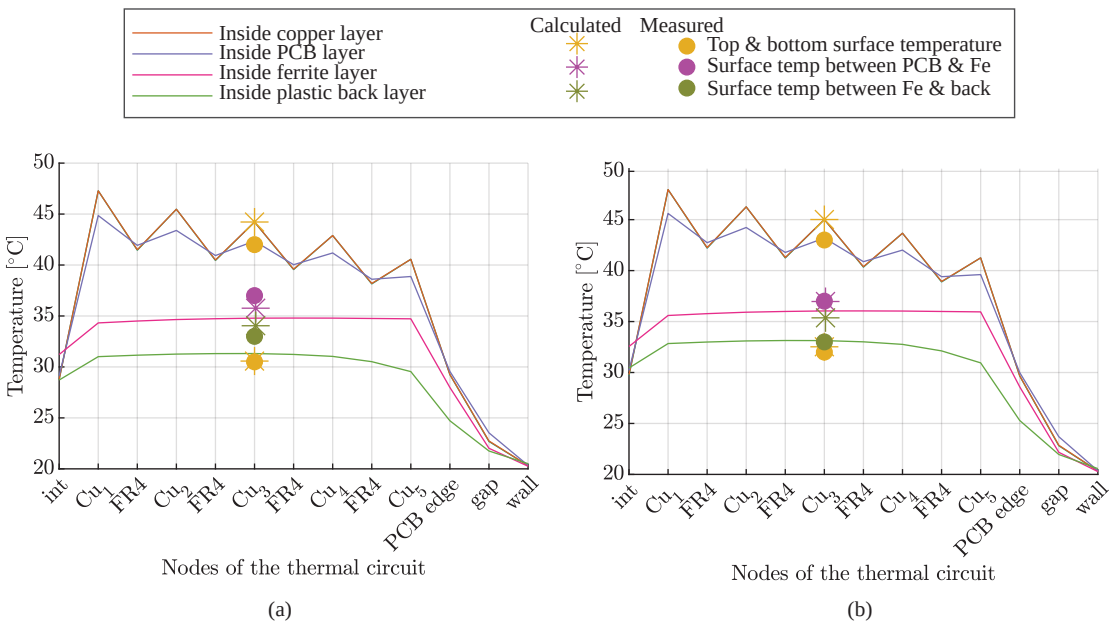

Fig. 6.10 Measured and calculated temperature in different layers of the coil (a) the coil is vertically placed (b) the coil is horizontally placed. Stars '*' are the calculated top and bottom surface temperature. Dots '·' are the measured surface temperature. Lines '-' are the calculated temperature at each node inside each layer.

The measurement and prediction temperatures of coil 1 are shown in **Fig. 6.11a**. The hottest temperature appears on the innerest turn on copper, which reaches 50 °C. This low temperature rise is due to the large surface area of coil 1. The temperatures of coil 2 are shown in **Fig. 6.11b** and **Fig. 6.11c**. This coil doesn't have enclosure, and the temperatures on bottom surface of ferrite and on top surface of PCB are tested. The maximum temperature rise at room temperature and at 45 °C

Tab. 6.4 Three tested coil geometries.

	Characteristics	Coil 1	Coil 2
PCB parameters	PCB edge length [mm]	170	120
	winding inner radius [mm]	40	33.5
	number of turns	3	5
	width of each turn [mm]	10.5	2.7
	gap between turns	0.9	1.73
Ferrite	shape	rectangular	round
	thickness [mm]	5	5
PCB coating	thickness [mm]	≈ 0	≈ 0
Backplane	material	Plastic	Plastic
	thickness [mm]	2	0

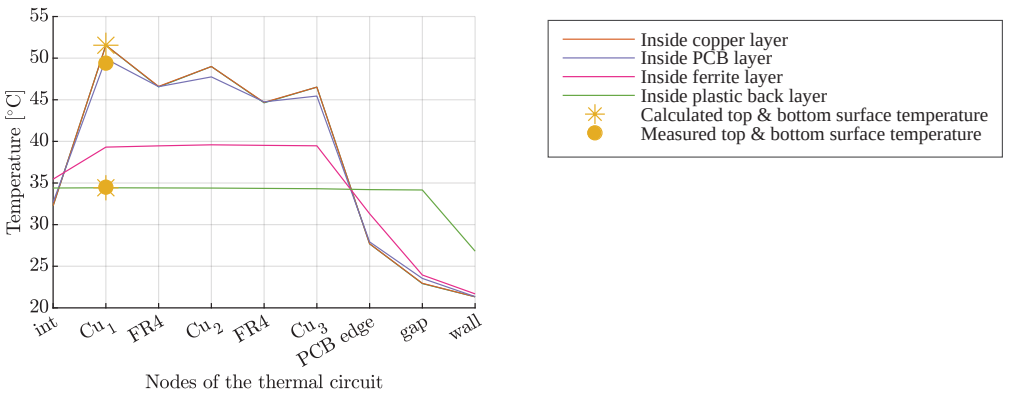

(a)

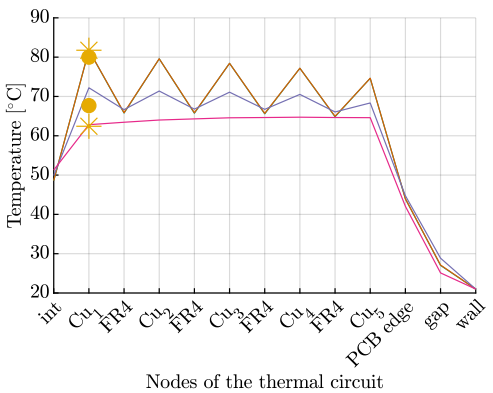

(b)

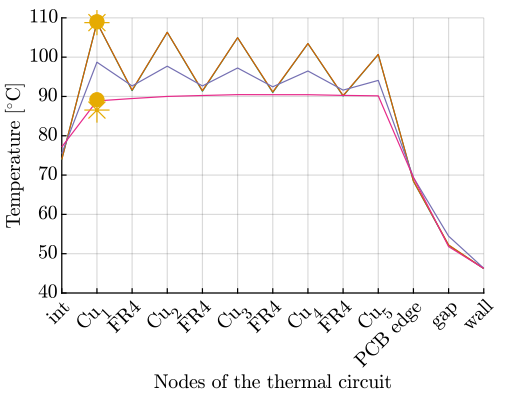

(c)

Fig. 6.11 Measured and calculated temperature in different layers of the (a) coil 1 under21 °C ambient temperature. (b) coil 2 under 21 °C ambient temperature. (c) coil 2 under 45 °C ambient temperature.

ambient temperature are 60 °C and 64 °C respectively. In addition, it can be seen that the temperature distribution inside coil is similar under different ambient temperature. These tests with different coil geometries verify the accuracy and generality of the thermal model.

6.3 Summary

The temperature of individual components within a coil plays a critical role in determining its overall performance. This chapter proposes a thermal model that can predict the steady state temperature at each node in a coil system based on planar PCBs. The objectives of this thermal model are to achieve high accuracy, low computation time, and easy integration into the optimization flow.

The proposed model considers conduction, convection, and radiation effects based on the analysis of dissipation methods in a coil system. The model takes into account the axial symmetrical geometry of the coil and constructs a thermal network in axial and radial directions. In addition, due to the coupling between the surface temperature and the convection and radiation resistances, the convection and radiation resistances are updated at each iteration while predicting the temperature until convergence is reached, resulting in higher accuracy. Furthermore, no measurements or computational fluid dynamics (CFD) simulations are involved in the model, which results in fast computation. In addition, the fully analytic model permits easy integration into optimization process.

The thermal model is designed to be adaptable to various geometry changes. Once the PCB geometry is provided, the thermal network can be rapidly and simply generated. Additionally, the model is validated under a broad range of operating conditions, including various coil configurations, DC and AC excitation, and different ambient temperatures. The thermal model will be integrated to the optimization tool to ensure that the coil designs meet the thermal coordination.

7
Optimization Flow

In this chapter, the optimization procedure of a coil link is proposed, which integrates the electrical model, the magnetic model and the thermal model. The optimization is based on GA and is proposed for the coils with ferrite on their backside. The high efficiency of coil link and the small coil size are the optimization goals, and the output voltage as well as thermal limitations are the optimization constraints. One optimal coil pair from the Pareto front is prototyped and tested under different load conditions. In addition, the loss decomposition at nominal load is analyzed as indication for further efficiency optimization.

7.1 Optimization with Genetic Algorithm

GA is widely used in different scenarios to solve multi-objective optimization problems by mimicking biological evolution with natural selection process such as mutation, crossover and selection. In power electronics field, GA has been used in circuit design optimization [171][172], printed circuit board optimization [173] as well as components design in converter modules such as transformers or heatsinks [174][175] where the multi-parameter and multi-objective optimization is usually required. In this chapter, GA is used to generate optimal geometry design of PCB based IPT coil pairs in the constraints of system specifications. As shown in **Fig. 7.1**, each generation is selected to approach a better objective, and the mutation and crossover operation is performed within the defined constraints. Considering the application of IPT coils as APS in MV applications, high efficiency and high power density are selected as two optimization objectives. Meanwhile, the output voltage and thermal limits are applied as constraints during optimization.

The IPT system with electrical specifications listed in **Tab. 7.1** is used as the demonstration example of the optimization result. Based on the discussion in **Sec. 4.5.1**, the design space is defined and is shown in **Tab. 7.2**. The winding geometries are optimally designed with GA algorithm, incorporating models that are independently proposed before: the electric circuit model in **Chap. 3**, the magnetic model proposed in **Chap. 5**, and the thermal model proposed in **Chap. 6**. Those models are integrated into optimization flow and are called during each optimization iteration.

Tab. 7.1 System nominal operation specifications

V_{in}	V_{out}	P_{out}	f_{sw}
80 V	$36 \pm 2V$	130 W	500 kHz

7.1.1 Objectives: high efficiency and high power density

In order to better reflect the resistance of spiral winding, the resistance from ANN model is modified with a length ratio

$$R = R_{ANN} * \frac{spiral\ length}{concentric\ cirles\ length} \tag{7.1}$$

where *spiral length* is the length of the circular spiral, and *concentric cirles length* is the length of concentric circles in 2D FEM simulations. This modified resistance is used in the calculation of efficiency.

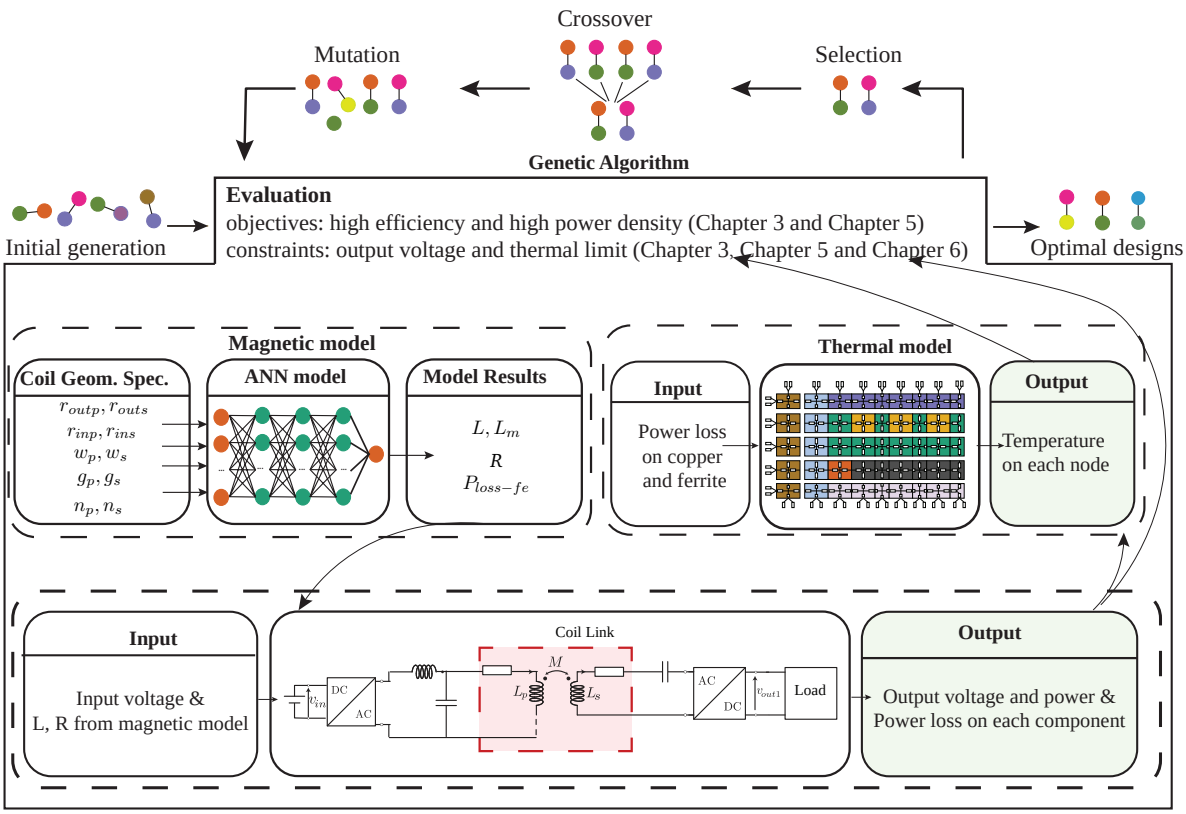

Fig. 7.1 GA optimization process with initial generation and the repetitive evaluation, selection, crossover and mutation operators. The magnetic model, electric circuit model and thermal model are called in the evaluation stage.

Tab. 7.2 Design space of PCB coil geometries and operating frequency

Sweeping inputs	Characteristics	Value/Range	Units
Outer radius	r_{outp}, r_{outs}	20-80	mm
Copper trace width	w_p, w_s	1-10	mm
gap-width ratio	gwr_p, gwr_s	0.1-1.5	mm
Number of turns	n_p, n_s	1-10	-
Distance between coils	dis	60	mm

The AC-AC efficiency of a coil link is

$$\eta = \frac{P_{out}}{P_{out} + P_{loss}} \tag{7.2}$$

where $P_{loss} = P_w + P_{fe}$. P_w is the winding loss on both primary and secondary side and P_{fe} is the ferrite loss on both sides. The output power and power losses on the winding are calculated as discussed in **Chap. 3**.

Loss of ferrite at nominal current is scaled from the ferrite loss result from magnetic model (at 1 Arms) from **Chap. 5**

$$P_{fe} = \hat{P}_{fe-p-1A} I_p^y + \hat{P}_{fe-s-1A} I_s^y \tag{7.3}$$

where $y = 2.7$ for 3F36 MnZn material.

In addition to power transfer efficiency, the small coil size, which relates to high power density under the same output power, is another optimization objective, and it's defined by outer radius of the coil pair: $max(r_{out-p}, r_{out-s})$. The coil designs that have high efficiency and small size are selected as *parents* of the current population, and contribute their *genes* (features) to the *children*. The detailed explanation of the function to select parents and create the next generation can be found in [176].

7.1.2 Constraints: thermal limit and output voltage limit

The optimization is done with two constraints: output voltage range and thermal limits. Qualified output range is 36 V ± 2 V. In the optimization flow, the output voltage of each design is evaluated as discussed in **Chap. 3** and the designs outside of this range are invalid. The thermal limit is defined for both primary and secondary coil. The losses on the coils are needed to predict the temperature rise. The power losses of windings are

$$\begin{aligned} P_{w-p} &= R_p I_p^2 \\ P_{w-s} &= R_s I_s^2 \end{aligned} \tag{7.4}$$

where R_p and R_s are the resistance of primary and secondary windings under 500 kHz and are obtained from magnetic model in **Chap. 5**.

The power losses in the ferrite are

$$\begin{aligned} P_{fe-p} &= \hat{P}_{fe-p} I_p^y \\ P_{fe-s} &= \hat{P}_{fe-s} I_s^y \end{aligned} \tag{7.5}$$

where $\hat{P}_{fe-p}$ and $\hat{P}_{fe-s}$ are primary and secondary core loss under 1 Arms current obtained from the magnetic model.

The winding loss calculated from (7.4) and core loss calculated from (7.5) are fed into the thermal model proposed in **Chap. 6**. The loss is distributed in each turn according to turns length ratio. With losses as input, the maximum temperature rise in the coil system can be calculated. The thermal constraint is that the average temperature rise in each layer inside coil $\Delta T < 80^\circ$ C, considering that the 3F36 material has low loss in the temperature range $20^\circ C - 100^\circ C$, and maximum working temperature of PCB coating material is around $125^\circ C$.

7.1.3 Initial generation

The initial population of GA is important to its computation efficiency. If letting the initial population be entirely random, the optimization would not only be less efficient but may also end up at no feasible solutions. In order to avoid this situation, a fast brute force searching with big steps is used to provide the first population.

The coil pairs with geometry parameters listed in **Tab. 7.3** are selected. Number of turns is swept from one turn to the maximum possible turns within the coil surface. In total, less than 1000 designs undergo brute force evaluation, and the entire evaluation takes less than three minutes.

The designs that fullfill the thermal limit and output voltage limit are considered as valid solutions, and are taken as the initial generation in GA optimization, based on which more generations are developed and explored. In the end, 111 designs fullfill the constraints, and among them, 100 designs are randomly selected as the initial population for the GA optimization.

7.1.4 Results

The optimization is done with the "gamultiobj" function in Matlab. The main function options are shown in **Tab. 7.4**. Other features not specified here are assigned default values in [177]. The Pareto front shown in **Fig. 7.2** is generated as the result of the optimization flow. The trade off between small coil size and high efficiency is clearly observed. In order to verify the power transfer capability of optimization results, a turning point on the Pareto front marked with star is prototyped and tested. This coil pair with small radius of 71 mm has 87 % AC-AC power transfer efficiency.

The prototyped coil pair winding geometry is shown in **Tab. 7.5**. The primary and secondary coil has similar outer radius which brings better coupling. For both primary and secondary sides, the trace width is below 8 mm and the space-width ratio is below 0.8. The photos of the prototyped coils are shown in **Fig. 7.3a** and **Fig. 7.3b**.

Tab. 7.3 Brute force search space

Sweeping inputs	Characteristics	values to evaluate	Units
Outer radius	r_{outp}, r_{outs}	[20, 39, 57, 75]	mm
Copper trace width	w_p, w_s	[1,4,7,10]	mm
gap-width ratio	gwr_p, gwr_s	[0.1, 0.6, 1, 1.5]	mm

Tab. 7.4 Options of "gamultiobj" function

Option	Description	Value
PopulationSize	Size of population	100
DistanceMeasureFcn	The distance function maintains diversity on a front by favoring individuals that are relatively far away on the front	@distancecrowding,'genotype'
FunctionTolerance	The algorithm stops if the average relative change in the distance of pareto front over MaxStallGenerations (= 50) generations is less than or equal to FunctionTolerance	1e-3

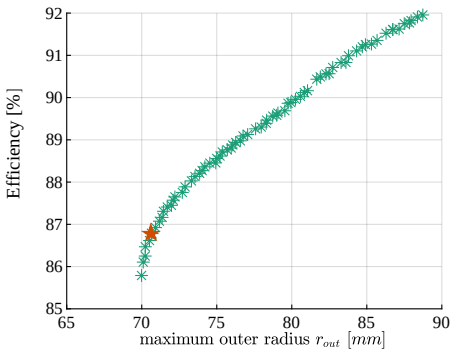

Fig. 7.2 Pareto front of coil designs. The prototyped design is marked with star.

(a) (b)

Fig. 7.3 (a) Prototyped primary coil (b) Prototyped secondary coil.

Tab. 7.5 Parameters of the prototyped coils

Specifications	Features	characteristics
primary coil		
outer radius	r_{outp}	70.70 mm
trace width	w_p	7.67 mm
turns gap	s_p	4.14 mm
turns number	n_p	3
space-width ratio	$\frac{s_p}{w_p}$	0.54
secondary coil		
outer radius	r_{outs}	70.66 mm
trace width	w_s	4.54 mm
turns gap	s_s	3.50 mm
turns number	n_s	4
space-width ratio	$\frac{s_s}{w_s}$	0.77

7.2 Experiment Results

7.2.1 Coil characteristics test

The coil pair is tested with LCR meter at 500 kHz and results are listed in **Tab. 7.6** together with optimization flow prediction results and FEM simulation results. The errors between prediction results and test results are below 5%.

7.2.2 Partial discharge test

The IPT coil pair is designed for a MV converter with a working voltage of 6 kVrms. As discussed in **Sec. 4.4.1**, the primary and secondary coils are separated with 60 mm distance to withstand this voltage stress. In the air gap between coils, partial discharge (PD) can cause failure by gradual erosion or treeing leading to puncture or surface flashover. In order to verify the insulation capability between the primary coil and secondary coil, the PD test is performed.

The coil is tested with the high voltage setup shown in **Fig. 7.4a** inside a Faraday cage. The setup consists of a voltage divider, a step-up high voltage transformer, a current limiting resistor and a high voltage coupling capacitor. The MPD 600 from Omicron is used to measure the PD level during the test. The illustration of setup is shown in **Fig. 7.4b**.

The background noise is first tested with 0.4 U_n, where U_n represents the nominal working voltage of 6 kV in our application. The noise PD level is tested to be 0.2 pC. Extracted from the standards IEC 61800-5-1 [127] and IEC 60664-1 [178], the PD test waveform is shown in **Fig. 7.5**. U_{PD} is the rated discharge voltage, which is the recurring peak voltages in the test system. According to 5.3.3.2.4 in

Tab. 7.6 Modeling, FEM and test results of inductance and resistance of the coil pair. The error is the difference between modeling result and test result.

Coil pair	$L_p[\mu H]$	$L_s[\mu H]$	$R_p[m\Omega]$	$R_s[m\Omega]$	$L_m[\mu H]$
ANN	1.97	3.82	85	172	0.56
2D FEM	1.95	3.80	84	168	0.53
Test	1.93	3.75	82	164	0.54
Error	2%	1.8%	3.6%	4.8%	3.7%

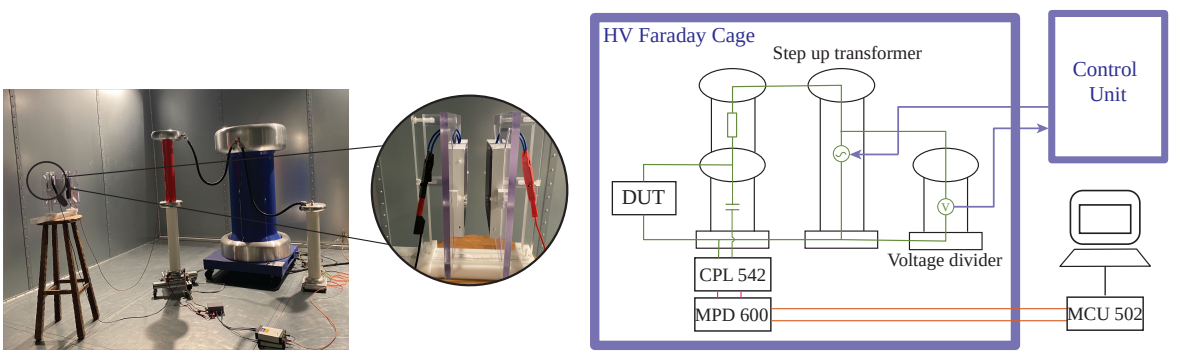

(a) (b)

Fig. 7.4 PD measurement setup inside the Faraday cage (a) photo of test setup (b) illustration of test setup.

[178], the maximum recurring peak voltage can be assumed to be $1.1 \times \sqrt{2}U_n = 6.6 \times \sqrt{2}kV$. During the test, the voltage is increased from 0 V to $1.875U_{PD}$ and held for maximum 5 s. If the PD has occurred, the voltage is decreased to $1.5U_{PD}$ and held for a maximum time of 15 s and the PD is measured during this time period.

The coil pair as shown in **Fig. 7.7** is tested under 12.375 kVrms for 5 s, and 9.9 kVrms for 15 s, and the test result is shown in **Fig. 7.6**. **Fig. 7.6a** shows the test voltage waveform and phase resolved PD. The source of the distorted voltage is from the power connection at the test location. The maximum PD exceeds 10 pC, however it happens during the pre-stressing stage as shown in **Fig. 7.6b**. The detected PD is less than 10 pC during the measurement period, therefore the test is considered successfully passed [127]. From the PD pattern, it can be seen that the cluster accumulates around the maximum and minimum of the AC voltage, and the occurrence phase is between 0 to 90° and 180° to 270°, which signifies surface discharge, which could happen between the insulation varnishing of the copper winding and the air [179], [180], or corona discharge in air, which could happen due to soldering point on PCB.

7.2.3 Power test

In order to test the power transfer efficiency, the coil pair is tested with the testbench shown in **Fig. 7.8**, with a nominal load of 10 Ω, input voltage of 80 V and operating frequency of 500 kHz.

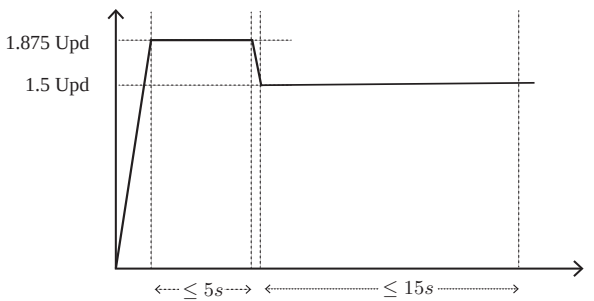

Fig. 7.5 Test voltage sequence applied to the IPT coils during PD test extracted from the standards IEC 61800-5-1 [127].

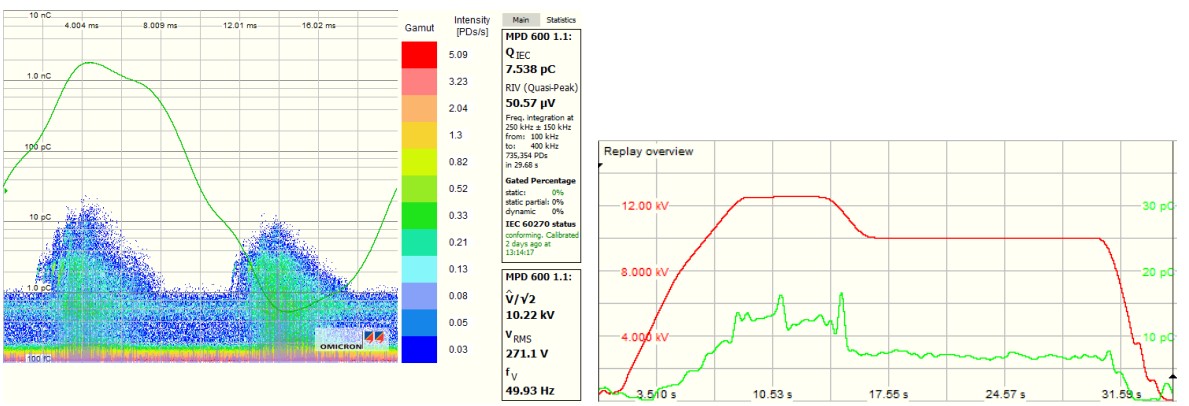

(a) (b)

Fig. 7.6 (a) Measured accumulated PD between primary and secondary coil. (b) RMS value of test voltage and measured instant PD.

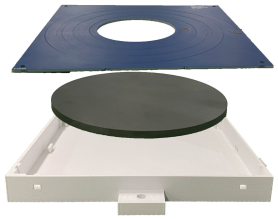

Fig. 7.7 The structure of the coil under PD test. No electrical connections between the enclosure, ferrite, or printed circuit board. There is no exposed copper on the outer surface of the printed circuit board. Solder joints are located only on the backside of the printed circuit board.

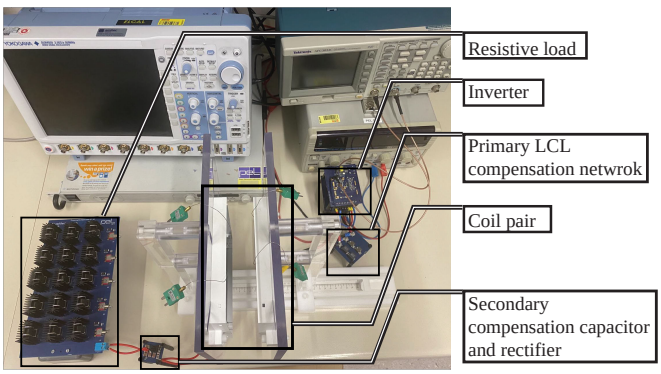

Fig. 7.8 Test bench of a coil pair consists of a DC power source, full bridge inverter, the primary side compensation network, primary coil, secondary coil, the secondary side compensation network, rectifier and resistor load.

Other components in the test bench are: the primary coil is connected to a GaN HEMTs based full bridge inverter (Infineon, EVAL-1EDF-G1-HB-GAN). The secondary coil is connected to Schottky diode based passive half bridge rectifier (ST, STPS30M60DJF). The LCL compensation network is used on primary side and series compensation network is used on secondary side. TDK MLCC capacitors are used due to low ESR. High power high frequency inductors are used as compensation inductor.

The test results are shown in **Fig. 7.9**. With an input DC voltage of 80 V, 33 V is observed at DC output. The voltage before the compensation network is a square wave, and the current is a distorted waveform composed of fundamental and high frequency harmonics. After the compensation network, the current through the primary coil and voltage across it are sinusoidal waveforms of fundamental frequency. The induced current to the secondary side is of fundamental frequency due to the compensation capacitor on the secondary side. However the voltage across secondary coil shows a voltage jump at the current zero crossing point, which can be explained by the voltage potential change of the rectifier capacitors when the current direction changes.

In order to verify the temperature rise is within safety limit, the temperature in each coil is measured with thermocouples. Four thermocouples are inserted in each coil and placed on four different layers: the surface of PCB copper trace, between the PCB and ferrite, between ferrite and enclosure, and on the bottom surface of coil holder. In each layer, the thermocouple is on the most inner turn of spiral coils.

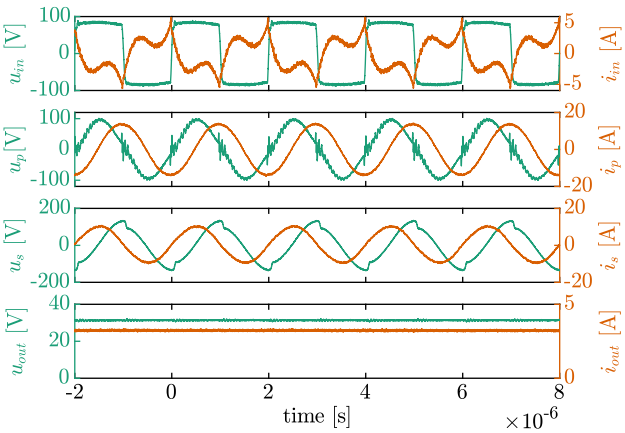

Fig. 7.9 Voltage and current waveform at nominal load. From top to bottom: input voltage and current between inverter and compensation network; voltage and current of the primary coil; voltage and current of the secondary coil; output DC voltage and current of load.

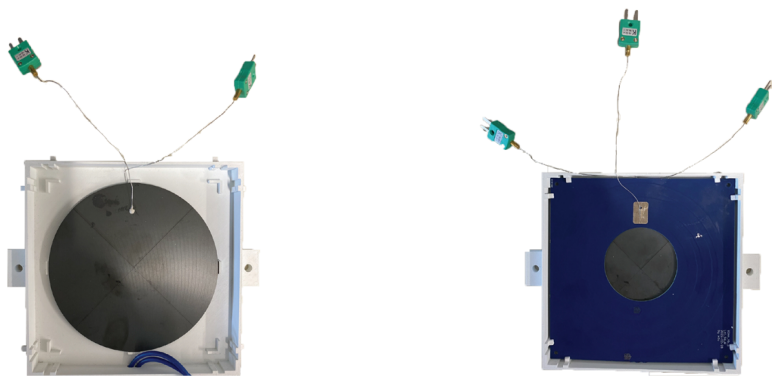

(a) (b)

Fig. 7.10 Prototype with thermal couples (a) inserted between ferrite and PCB (b) on the top surface of PCB.

Comparing to **Chap. 6**, minature thermocouples plug type K XF-1046-FAR which have smaller diameter at 0.5 mm are used to measure the surface temperatures. Thermally conductive silicon adhesive is used to fix the thermocouples between the inner surfaces (between enclosure and ferrite, between ferrite and PCB) as shown in **Fig. 7.10a**, and thermopads are used to fix the thermocouples on the outer surfaces (on PCB and on enclosure) as shown in **Fig. 7.10b**.

The stabilized temperature is measured and shown in **Fig. 7.11** together with the calculated temperature from thermal network model. It can be seen that the error between the measured surface temperature and calculated surface temperature is within 3 °C. In each coil, the hottest temperature is at the copper layer. This is because most losses in this coil system appear on the winding. The backside of the coil shows the lowest temperature and has a large temperature gap with the ferrite layer, which is due to the thick plastic wall on the backside (composed of the back coil enclosure and the coil holder, as shown in **Fig. 7.8**).

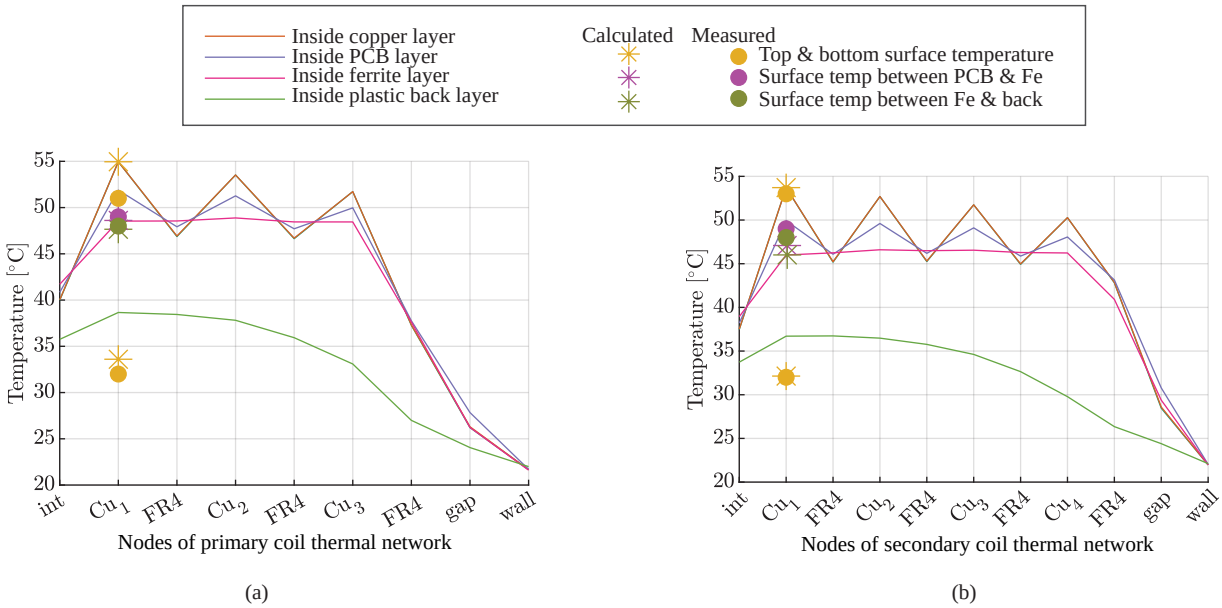

Fig. 7.11 Measured and calculated temperature in different layers in (a) primary coil (b) secondary coil. Stars '*' are the calculated surfaces temperatures. Dots '·' are the measured surfaces temperatures. Lines '-' are the calculated temperature at each node inside each layer.

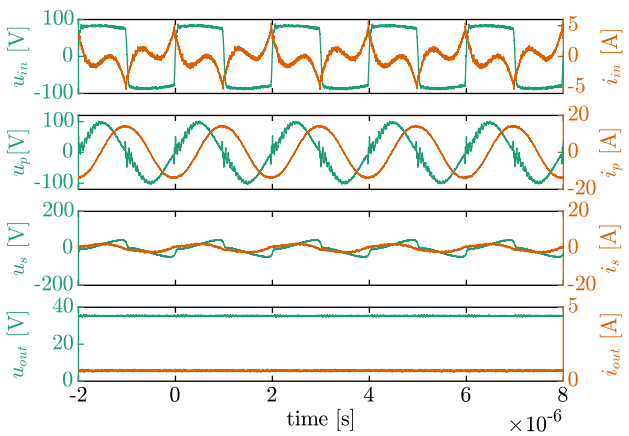

Fig. 7.12 Voltage and current waveform at 50 Ω load. From top to bottom: input voltage and current between inverter and compensation network; voltage and current of the primary coil; voltage and current of the secondary coil; output DC voltage and current of load.

7.2.4 Load condition change

The developed IPT coil pair is supposed to serve as APS for power electronics converters, and the load condition of IPT system could change as the main power converter state changes. In the power test, a resistor bank is connected to the IPT as the load to imitate a PEBB. By switching on and off resistors, the load change can be controlled. As a representation, the voltage and current at 50 Ω load are shown in **Fig. 7.12**. Comparing to the waveforms at nominal load condition in **Fig. 7.9**, the load current reduces significantly, however the primary side current stays the same.

A N4L PPA5530 Precision Power Analyzer is used to analyze the DC-DC efficiency. The output

Tab. 7.7 Output voltage, output power and efficiency of different load conditions.

Resistive load	50 Ω	25 Ω	16.7 Ω	12.5 Ω	10 Ω
Output voltage	36.26	35.43	34.56	33.65	32.82
Output power	26.88	51.23	72.97	92.08	109.42
DC-DC efficiency	0.55	0.68	0.73	0.75	0.75

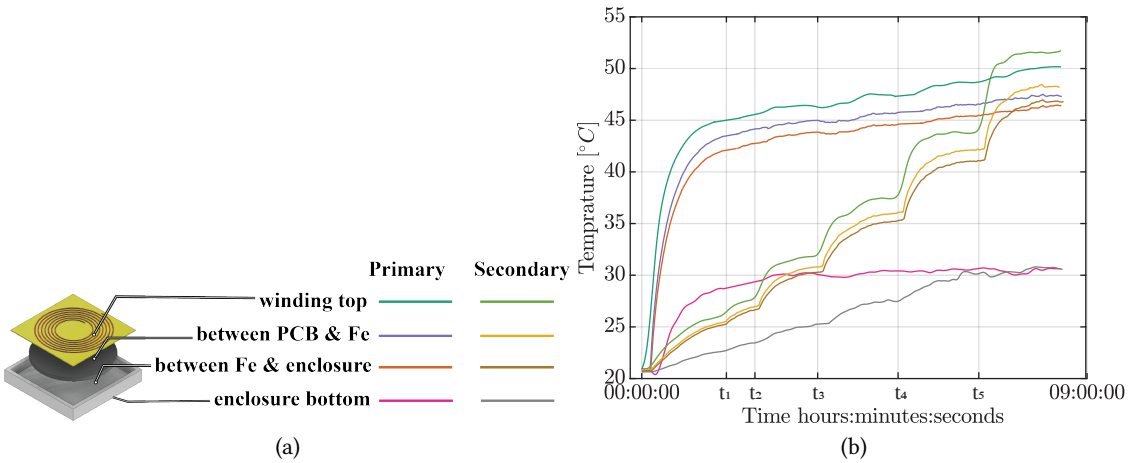

Fig. 7.13 Temperature rise in both coils in different layers. The load is disconnected with the secondary coil at initial state. (a) The illustration of thermal couple positions. (b) Recorded temperature. From time t_1 to t_5, the load connection rises from 20%, 40%, 60%, 80% to full load.

voltage, output power and DC-DC efficiency with different load conditions are shown in **Tab. 7.7**. The nominal load resistor is 10 Ω. When the resistor increases five times (the load drops to 20% of nominal load), the voltage varies slightly and stays within the range [32.82 V, 36.26 V]. The voltage source behavior of the IPT system is therefore verified. In addition, it can be observed that when the load drops, the power transfer efficiency drops as well, and the highest efficiency appears at nominal load condition.

The temperatures in both coils are recorded while the load gradually connects to the secondary side. When the temperature is observed starting to stablize (at t_1,...t_5), 20 % load step is applied to the secondary side at each time point. As shown in **Fig. 7.13**, at initial state, the load is disconnected to the secondary coil. The temperature on the secondary side is not rising due to negligible power loss on the secondary side, however temperature on the primary coil rises rapidly. When the load increases from no load to full load by adding 20% each time, the secondary side coil becomes hotter at each time point due to higher loss, and the load change can be clearly seen in the temperature rise pattern in secondary coils. In the meantime, the temperature variation of primary side is within 5 °C from no load to full load condition. This further verifies that the current through primary coil is stable regardless of load change.

Tab. 7.8 Key components in the IPT system

Components	Parts number	Quantity
primary side inverter transistors	GaN IGOT60R070D1	8
primary side compensation inductor	Wurth Elektronik WE-HCF 7443320068, 0.68uH	2
	TDK SPM10040T-R47M-HZ 0.47uH	2
primary side compensation capacitor	NP0 ceramic capacitor 22 nF	8
secondary side compensation capacitor	NP0 ceramic capacitor 6.8 nF	4
secondary side rectifier diodes	power Schottky diodes STPS30M100DJF	4

7.3 Power Loss Analysis

In the design process of IPT coils, the losses on the inverter, rectifier and compensation networks were neglected. And this leads to the difference of the measured DC-DC efficiency and predicted AC-AC efficiency. The components used in the IPT power transfer link are listed in **Tab. 7.8**. The loss analysis under nominal load is done with the measured waveform in **Fig. 7.9**. The primary side inverter is a full bridge inverter. In each leg, there are two 600 V GaN transistors in parallel to reach the high current capability. In total eight GaN transistor are in the inverter stage. The primary side compensation inductance is composed of four inductors connected in series to reach 2.3 µH in total. The primary compensation capacitor is composed of eight NP0 capacitors of 22 nF. Four branches of capacitors are in parallel to increase current capability and in each branch there are two capacitors connected in series.

- GaN inverter losses

  The inverter works with fixed duty cycle at 0.5. The GaN transistors in the inverter operation has conduction loss, reverse conduction loss, switching losses, and gate driving losses. The conduction losses , reverse conduction loss and gate driving losses are calculated following application note [181]. In each leg in the full bridge inverter, there are two GaN transistors in parallel. The current through each GaN during its conduction phase is

  $$I_{gan.rms} = \frac{I_{in.rms}}{2} \tag{7.6}$$

  where, $I_{in.rms}$ is the rms value of input current. Each transistor conducts only for half period, and the loss of each GaN in one period is

  $$P_{gan.cond} = 0.5 \cdot I_{gan.rms}^2 R_{on(80^\circ C)} = \frac{I_{in.rms}}{8} R_{on(80^\circ C)} \tag{7.7}$$

  where, $R_{on(80^\circ C)}$ is the conduction resistance at $80^\circ C$ for each IGOT60R070D1 GaN transistor, extracting from datasheet it is $0.077\,\Omega$. There are in total eight GaN transistors in the inverter, and the total conduction loss in the inverter is

  $$P_{inv.cond} = I_{in.rms}^2 R_{on(80^\circ C)} \tag{7.8}$$

  During dead-times, when the channel is turned off, and before turn-on, the GaN transistors operate in reverse conduction mode (third quadrant). The current passes through GaN devices and there is a voltage drop V_{SD} over the device. According to the datasheet, with the negative

gate voltage at −2.5 V, V_{SD} = 4.5 V. All the eight transistors have the same deadtime, and the reverse conduction loss can be calculated as

$$P_{reverse.cond} = 8 \cdot \frac{I_{avg}}{2} \cdot V_{SD} \cdot DeadTime \cdot f = 4 \cdot I_{avg} \cdot V_{SD} \cdot DeadTime \cdot f \tag{7.9}$$

where, I_{avg} is the average value through one leg in the time interval t=[0, deadtime]. Deadtime is 100 ns. The average current is extracted and calculated from the test data.

Due to the ZVS at turn-on, GaN in the rectifier has only turn-off losses as switching losses. For switching turn-off losses, the test characterization is done under nominal load condition. The voltage and current of one GaN device during turn-off at nominal load condition is shown in **Fig. 7.14**. The turn-off losses for eight GaN transistors is:

$$P_{sw,off} = 8 \cdot E_{off} \cdot f \tag{7.10}$$

Gate driving losses are caused by the energy required to charge the GaN gate. That is, the Q_g at the gate voltage of the circuit. And it counts for both turn-on and turn-off gate losses. The driving losses in the eight GaN transistor is

$$P_{gate} = 8 \cdot (V_{gs,p} - V_{gs,p}) \cdot Q_g \cdot F_{sw} \tag{7.11}$$

where, $Q_g = 5.8nC$, $V_{gs,p} = 3.6V$ and $V_{gs,s} = -6V$ are the positive and negative gate drive voltage levels respectively. The GaN power losses in the full bridge is

$$P_{GaN} = P_{cond} + P_{reverse.cond} + P_{sw,off} + P_{gate} \tag{7.12}$$

- Compensation network losses
  In the primary side compensation network, there is inductor L_{pc} and capacitor C_{pc}. On the secondary side, there is compensation capacitor C_{sc}. The losses on these components need to be considered. The primary side compensation inductor is composed of two inductors of 0.68 uH from Wurth Elektronik and two inductors of 0.47 uH from TDK. There are two purposes of selecting these components: firstly, to achieve the total inductance value that is closest to the desired compensation inductance; secondly, to have low losses at the nominal operating point. Loss of two inductors at 0.68 uH from Wurth Elektronik can be calculated by its loss tool [182], which at $I_{in.rms}$, 500 kHz is 408 mW. Two of them would have loss at 816 mW. Two inductors

Fig. 7.14 Voltage and current of one GaN device during turning off at nominal load condition.

from TDK have quality factor at 500 kHz to be 83.5, quality factor at 1.5 MHz is 56.4, and at 2.5 MHz is 51.2.

The losses on the two TDK inductors are approximated as

$$P_{ind} \approx 2 \cdot (I_{in.1st}^2 \frac{wL}{83.5} + I_{in.3rd}^2 \frac{3wL}{56.4} + I_{in.5th}^2 \frac{5wL}{51.2}) \tag{7.13}$$

The NPo ceramic capacitors have low dissipation factor $DF \approx 0.1\%$ and therefore are used as compensation capacitors. The current through primary side compensation capacitors is

$$I_{Cp} = I_{in} - I_p \tag{7.14}$$

where, I_{in} and I_p are from test data. Considering the primary capacitors are four branches in parallel and each branch has two capacitors, the loss on the primary side compensation capacitor is

$$P_{Cp} = 8 \cdot \frac{I_{Cp.rms}}{4}^2 \cdot \frac{0.1\%}{\omega C_{pc}} \tag{7.15}$$

On the secondary side, there are four capacitors connected in parallel to form the compensation capacitor. The loss on the secondary side compensation capacitor is

$$P_{Cs} = 4 \cdot \frac{I_{s.rms}}{4}^2 \cdot \frac{0.1\%}{\omega C_{sc}} \tag{7.16}$$

where $I_{s.rms}$ is the rms current through the secondary coil and compensation capacitors, which can be obtained from the test waveform.

- Rectifier diode losses
  The average forward current through one rectifier branch is

$$I_{f.avg} = 0.45 I_{s.rms} \tag{7.17}$$

  In each branch, there are two diodes in parallel. In total, there are four shottky diode from STPS30M100DJF of rating 100V, 30A are used. At 125 °C junction temperature, $U_f = 0.4 + 0.015 \cdot I_f$ The loss on the diode is calculated as

$$P_{dio} = 4 \cdot (0.4 \cdot \frac{I_{f.avg}}{2} + 0.5 \cdot 0.015 \cdot (\frac{I_{s.rms}}{2})^2) \tag{7.18}$$

- Connector and wire losses
  In addition to the losses on coil pair, GaN switches, compensation networks and diodes, there are losses on the connector and wires which also play an important role in high frequency operation. This loss is obtained by deducting other losses from the total loss

$$P_{other} = P_{in} - P_{out} - P_{GaN} - P_{ind} - P_{Cp} - P_{Cs} - P_{dio} - P_{coil} \tag{7.19}$$

The test waveform at nominal load shown in **Fig. 7.9** is taken into calculation of losses. The loss decomposition is shown in **Fig. 7.15**. The losses on coils count 46% of total loss. In addition to that, the loss on connectors and wires are the second largest loss which count 24% of total loss. Other losses mainly appear on GaN devices, on diodes and on primary compensation inductors. Further efficiency improvement can be achieved by optimizing wire layouts and paralleling components.

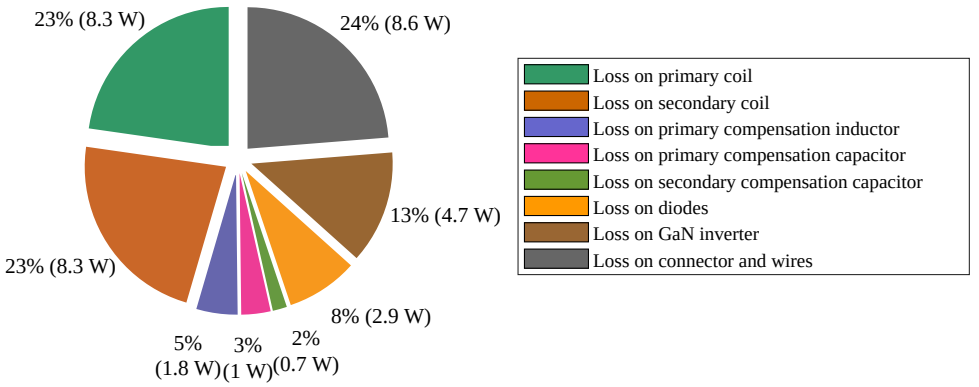

Fig. 7.15 Losses distribution in the prototyped IPT system at nominal operation point.

7.4 Summary

This chapter proposes an optimization flow for winding geometries of IPT PCB based IPT coils. As a demonstration, the optimization is done for electric specifications defined for APS in MV converters and is for coils with round shape 5 mm thick ferrite on its backside. This optimization flow is capable to be generalized to other electric specifications and ferrite geometries. The optimization integrates electric circuit model, magnetic model and thermal model. The optimization is fully based on Matlab, without the need to call external simulations, which permits fast optimization within three hours.

One coil pair with outer radius of 71 mm from the Pareto front is prototyped, and different tests are done on it. Firstly, the coil pair is tested with impedance analyzer, which further validates the accuracy of the magnetic model proposed in **Chap. 5**. Then the coil pair is tested under different load conditions. The DC-DC efficiency under nominal load condition for this coil pair is 75%. In addition, the temperature is measured on distinct layers of the coil system, thereby confirming that the coil system operates within the temperature limit, which further reinforces the validation of thermal model proposed in **Chap. 6**.

In addition, based on the test data, the losses decomposition on the DC-DC link is analyzed for the nominal load condition. The results indicate further optimization direction on the connectors, wires and inverter.

8 Conclusion and Future Works

This chapter provides a comprehensive summary of all the contributions of this thesis in the emerging field of PCB based loosely coupled IPT system. These contributions highlight the advancements and novel insights thorough the research conducted. In addition, the future research possibilities resulting from the work done in this thesis is elaborated.

8.1 Summary and Contributions

This thesis focuses on the solutions for independent APSs for the MV converters. Those APSs usually require high insulation capability. **Chap. 2** reviews the existing solutions for independent APS in MV converters and compares them in different perspectives. Considering that in addition to its flexibility and therefore convenience, the IPT offers intrinsic insulation barrier due to the contactless nature, it is considered as a potential solution for APS. However, the large insulation distance leads to a loosely coupled system which brings challenges to achieve high efficiency IPT system. Therefore the IPT system needs to be optimized to achieve high power transfer efficiency and high power density. The coil link, including the compensation network and the primary and secondary coils, is the critical part in an IPT system. **Chap. 2** discusses the design space within the coil link, which includes the coil shape, the winding construction, the magnetic shielding, compensation network and input and output converters. With discussion on all the possible coil geometries, PCB based circular spiral winding is chosen due to its standardized manufacturing. With discussion on magnetic cores, ferrite is selected as the magnetic shielding material due to its low eddy current loss. To accommodate the modular structure of PEBBs, an IPT configuration featuring multiple independent output channels is defined. The free parameters to be discussed and included in the optimization process are the winding geometries, the ferrite shapes and the compensation network. These design freedoms are multi-physically coupled. And the optimization needs the knowledge of electric model, magnetic model and thermal model, which are discussed later in the thesis chapter by chapter.

Chap. 3 focuses on the compensation network design. It first discusses four basic compensation networks on their output behavior and resonance frequency. Inspired by these designs, LCL-S compensation network is proposed to achieve independent and stable output voltage on each secondary. LCL-S ensures the stable current through series connected primary coils, and therefore stable voltage transferred to the secondary side regardless of load conditon. The detailed design process for LCL-S network is explored to achieve optimal efficiency, slightly inductive input impedance, and stable outputs simultaneously. Later, by fixing the quality factor of coils, the influences of coupling factor k, switching frequency f and primary side inverter topology on the component values and coil link efficiency are analyzed. It shows that full bridge inverter on the primary side achieves smaller difference between primary and secondary coil inductance and therefore higher potential to have

better coupling.

The magnetic model for PCB windings without magnetic shielding is developed in **Chap. 4**, presenting several key contributions. Initially, an enhanced magnetic field distribution model is introduced for coils with rectangular cross-section, providing higher accuracy than the filament approach while ensuring fast calculation. Additionally, the model enables efficient characterization of PCB coils, encompassing self and mutual inductance and resistance. Furthermore, an analysis of coil geometries reveals the critical importance of maintaining a small gap between traces and an appropriate coil's inner radius to achieve a high quality factor of the coil. Ultimately, an optimization flow on the winding geometry is proposed based on the brute force search. The optimization allows users to define design specifications and constraints, and conducts the exploration of the entire design space. From the Pareto front, a coil pair capable of transferring 110 W over a 60 mm air gap was prototyped and tested. In addition, the test with multiple coils connected to the same source while supplying distinct loads is executed, which proves the independent outputs of the proposed IPT structure.

Ferrite is usually added in the IPT system to increase the coupling between primary and secondary coils, as well as to achieve better EMI performance. **Chap. 5** examines the influence of ferrite on coil pairs and builds the magnetic model to predict the characteristics for arbitrary winding geometries. The existence of ferrite on the back side of coils would influence both quality factor and coupling factor. The examination begins with an analysis of various ferrite geometries, including surface shapes and thickness. The results indicate that round and rectangular-shaped ferrite, with a thickness exceeding 1 mm, demonstrate superior performance in terms of coupling and quality factors. Subsequently, a magnetic model is introduced specifically for coil pairs equipped with round-shaped ferrite measuring 5 mm in thickness. This model accurately predicts key characteristics of coils, such as coil inductance, winding resistance, and core losses, for coil pairs with arbitrary winding geometries. The development of this magnetic model is based on ANN in conjunction with FEM data, with pre-verification of the accuracy of the FEM data. The model is implemented in Matlab, facilitating seamless integration into the optimization process. The initial accuracy verification of the model is accomplished using extra test data obtained from FEM simulations. And further verification is done with test in **Chap. 7**.

The temperature within a coil impacts its overall performance. In **Chap. 6**, a thermal model is introduced, aiming to accurately predict the steady-state temperature at each component in a coil. This thermal model is built to achieve high accuracy, low computation time, and seamless integration into the optimization process. The proposed model takes into account conduction, convection, and radiation effects as dissipation methods. It considers the axial symmetrical geometry of the coil and constructs a thermal network in both axial and radial directions. The model enhances accuracy by iteratively updating the convection and radiation resistance to predict the temperature rise. Moreover, the proposed model does not require measurements or simulations. Compared to CFD simulations, the proposed model permits fast calculation. Additionally, being fully analytic, the model can easily integrate into optimization process. Furthermore, the thermal model is designed to be adaptable to various coil geometry. Once the PCB, ferrite and enclosure geometry are provided, the thermal network can be rapidly and effortlessly generated. In the end, tests with different coil geometries and orientations, under various ambient temperatures, are performed and verified the generality and accuracy of the thermal model.

With the electric model proposed in **Chap. 3**, the magnetic model in **Chap. 5**, and the thermal model in **Chap. 6**, the design and optimization can be done on winding geometries in a coil link. The optimization method is detailed in **Chap. 7**. The optimization is specifically applied to meet the

electric specifications outlined by APS in MV converters and focuses on coils with a round shape and a 5 mm thickness ferrite on the backside. However, this optimization process can be extended to apply to other electric specifications and ferrite geometries. The optimization process incorporating electric, magnetic, and thermal modeling techniques, are entirely implemented in Matlab, eliminating the need for external simulations and enabling rapid optimization within a three-hour time frame. As a result, a coil pair is selected from the Pareto front and subsequently prototyped. Under nominal load conditions, the coil pair exhibits a DC-DC efficiency of 75%. Additionally, based on the test data, a detailed analysis is conducted to decompose the losses on the DC-DC link under the nominal load condition. The results of this analysis identify potential directions for further optimization.

8.2 Future Work

The work presented in this thesis covers the development of an PCB based IPT coil link for the APS in MV converters. Various models are built for the coils including electric model, magnetic model and the thermal model. The knowledge on these models allows to fastly optimize the coil winding geometry to achieve high efficiency and high power density. The optimized coil pair is prototyped and tested to verify proposed models and functional operation. To further optimize the IPT system, more work can be done.

8.2.1 Optimization on winding structure

In order to reduce the high frequency loss, instead of a single strand on PCB, the winding can be realized in 3D litz routing pattern [183]. Similar to litz wire, there are some important parameters to consider. Firstly, the thickness and width per strand determines the influences of skin effect. In order to avoid the skin effect from all the surfaces of the rectangular trace, the thickness and width of each copper trace should be less than twice of the skin dept. However the minimum width of the strand is restricted by the PCB fabrication technique. Secondly, the number of strand influences the proximity effect and this should be optimized to achieve low AC resistance of winding.

8.2.2 Modeling on metallic shielding

The IPT system is supposed to serve as APS for MV converters which are usually mounted in metallic cabinet. Therefore the IPT coil will have metal in its surroundings. When the metal is exposed to a time-varying magnetic field, electric currents are induced due to variation of the field with time. These circulating eddy currents induce magnetic fields that counteract the incident magnetic fields penetrating the material, resulting in a reduction of the net magnetic field in the vicinity of the metal. Having metal in the vicinity of the coils would require a new model of coil characteristics: the self inductance and coupling of coils decrease, in the meantime the coil equivalent resistance increases. Eventhough with ferrite placed between the winding and metallic shielding, the leakage flux reaching the aluminum shielding is greatly reduced, the effect still needs to be well understood to get accurate models to predict coil performance.

8.2.3 DC-DC link efficiency optimization

The DC-DC efficiency of the final prototype is 74%. According to the loss decomposition in **Chap. 7**, the losses on the other parts in addition to the coils count more than 50% loss. For the primary side

inverters, the conduction losses on the GaN devices can be reduced by changing to low resistance GaN devices or paralleling more devices in parallel. The reverse conduction losses of GaN devices can be reduced by lowering the deadtime. The switch off losses can be reduced by optimizing the GaN gate driving circuit. On the secondary side, the losses on the rectifier can be optimized by using more diodes in parallel. In addition, the wiring and the connectors from wire to board should be optimized.

8.2.4 Development of impedance matching network

During implementation of coil, wiring could bring unpredictable inductance in the coil link. This would alter the resonant tank on primary and secondary side from their optimal operating point. An impedance detection and matching network which can smartly adjust according to real coil inductance would facilitate the implementation process. In addition, by adjusting the impedance matching network, the output voltage can be regulated precisely. This necessity arises, because with a fixed impedance matching network, as presented in this thesis, the output voltage varies when the load changes.

Appendices

A

Thermal dissipation mechanism

A.1 Conduction

Conduction refers to the process of heat transfer within a material or between two materials that are in direct physical contact. The heat transfers from the hot region to the cold region due to the random movement of atoms or molecules within the material. The rate of heat transfer by conduction is dependent on the solid material, as well as the temperature difference between the two regions. Materials with high thermal conductivity, such as metals, are good conductors of heat and will allow heat to pass through them more quickly than materials with low thermal conductivity, such as plastics.

Heat flux through the objects per unit area perpendicular to the dissipation direction q''[W/m^2] is proportional to the temperature gradient [K/m], known as the Newton's law of cooling [165]:

$$q'' = \frac{q_{cond}}{A} = -k\nabla T(x, y, z) \tag{A.1}$$

where, k is a transport property known as the thermal conductivity [W/mK] and is a characteristic of the object material. The minus sign is a consequence of the fact that heat is transferred in the direction of decreasing temperature. By integrating the heat flux inside the objects, the total power transferred through the objects is:

$$Q_{1,2} = \frac{T_{hot}(1) - T_{cold}(2)}{R_{th}} \tag{A.2}$$

where, $Q_{1,2}$ is the heat flux [W] that flows from the hotter temperature $T_{hot}(1)$ (K) to the colder temperature $T_{cold}(2)$ through a thermal resistance R_{th} [K/W]. Thermal resistance needs to reflect the geometry and thermal conductivity of objects.

When the heat flux passes through a planar wall, the thermal resistance is defined as

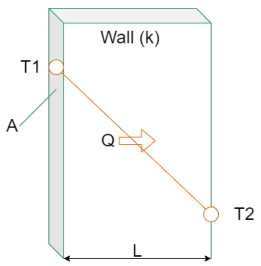

$$R_{th,cond} = \frac{L}{kA} \tag{A.3}$$

Fig. A.1 Conduction through a planar wall.

with L the thickness (m) of the wall through which the heat flow passes, k the thermal conductivity [W/mK] of the wall and A the area [m^2] of the wall through which the flux passes.

When heat flux passes through a radial wall, the thermal resistance is

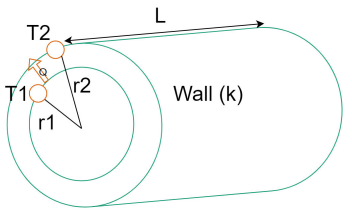

$$R_{th,cond} = \frac{ln(r_2/r_1)}{2\pi Lk} \tag{A.4}$$

Fig. A.2 Conduction through a radial wall.

A.2 Convection

Convection heat transfer is a process that occurs between a fluid in motion and a boundary surface when they are at different temperatures. There are two main convection processes [165]:

- the forced convection which occurs when the fluid in forced motion comes into contact with a surface of a different temperature.
- the natural convection which occurs when the difference in temperature between a surface and the surrounding fluid generates a movement in this fluid, through the change in density of the latter, which is induced by the non-homogeneity of its temperature.

Same for the conduction heat transfer, the heat flux equation, known as the Newton's law of cooling, is

$$q'' = \frac{q_{conv}}{A} = h(T_s - T_\infty) \tag{A.5}$$

with q'' [W/m^2] the heat convection flux that is proportional to the temperature difference between the surface T_s and air temperatures T_∞, and h [W/m^2K] the convection heat transfer coefficient.

The power [W] transferred by convection is calculated as:

$$q_{conv} = \frac{T_s - T_\infty}{R_{th}} \tag{A.6}$$

where R_{th} is a function on the thermal convection coefficient and the convection surface area:

$$R_{th,conv} = \frac{1}{hA} \tag{A.7}$$

Thermal convection coefficient h is a number dependent on the environment conditions and object characteristics including the air viscosity, air and object temperature and the test object geometries, positions, materials, etc. The object's orientation will influence the convection coefficient. For a bottom hot surface facing downwards, as shown in **Fig. A.3a**, the air's tendency to descend or ascend is hindered by the plate. The air must flow horizontally before it can move up or down from the edges of the plate, which reduces the effectiveness of convection heat transfer. On the other hand,

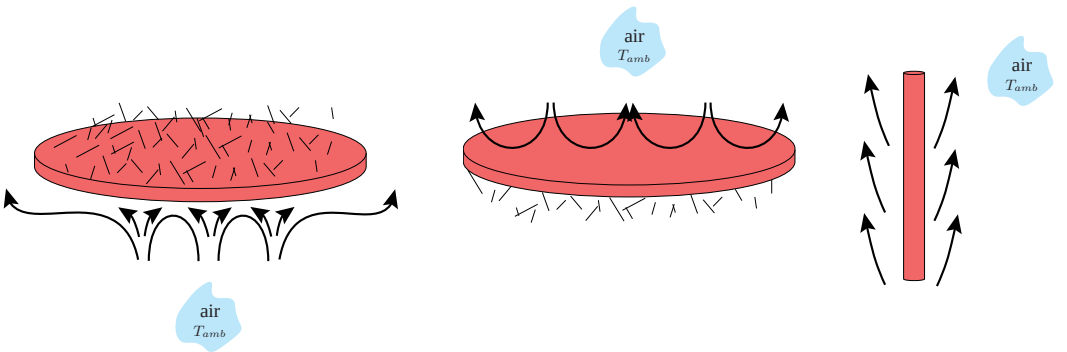

Fig. A.3 Buoyancy-driven flows on horizontal and vertical hot plates: (a) Top surface of hot plate. (b) Bottom surface of hot plate. (c) Side surface of hot plate.

for a top hot surface facing upwards, as shown in **Fig. A.3b**, the flow is driven by descending or ascending parcels of air, respectively, and it leads to more effective heat transfer. When the hot plate is vertically placed as shown in **Fig. A.3c**, the air is heated by the object and rises due to buoyancy forces, entraining the air from the quiescent region.

Taking all the environmental and object conditions into consideration, the average convection coefficient on a hot plane surface, can be formulated as:

$$h = \frac{k_{air} N_u}{L_c} \tag{A.8}$$

where, k_{air} is the thermal conductivity of air [$\mathrm{Wm^{-1}K^{-1}}$], and N_u is the average Nusselt number which represents the ratio of convective to conductive heat transfer at a boundary in the air and different for hot planes facing different directions. L_c is the characteristic length of the test object. k_{air} at atmospheric pressure is dependent only on the temperature of air. The characteristic length is reflecting the coil geometry and defined as the ratio between the surface area and perimeter $L_c = \frac{A}{P}$. N_u is a function of several factors [110]:

$$N_u = f(g, \beta, T_s, Ta, L_c, \nu, P_r) \tag{A.9}$$

where g is gravitational acceleration [$\mathrm{m/s^2}$], β is the coefficient of thermal expansion of air [$\mathrm{K^{-1}}$] and is dependent on atmosphere pressure and air temperature, T_s is the surface temperature [K], T_a is the ambient temperature [K], ν is the kinematic viscosity [$\mathrm{m^2/s}$], and P_r is the Prandtl number. It's practical to obtain Nusselt number N_u with empirical equations that are obtained by correlating measured convection heat transfer results. The empirical equations for Nusselt number are different when the hot plane is facing different directions.

- Heat transfer from a hot surface facing up. The Nusselt number is found to be:

$$Nu_L = \begin{cases} 0.54 \cdot Ra_L^{1/4} & \text{if } 10^4 < Ra_L < 10^7 \\ 0.15 \cdot Ra_L^{1/3} & \text{if } 10^7 < Ra_L < 10^11 \end{cases} \tag{A.10}$$

- Heat transfer from a hot surface facing down. The Nusselt number in this case is:

$$Nu_L = 0.27 \cdot Ra_L^{1/4} \tag{A.11}$$

Tab. A.1 Thermophysical properties of gases at atmoshpheric pressure [165].

T (K)	$\nu \cdot 10^6[m^2/s]$	$\alpha \cdot 10^6[\mathrm{m}^2/\mathrm{s}]$	Prandtl number Pr
250	11.44	15.9	0.720
300	15.89	22.5	0.707
350	20.92	29.9	0.700
400	26.41	38.3	0.690
450	32.39	47.2	0.686

- Heat transfer from a vertical hot surface. The Nusselt number in case of natural convection around a vertical plate is known as the Churchill & Chu formula:

$$Nu_L = \{0.825 + \frac{0.387 Ra_L^{1/6}}{[1 + (0.492/Pr)^{9/16}]^{8/27}}\}^2 \tag{A.12}$$

In the equations above, Ra_L is the Rayleigh number which characterizes the air's flow regime considering the air viscosity and buoyancy. Pr is Prandtl number.

$$Pr = \nu/\alpha \tag{A.13}$$

Rayleigh number is the product of Grashof and Prandtl numbers

$$Gr_L = \frac{g\beta(Ts - T_a)\, L^3}{\nu^2} \tag{A.14}$$

$$Ra_L = Gr_L\, Pr = \frac{g\beta(T_s - T_\infty)L^3}{\nu\alpha} \tag{A.15}$$

The air properties ν, α are defined at film temperature $T_f = \frac{Ts+T_\infty}{2}$ [K] by interpolating the values in **Tab. A.1**.

Bibliography

[1] A. Nabae, I. Takahashi, and H. Akagi, "A new neutral-point-clamped pwm inverter," *IEEE Transactions on Industry Applications*, vol. IA-17, no. 5, pp. 518–523, 1981.

[2] T. Bruckner and S. Bemet, "Loss balancing in three-level voltage source inverters applying active npc switches," in *2001 IEEE 32nd Annual Power Electronics Specialists Conference (IEEE Cat. No.01CH37230)*, vol. 2, 2001, 1135–1140 vol.2.

[3] T. Meynard and H. Foch, "Multi-level conversion: High voltage choppers and voltage-source inverters," in *PESC '92 Record. 23rd Annual IEEE Power Electronics Specialists Conference*, 1992, 397–403 vol.1.

[4] M. Narimani, B. Wu, Z. Cheng, and N. R. Zargari, "A new nested neutral point-clamped (nnpc) converter for medium-voltage (mv) power conversion," *IEEE Transactions on Power Electronics*, vol. 29, no. 12, pp. 6375–6382, 2014.

[5] P. Hammond, "A new approach to enhance power quality for medium voltage ac drives," *IEEE Transactions on Industry Applications*, vol. 33, no. 1, pp. 202–208, 1997.

[6] A. Lesnicar and R. Marquardt, "An innovative modular multilevel converter topology suitable for a wide power range," in *2003 IEEE Bologna Power Tech Conference Proceedings,*, vol. 3, 2003, 6 pp. Vol.3-.

[7] T. Ericsen, "Power electronic building blocks-a systematic approach to power electronics," in *2000 Power Engineering Society Summer Meeting (Cat. No.00CH37134)*, vol. 2, 2000, 1216–1218 vol. 2.

[8] A. Christe, M. Petkovic, I. Polanco, M. Utvic, and D. Dujic, "Auxiliary submodule power supply for a medium voltage modular multilevel converter," *CPSS Transactions on Power Electronics and Applications*, vol. 4, no. 3, pp. 204–218, 2019.

[9] J. Gottschlich, M. Schäfer, M. Neubert, and R. W. De Doncker, "A galvanically isolated gate driver with low coupling capacitance for medium voltage sic mosfets," in *2016 18th European Conference on Power Electronics and Applications (EPE'16 ECCE Europe)*, 2016, pp. 1–8.

[10] Y. Mo, H. Qin, W. Chen, *et al.*, "Auxiliary Power Supply with SiC MOSFET for Wide-Range High Voltage Input Applications," in *2020 IEEE 9th International Power Electronics and Motion Control Conference (IPEMC2020-ECCE Asia)*, Nov. 2020, pp. 137–141.

[11] J. Liu, S. Zhong, J. Zhang, Y. Ai, N. Zhao, and J. Yang, "Auxiliary Power Supply for Medium-/High-Voltage and High-Power Solid-State Transformers," *IEEE Transactions on Power Electronics*, vol. 35, no. 5, pp. 4791–4803, May 2020.

[12] A. Rodriguez, M. R. Rogina, M. Saeed, *et al.*, "Auxiliary power supply based on a modular isop flyback configuration with very high input voltage," in *2016 IEEE Energy Conversion Congress and Exposition (ECCE)*, Sep. 2016, pp. 1–7.

[13] O. S. Senturk, T. Maerki, P. Steimer, and S. McLaughlin, "High voltage cell power supply for modular multilevel converters," in *2014 IEEE Energy Conversion Congress and Exposition (ECCE)*, Sep. 2014, pp. 4416–4420.

[14] T. Modeer, S. Norrga, and H. Nee, "High-voltage tapped-inductor buck converter utilizing an autonomous high-side switch," *IEEE Transactions on Industrial Electronics*, vol. 62, no. 5, pp. 2868–2878, May 2015.

[15] Yaqiang Han, Wenjie Chen, Xiliang Chen, *et al.*, "A 4000v input auxiliary power supply with series connected sic mosfets for mmc-based hvdc system," in *2016 IEEE 8th International Power Electronics and Motion Control Conference (IPEMC-ECCE Asia)*, May 2016, pp. 279–284.

[16] T. Meng, C. Li, H. Ben, and J. Zhao, "An Input-Series Flyback Auxiliary Power Supply Scheme Based on Transformer-Integration for High-Input Voltage Applications," *IEEE Transactions on Power Electronics*, vol. 31, no. 9, pp. 6383–6393, Sep. 2016.

[17] J. Won, G. Jalali, X. Liang, Z. Chi, S. Srdic, and L. Srdjan M., "Auxiliary Power Supply for Medium-Voltage Power Converters: Topology and Control," *IEEE Transactions on Industry Applications*, vol. 55, no. 4, pp. 4145–4156, Jul. 2019.

[18] H. Torresan and D. Holmes, "A High Voltage Converter for Auxiliary Supply Applications using a Reduced Flying Capacitor Topology," in *2005 IEEE 36th Power Electronics Specialists Conference*, Jun. 2005, pp. 1220–1226.

[19] L. Zhu, C. Li, H. Yang, H. Yan, W. Li, and X. He, "Buck-Boost Type High Voltage DC Auxiliary Power Supply for Medium Voltage DC System," in *2021 IEEE 1st International Power Electronics and Application Symposium (PEAS)*, Nov. 2021, pp. 1–5.

[20] R. Steiner, P. K. Steimer, F. Krismer, and J. W. Kolar, "Contactless energy transmission for an isolated 100W gate driver supply of a medium voltage converter," in *2009 35th Annual Conference of IEEE Industrial Electronics*, Nov. 2009, pp. 302–307.

[21] K. Sun, Y. Xu, J. Wang, R. Burgos, and D. Boroyevich, "Insulation Design of Wireless Auxiliary Power Supply for Medium Voltage Converters," *IEEE Journal of Emerging and Selected Topics in Power Electronics*, vol. 9, no. 4, pp. 4200–4211, Aug. 2021.

[22] B. Wunsch, D. Zhelev, and B. Oedegard, "Externally-fed auxiliary power supply of MMC converter cells," in *2016 18th European Conference on Power Electronics and Applications (EPE'16 ECCE Europe)*, Karlsruhe: IEEE, Sep. 2016, pp. 1–10.

[23] J. Pan, F. Qi, H. Cai, and L. Xu, "Efficiency and electromagnetic interference analysis of wireless power transfer for high voltage gate driver application," in *2016 IEEE Energy Conversion Congress and Exposition (ECCE)*, Sep. 2016, pp. 1–5.

[24] M. Browne, *Physics for Engineering and Science*. New York: McGraw Hill/Schaum, 2013.

[25] D. Bui, T. M. Mostafa, A. P. Hu, and R. Hattori, "DC-DC Converter Based Impedance Matching for Maximum Power Transfer of CPT System with High Efficiency," in *2018 IEEE PELS Workshop on Emerging Technologies: Wireless Power Transfer (Wow)*, Jun. 2018, pp. 1–5.

[26] J. Dai and D. C. Ludois, "A Survey of Wireless Power Transfer and a Critical Comparison of Inductive and Capacitive Coupling for Small Gap Applications," *IEEE Transactions on Power Electronics*, vol. 30, no. 11, pp. 6017–6029, Nov. 2015.

[27] H. Zhang, F. Lu, H. Hofmann, and C. Mi, "A loosely coupled capacitive power transfer system with LC compensation circuit topology," in *2016 IEEE Energy Conversion Congress and Exposition (ECCE)*, Sep. 2016, pp. 1–5.

[28] L. J. Zou and A. P. Hu, "A Contactless Single-Wire CPT (Capacitive Power Transfer) Power Supply for Driving a Variable Message Sign," in *2018 IEEE PELS Workshop on Emerging Technologies: Wireless Power Transfer (Wow)*, Jun. 2018, pp. 1–5.

[29] J. C. Schuder, "Powering an Artificial Heart: Birth of the Inductively Coupled-Radio Frequency System in 1960," *Artificial Organs*, vol. 26, no. 11, pp. 909–915, 2002.

[30] T. B. Tang, S. Smith, B. W. Flynn, *et al.*, "Implementation of wireless power transfer and communications for an implantable ocular drug delivery system," *IET Nanobiotechnology*, vol. 2, no. 3, pp. 72–79, Sep. 2008.

[31] B. Farnsworth, D. Taylor, R. Triolo, and D. Young, *Wireless in Vivo EMG Sensor for Intelligent Prosthetic Control*. Jul. 2009, p. 361.

[32] O. Knecht, R. Bosshard, J. W. Kolar, and C. T. Starck, "Optimization of Transcutaneous Energy Transfer coils for high power medical applications," in *2014 IEEE 15th Workshop on Control and Modeling for Power Electronics (COMPEL)*, Jun. 2014, pp. 1–10.

[33] M. Zargham and P. G. Gulak, "Maximum Achievable Efficiency in Near-Field Coupled Power-Transfer Systems," *IEEE Transactions on Biomedical Circuits and Systems*, vol. 6, no. 3, pp. 228–245, Jun. 2012.

[34] P. Si, A. P. Hu, S. Malpas, and D. Budgett, "A Frequency Control Method for Regulating Wireless Power to Implantable Devices," *IEEE Transactions on Biomedical Circuits and Systems*, vol. 2, no. 1, pp. 22–29, Mar. 2008.

[35] Q. Xu, Z. Gao, H. Wang, J. He, Z.-H. Mao, and M. Sun, "Batteries Not Included: A Mat-Based Wireless Power Transfer System for Implantable Medical Devices As a Moving Target," *IEEE Microwave Magazine*, vol. 14, pp. 63–72, Mar. 2013.

[36] *Qi Wireless Charging | Wireless Power Consortium*, https://www.wirelesspowerconsortium.com/qi/.

[37] J. Baek, C. Ahn, B.-c. Kim, S. Choi, and S. Kwak, "High frequency wireless power transfer system for robot vacuum cleaner," in *2014 IEEE International Conference on Consumer Electronics (ICCE)*, Jan. 2014, pp. 308–310.

[38] J. M. Arteaga, S. Aldhaher, G. Kkelis, C. Kwan, D. C. Yates, and P. D. Mitcheson, "Dynamic Capabilities of Multi-MHz Inductive Power Transfer Systems Demonstrated With Batteryless Drones," *IEEE Transactions on Power Electronics*, vol. 34, no. 6, pp. 5093–5104, Jun. 2019.

[39] T. Dewi, P. Risma, Y. Oktarina, A. Taqwa, L. Prasetyani, and A. A. Astra, "Experimental Analysis on Wireless Power Transfer for Continuous Charging of a Mobile Robot," in *2019 International Conference on Technologies and Policies in Electric Power & Energy*, Oct. 2019, pp. 1–6.

[40] S. S. Williamson, U. Madawala, and D. Kumar, "Guest Editorial Advances in Wireless Power Transfer Technologies," *IEEE Journal of Emerging and Selected Topics in Industrial Electronics*, vol. 3, no. 3, pp. 391–393, Jul. 2022.

[41] "Ki Cordless Kitchen Standard | Wireless Power Consortium," Tech. Rep.

[42] L. J. Chen, J. T. Boys, and G. A. Covic, "A novel fast-switching control for multiple pickup IPT systems," in *2013 IEEE Energy Conversion Congress and Exposition*, Sep. 2013, pp. 2559–2565.

[43] G. A. Covic and J. T. Boys, "Modern Trends in Inductive Power Transfer for Transportation Applications," *IEEE Journal of Emerging and Selected Topics in Power Electronics*, vol. 1, no. 1, pp. 28–41, Mar. 2013.

[44] *Contactless power supply system for floor surface conveyors*, https://www.enrx.com/en/Products/Charge-and-power-products/Power-Floor-Contactless-power-supply.

[45] S. Y. Choi, B. W. Gu, S. Y. Jeong, and C. T. Rim, "Advances in Wireless Power Transfer Systems for Roadway-Powered Electric Vehicles," *IEEE Journal of Emerging and Selected Topics in Power Electronics*, vol. 3, no. 1, pp. 18–36, Mar. 2015.

[46] J. Kim, J. Kim, S. Kong, *et al.*, "Coil Design and Shielding Methods for a Magnetic Resonant Wireless Power Transfer System," *Proceedings of the IEEE*, vol. 101, no. 6, pp. 1332–1342, Jun. 2013.

[47] *Mass Transit - in-route charging*, https://wavecharging.com/products/wireless/mass-transit/.

[48] *IPT Dynamic Wireless Charging of Electric Vehicles*, https://www.enrx.com/en/Products/Charge-and-power-products/Electric-roadway.

[49] K. Kusaka, M. Kato, K. Orikawa, *et al.*, "Galvanic isolation system for multiple gate drivers with inductive power transfer — Drive of three-phase inverter," in *2015 IEEE Energy Conversion Congress and Exposition (ECCE)*, Montreal, QC, Canada: IEEE, Sep. 2015, pp. 4525–4532.

[50] C. Marxgut, J. Biela, J. W. Kolar, R. Steiner, and P. K. Steimer, "DC-DC converter for gate power supplies with an optimal air transformer," in *2010 Twenty-Fifth Annual IEEE Applied Power Electronics Conference and Exposition (APEC)*, Palm Springs, CA: IEEE, Feb. 2010, pp. 1865–1870.

[51] N. Yan, D. Dong, and R. Burgos, "A Multichannel High-Frequency Current Link Based Isolated Auxiliary Power Supply for Medium-Voltage Applications," *IEEE Transactions on Power Electronics*, vol. 37, no. 1, pp. 674–686, Jan. 2022.

[52] *Power Supplies GVA IPSS*, https://www.gva-power.de/komponenten/power-supplies-gva-ipss.

[53] J. Gottschlich, M. Schäfer, M. Neubert, and R. W. De Doncker, "A galvanically isolated gate driver with low coupling capacitance for medium voltage SiC MOSFETs," in *2016 18th European Conference on Power Electronics and Applications (EPE'16 ECCE Europe)*, Sep. 2016, pp. 1–8.

[54] D. Peftitsis, M. Antivachis, and J. Biela, "Auxiliary power supply for medium-voltage modular multilevel converters," in *2015 17th European Conference on Power Electronics and Applications (EPE'15 ECCE-Europe)*, Sep. 2015, pp. 1–11.

[55] S. Fuchs and J. Biela, "Output Voltage Stability of Series Connected Transformers for Isolated Auxiliary Supplies in Modular Medium Voltage Converter Systems," in *2018 20th European Conference on Power Electronics and Applications (EPE'18 ECCE Europe)*, Sep. 2018, P.1–P.9.

[56] *Siebel elektronik power supplies*, https://www.siebel-elektronik.de/en/power-supplies/power-supplies/.

[57] B. Wunsch, J. Bradshaw, I. Stevanovic, F. Canales, W. Van-der-Merwe, and D. Cottet, "Inductive power transfer for auxiliary power of medium voltage converters," in *2015 IEEE Applied Power Electronics Conference and Exposition (APEC)*, Charlotte, NC, USA: IEEE, Mar. 2015, pp. 2551–2556.

[58] R. Steiner, P. K. Steimer, F. Krismer, and J. W. Kolar, "Contactless energy transmission for an isolated 100W gate driver supply of a medium voltage converter," in *2009 35th Annual Conference of IEEE Industrial Electronics*, Nov. 2009, pp. 302–307.

[59] *Power Supplies « Power Supplies « en « Siebel Elektronik*.

[60] *Gva power supply system (gpss) gpss 221-24*, Datasheet GPSS 221-24, GvA, 2020.

[61] V.-T. Nguyen, V. U. Pawaskar, and G. Gohil, "Isolated Gate Driver for Medium-Voltage SiC Power Devices Using High-Frequency Wireless Power Transfer for a Small Coupling Capacitance," *IEEE Transactions on Industrial Electronics*, vol. 68, no. 11, pp. 10 992–11 001, Nov. 2021.

[62] K. Sun, J. Wang, R. Burgos, D. Boroyevich, J. Stewart, and N. Yan, "Design and Multiobjective Optimization of an Auxiliary Wireless Power Transfer Converter in Medium-Voltage Modular Conversion Systems," *IEEE Transactions on Power Electronics*, vol. 37, no. 8, pp. 9944–9958, Aug. 2022.

[63] J. Werthen, A. Andersson, S. Weiss, and H. Bjorklund, "Current measurements using optical power," in *Proceedings of 1996 Transmission and Distribution Conference and Exposition*, 1996, pp. 213–218.

[64] H. Fujita, "A Resonant Gate-Drive Circuit With Optically Isolated Control Signal and Power Supply for Fast-Switching and High-Voltage Power Semiconductor Devices," *IEEE Transactions on Power Electronics*, vol. 28, no. 11, pp. 5423–5430, Nov. 2013.

[65] *Diode Lasers: Research gives high-power diode lasers new capabilities | Laser Focus World*, https://www.laserfocusworld.com/lasers-sources/article/16556280/diode-lasers-research-gives-highpower-diode-lasers-new-capabilities.

[66] J. B. Rosolem, "Power-over-fiber applications for telecommunications and for electric utilities," in *Optical Fiber and Wireless Communications*, R. Roka, Ed., Rijeka: IntechOpen, 2017, ch. 13.

[67] S. Fafard, D. Masson, J. Werthen, *et al.*, "Ultrahigh efficiency optical power converters based on the vertical epitaxial heterostructure architecture (vehsa) design," in *The 1st Optical Wireless and Fiber Power Transmission Conference (OWPT2019)*, 2019.

[68] M. Röger, G. Böttger, M. Dreschmann, *et al.*, "Optically powered fiber networks," *Optics express*, vol. 16, no. 26, pp. 21 821–21 834, 2008.

[69] M. Haid, C. Armbruster, D. Derix, C. Schöner, and H. Helmers, "5w optical power link with generic voltage output and modulated data signal," in *Proceedings of the 1st Optical Wireless and Fiber Power Transmission Conference (OWPT2019)*, 2019, pp. 23–25.

[70] *MH GoPower*, http://www.mhgopower.com/laser_pof_Platform.html.

[71] *AFBR-POMEK2204*, https://www.broadcom.com/products/fiber-optic-modules-components/industrial/optical-power-components/afbr-pomek2204.

[72] *AFBR-POC306A1 Optical Power Converter*, https://www.broadcom.com/products/fiber-optic-modules-components/industrial/optical-power-components/optical-power-converters/afbr-poc306a1.

[73] V. Iyer, E. Bayati, R. Nandakumar, A. Majumdar, and S. Gollakota, "Charging a smartphone across a room using lasers," *Proceedings of the ACM on Interactive, Mobile, Wearable and Ubiquitous Technologies*, vol. 1, no. 4, pp. 1–21, 2018.

[74] S.-M. Kim and D.-H. Rhee, "Experimental demonstration of optical wireless power transfer with a dc-to-dc transfer efficiency of 12.1%," *Optical Engineering*, vol. 57, no. 8, p. 086 108, 2018.

[75] M. Budhia, G. Covic, and J. Boys, "A new IPT magnetic coupler for electric vehicle charging systems," in *IECON 2010 - 36th Annual Conference on IEEE Industrial Electronics Society*, Nov. 2010, pp. 2487–2492.

[76] Y. Nagatsuka, N. Ehara, Y. Kaneko, S. Abe, and T. Yasuda, "Compact contactless power transfer system for electric vehicles," in *The 2010 International Power Electronics Conference - ECCE ASIA -*, Jun. 2010, pp. 807–813.

[77] B. Sim, S. Jeong, S. Lee, S. Hong, H. Kim, and J. Kim, "Design and Analysis of Double-Eight Shaped Shielding Coil for Solenoid Coil in Loosely-Coupled Wireless Power Transfer System," in *2019 IEEE International Symposium on Electromagnetic Compatibility, Signal Power Integrity (EMC+SIPI)*, Jul. 2019, pp. 639–643.

[78] Y. Tang, F. Zhu, Y. Wang, and H. Ma, "Design and optimizations of solenoid magnetic structure for inductive power transfer in EV applications," in *IECON 2015 - 41st Annual Conference of the IEEE Industrial Electronics Society*, Nov. 2015, pp. 001 459–001 464.

[79] Q. Deng, J. Liu, D. Czarkowski, *et al.*, "Frequency-Dependent Resistance of Litz-Wire Square Solenoid Coils and Quality Factor Optimization for Wireless Power Transfer," *IEEE Transactions on Industrial Electronics*, vol. 63, no. 5, pp. 2825–2837, May 2016.

[80] R. Bosshard, J. Mühlethaler, J. W. Kolar, and I. Stevanović, "Optimized magnetic design for inductive power transfer coils," in *2013 Twenty-Eighth Annual IEEE Applied Power Electronics Conference and Exposition (APEC)*, Mar. 2013, pp. 1812–1819.

[81] T. Kan, T.-D. Nguyen, J. C. White, R. K. Malhan, and C. C. Mi, "A New Integration Method for an Electric Vehicle Wireless Charging System Using LCC Compensation Topology: Analysis and Design," *IEEE Transactions on Power Electronics*, vol. 32, no. 2, pp. 1638–1650, Feb. 2017.

[82] N. F. Ali Mohamed, J. I. Agbinya, and A. Okaf, "Magnetic Field Tuning and Control for Wireless Power Transfer Using Inductive Tuning Plunger and Conical Coils," in *2018 IEEE PELS Workshop on Emerging Technologies: Wireless Power Transfer (Wow)*, Jun. 2018, pp. 1–4.

[83] A. Ahmad, M. S. Alam, and R. Chabaan, "A Comprehensive Review of Wireless Charging Technologies for Electric Vehicles," *IEEE Transactions on Transportation Electrification*, vol. 4, no. 1, pp. 38–63, Mar. 2018.

[84] M. Budhia, J. T. Boys, G. A. Covic, and C.-Y. Huang, "Development of a Single-Sided Flux Magnetic Coupler for Electric Vehicle IPT Charging Systems," *IEEE Transactions on Industrial Electronics*, vol. 60, no. 1, pp. 318–328, Jan. 2013.

[85] D. Kurschner, C. Rathge, and U. Jumar, "Design Methodology for High Efficient Inductive Power Transfer Systems With High Coil Positioning Flexibility," *IEEE Transactions on Industrial Electronics*, vol. 60, no. 1, pp. 372–381, Jan. 2013.

[86] Y. Wang, Y. Yao, X. Liu, D. Xu, and L. Cai, "An LC/S Compensation Topology and Coil Design Technique for Wireless Power Transfer," *IEEE Transactions on Power Electronics*, vol. 33, no. 3, pp. 2007–2025, Mar. 2018.

[87] B. H. Choi, E. S. Lee, Y. H. Sohn, G. C. Jang, and C. T. Rim, "Six Degrees of Freedom Mobile Inductive Power Transfer by Crossed Dipole Tx and Rx Coils," *IEEE Transactions on Power Electronics*, vol. 31, no. 4, pp. 3252–3272, Apr. 2016.

[88] J. Zhang, X. Yuan, C. Wang, and Y. He, "Comparative Analysis of Two-Coil and Three-Coil Structures for Wireless Power Transfer," *IEEE Transactions on Power Electronics*, vol. 32, no. 1, pp. 341–352, Jan. 2017.

[89] S. C. Tang, S. Y. Hui, and Henry Shu-Hung Chung, "Coreless planar printed-circuit-board (PCB) transformers-a fundamental concept for signal and energy transfer," *IEEE Transactions on Power Electronics*, vol. 15, no. 5, pp. 931–941, Sep. 2000.

[90] C. R. Sullivan and R. Y. Zhang, "Analytical model for effects of twisting on litz-wire losses," in *2014 IEEE 15th Workshop on Control and Modeling for Power Electronics (COMPEL)*, Jun. 2014, pp. 1–10.

[91] T. Guillod, J. Huber, F. Krismer, and J. W. Kolar, "Litz wire losses: Effects of twisting imperfections," in *2017 IEEE 18th Workshop on Control and Modeling for Power Electronics (COMPEL)*, Jul. 2017, pp. 1–8.

[92] J. Acero, J. Serrano, C. Carretero, I. Lope, and J. M. Burdío, "Analysis and design of tubular coils for wireless inductive power transfer systems," in *2017 IEEE Applied Power Electronics Conference and Exposition (APEC)*, Mar. 2017, pp. 848–854.

[93] D. E. Gaona and T. Long, "Design Considerations for High-power-density IPT Pads using Nanocrystalline Ribbon Cores," in *2020 IEEE PELS Workshop on Emerging Technologies: Wireless Power Transfer (WoW)*, Nov. 2020, pp. 377–382.

[94] S. Somkun, T. Sato, V. Chunkag, A. Pannawan, P. Nunocha, and T. Suriwong, "Performance Comparison of Ferrite and Nanocrystalline Cores for Medium-Frequency Transformer of Dual Active Bridge DC-DC Converter," *Energies*, vol. 14, no. 9, p. 2407, Apr. 2021.

[95] D. E. Gaona and T. Long, "Feasibility Analysis of Nanocrystalline Cores for Polarize and Non-Polarized IPT Charging Pads," in *2019 IEEE Applied Power Electronics Conference and Exposition (APEC)*, Mar. 2019, pp. 1539–1546.

[96] A. Abdolkhani and A. P. Hu, "Improved Coupling Design of Contactless Slipring for Rotary Applications," *IEEE Journal of Emerging and Selected Topics in Power Electronics*, vol. 3, no. 1, pp. 288–295, Mar. 2015.

[97] R. Laouamer, M. Brunello, J. Ferrieux, O. Normand, and N. Buchheit, "A multi-resonant converter for non-contact charging with electromagnetic coupling," in *Proceedings of the IECON'97 23rd International Conference on Industrial Electronics, Control, and Instrumentation (Cat. No.97CH36066)*, vol. 2, Nov. 1997, 792–797 vol.2.

[98] W. Zhang, Q. Chen, S. Wong, C. K. Tse, and X. Ruan, "A novel transformer for contactless energy transmission systems," in *2009 IEEE Energy Conversion Congress and Exposition*, Sep. 2009, pp. 3218–3224.

[99] D. Pedder, A. Brown, and J. Skinner, "A contactless electrical energy transmission system," *IEEE Transactions on Industrial Electronics*, vol. 46, no. 1, pp. 23–30, Feb. 1999.

[100] G. Kkelis, D. C. Yates, and P. D. Mitcheson, "Comparison of current driven Class-D and Class-E half-wave rectifiers for 6.78 MHz high power IPT applications," in *2015 IEEE Wireless Power Transfer Conference (WPTC)*, May 2015, pp. 1–4.

[101] L. Shi, A. Delgado, R. Ramos, and P. Alou, "A Wireless Power Transfer System With Inverse Coupled Current Doubler Rectifier for High-Output Current Applications," *IEEE Transactions on Industrial Electronics*, vol. 69, no. 5, pp. 4607–4616, May 2022.

[102] R. Bosshard, J. W. Kolar, J. Mühlethaler, I. Stevanović, B. Wunsch, and F. Canales, "Modeling and η - α - Pareto Optimization of Inductive Power Transfer Coils for Electric Vehicles," *IEEE Journal of Emerging and Selected Topics in Power Electronics*, vol. 3, no. 1, pp. 50–64, Mar. 2015.

[103] *ETSI TR 103 493 V1.1.1 (2019-02) - System Reference document (SRdoc); Wireless Power Transmission (WPT) systems operating below 30 MHz*, https://standards.iteh.ai/catalog/standards/etsi/8349550e-1a8e-42f9-9ecb-6a4ad14a860a/etsi-tr-103-493-v1-1-1-2019-02.

[104] A. Alliance, *Frequency Choice*, https://airfuel.org/frequency-choice/, Jun. 2022.

[105] *Dreaming of Power through the Air | Wireless Power Consortium*, https://www.wirelesspowerconsortium.com/blog/246/dreaming-of-power-through-the-air.

[106] H. Hwang, B. Jo, S. Park, S.-W. Kim, C.-H. Jeong, and J. Moon, "A 13.56 MHz CMOS ring oscillator for wireless power transfer receiver system," in *TENCON 2014 - 2014 IEEE Region 10 Conference*, Oct. 2014, pp. 1–4.

[107] X. Li, C.-Y. Tsui, and W.-H. Ki, "A 13.56 MHz Wireless Power Transfer System With Reconfigurable Resonant Regulating Rectifier and Wireless Power Control for Implantable Medical Devices," *IEEE Journal of Solid-State Circuits*, vol. 50, no. 4, pp. 978–989, Apr. 2015.

[108] F. Stubenrauch, N. Seliger, M. Schustek, A. Lebedev, and D. Schmitt-Landsiedel, "A 13.56MHz class e power amplifier for inductively coupled DC supply with 95% power added efficiency (PAE)," in *2015 International EURASIP Workshop on RFID Technology (EURFID)*, Oct. 2015, pp. 87–93.

[109] *Power Electronics: Converters, Applications, and Design, 3rd Edition | Wiley*.

[110] S. Kim, M. Amirpour, T. Dharmakeerthi, *et al.*, "Thermal Evaluation of an Inductive Power Transfer Pad for Charging Electric Vehicles," *IEEE Transactions on Industrial Electronics*, vol. 69, no. 1, pp. 314–322, Jan. 2022.

[111] B. Zhang, J. Deng, W. Wang, *et al.*, "Multi-Objective Thermal Optimization Based on Improved Analytical Thermal Models of a 30 kW IPT System for EVs," *IEEE Transactions on Transportation Electrification*, pp. 1–1, 2022.

[112] K. van Schuylenbergh and R. Puers, *Inductive Powering: Basic Theory and Application to Biomedical Systems* (Analog Circuits and Signal Processing). Springer Netherlands, 2009.

[113] K. Van Schuylenbergh and R. Puers, Eds., *Inductive Powering*. Dordrecht: Springer Netherlands, 2009.

[114] B. Esteban, M. Sid-Ahmed, and N. C. Kar, "A Comparative Study of Power Supply Architectures in Wireless EV Charging Systems," *IEEE Transactions on Power Electronics*, vol. 30, no. 11, pp. 6408–6422, Nov. 2015.

[115] H. Feng, T. Cai, S. Duan, J. Zhao, X. Zhang, and C. Chen, "An LCC-Compensated Resonant Converter Optimized for Robust Reaction to Large Coupling Variation in Dynamic Wireless Power Transfer," *IEEE Transactions on Industrial Electronics*, vol. 63, no. 10, pp. 6591–6601, Oct. 2016.

[116] N. A. Keeling, G. A. Covic, and J. T. Boys, "A Unity-Power-Factor IPT Pickup for High-Power Applications," *IEEE Transactions on Industrial Electronics*, vol. 57, no. 2, pp. 744–751, Feb. 2010.

[117] H. Hao, G. A. Covic, and J. T. Boys, "An Approximate Dynamic Model of LCL- T-Based Inductive Power Transfer Power Supplies," *IEEE Transactions on Power Electronics*, vol. 29, no. 10, pp. 5554–5567, Oct. 2014.

[118] R. Steigerwald, "A comparison of half-bridge resonant converter topologies," *IEEE Transactions on Power Electronics*, vol. 3, no. 2, pp. 174–182, Apr. 1988.

[119] S. Y. R. Hui, W. Zhong, and C. K. Lee, "A Critical Review of Recent Progress in Mid-Range Wireless Power Transfer," *IEEE Trans. Power Electron.*, vol. 29, no. 9, pp. 4500–4511, Sep. 2014.

[120] G. R. Nagendra, G. A. Covic, and J. T. Boys, "Determining the Physical Size of Inductive Couplers for IPT EV Systems," *IEEE Journal of Emerging and Selected Topics in Power Electronics*, vol. 2, no. 3, pp. 571–583, Sep. 2014.

[121] R. Bosshard, U. Iruretagoyena, and J. W. Kolar, "Comprehensive Evaluation of Rectangular and Double-D Coil Geometry for 50 kW/85 kHz IPT System," *IEEE Journal of Emerging and Selected Topics in Power Electronics*, vol. 4, no. 4, pp. 1406–1415, Dec. 2016.

[122] S. S. Mohan, "The design, modeling and optimization of on-chip inductor and transformer circuits," p. 215,

[123] S. Mohan, M. del Mar Hershenson, S. Boyd, and T. Lee, "Simple accurate expressions for planar spiral inductances," *IEEE Journal of Solid-State Circuits*, vol. 34, no. 10, pp. 1419–1424, Oct. 1999.

[124] I. Lope, C. Carretero, J. Acero, R. Alonso, and J. M. Burdío, "AC Power Losses Model for Planar Windings With Rectangular Cross-Sectional Conductors," *IEEE Transactions on Power Electronics*, vol. 29, no. 1, pp. 23–28, Jan. 2014.

[125] K. Sun, Y. Xu, J. Wang, R. Burgos, and D. Boroyevich, "Insulation Design of Wireless Auxiliary Power Supply for Medium Voltage Converters," *IEEE Journal of Emerging and Selected Topics in Power Electronics*, pp. 1–1, 2020.

[126] O. C. Spro, P. Lefranc, S. Park, *et al.*, "Optimized Design of Multi-MHz Frequency Isolated Auxiliary Power Supply for Gate Drivers in Medium-Voltage Converters," *IEEE Transactions on Power Electronics*, vol. 35, no. 9, pp. 9494–9509, Sep. 2020.

[127] "Adjustable speed electrical power drive systems. Part 5-1: Safety requirements – Electrical, thermal and energy," CEI, Standard, Jul. 2007.

[128] S. Babic and C. Akyel, "New analytic-numerical solutions for the mutual inductance of two coaxial circular coils with rectangular cross section in air," *IEEE Transactions on Magnetics*, vol. 42, no. 6, pp. 1661–1669, Jun. 2006.

[129] W. Kuhn and N. Ibrahim, "Analysis of current crowding effects in multiturn spiral inductors," *IEEE Transactions on Microwave Theory and Techniques*, vol. 49, no. 1, pp. 31–38, Jan. 2001.

[130] M. Q. Nguyen, Z. Hughes, P. Woods, Y. Seo, S. Rao, and J. Chiao, "Field Distribution Models of Spiral Coil for Misalignment Analysis in Wireless Power Transfer Systems," *IEEE Transactions on Microwave Theory and Techniques*, vol. 62, no. 4, pp. 920–930, Apr. 2014.

[131] E. B. Rosa and F. W. Grover, *Formulas and Tables for the Calculation of Mutual and Self-inductance*. U.S. Government Printing Office, 1948.

[132] M. Mogorovic and D. Dujic, "100 kW, 10 kHz Medium-Frequency Transformer Design Optimization and Experimental Verification," *IEEE Transactions on Power Electronics*, vol. 34, no. 2, pp. 1696–1708, Feb. 2019.

[133] C. Zierhofer and E. Hochmair, "Geometric approach for coupling enhancement of magnetically coupled coils," *IEEE Transactions on Biomedical Engineering*, vol. 43, no. 7, pp. 708–714, Jul. 1996.

[134] "IPC-9592 : Requirements for Power Conversion Devices for the Computer and Telecommunications Industries," Tech. Rep.

[135] *2221A: Generic Standard on Printed Board Design | IPC Store*.

[136] R. Bosshard, J. W. Kolar, J. Mühlethaler, I. Stevanović, B. Wunsch, and F. Canales, "Modeling and η - α - Pareto Optimization of Inductive Power Transfer Coils for Electric Vehicles," *IEEE Journal of Emerging and Selected Topics in Power Electronics*, vol. 3, no. 1, pp. 50–64, Mar. 2015.

[137] S. Mehri, A. C. Ammari, J. Slama, and M. Sawan, "Minimizing printed spiral coil losses for inductive link wireless power transfer," in *2016 IEEE Wireless Power Transfer Conference (WPTC)*, May 2016, pp. 1–4.

[138] R. Chedraui, "Design and prototyping of an ac-ac converter for an inductive power transfer system," M.S. thesis, ÉCOLE POLYTECHNIQUE FÉDÉRALE DE LAUSANNE, 2021.

[139] W. Roshen and D. Turcotte, "Planar inductors on magnetic substrates," *IEEE Transactions on Magnetics*, vol. 24, no. 6, pp. 3213–3216, Nov. 1988.

[140] C. Steinmetz, "On the law of hysteresis," *Proceedings of the IEEE*, vol. 72, no. 2, pp. 197–221, 1984.

[141] B.-G. Choi and Y.-S. Kim, "New Structure Design of Ferrite Cores for Wireless Electric Vehicle Charging by Machine Learning," *IEEE Transactions on Industrial Electronics*, vol. 68, no. 12, pp. 12 162–12 172, Dec. 2021.

[142] M. G. S. Pearce, G. A. Covic, and J. T. Boys, "Robust Ferrite-Less Double D Topology for Roadway IPT Applications," *IEEE Transactions on Power Electronics*, vol. 34, no. 7, pp. 6062–6075, Jul. 2019.

[143] T. Diekhans and R. W. De Doncker, "A Dual-Side Controlled Inductive Power Transfer System Optimized for Large Coupling Factor Variations and Partial Load," *IEEE Transactions on Power Electronics*, vol. 30, no. 11, pp. 6320–6328, Nov. 2015.

[144] Z. Wang, X. Huang, Z. Kong, and X. Zhang, "Edge Effect and Coil Optimization of Wireless Power Transmission System for Electric Vehicle Charging," in *2019 2nd International Conference on Mathematics, Modeling and Simulation Technologies and Applications (MMSTA 2019)*, Atlantis Press, Dec. 2019, pp. 73–77.

[145] M. Mu, F. C. Lee, Q. Li, D. Gilham, and K. D. T. Ngo, "A high frequency core loss measurement method for arbitrary excitations," in *2011 Twenty-Sixth Annual IEEE Applied Power Electronics Conference and Exposition (APEC)*, Mar. 2011, pp. 157–162.

[146] T.-H. Kim, S. Yoon, J.-G. Yook, G.-H. Yun, and W. Y. Lee, "Evaluation of power transfer efficiency with ferrite sheets in wpt system," in *2017 IEEE Wireless Power Transfer Conference (WPTC)*, 2017, pp. 1–4.

[147] M. Chen, M. Araghchini, K. K. Afridi, J. H. Lang, C. R. Sullivan, and D. J. Perreault, "A Systematic Approach to Modeling Impedances and Current Distribution in Planar Magnetics," *IEEE Transactions on Power Electronics*, vol. 31, no. 1, pp. 560–580, Jan. 2016.

[148] W. Roshen and D. Turcotte, "Planar inductors on magnetic substrates," *IEEE Transactions on Magnetics*, vol. 24, no. 6, pp. 3213–3216, 1988.

[149] W. Roshen, "Effect of finite thickness of magnetic substrate on planar inductors," *IEEE Transactions on Magnetics*, vol. 26, no. 1, pp. 270–275, 1990.

[150] K. O'Donoghue and P. Cantillon-Murphy, "Planar magnetic shielding for use with electromagnetic tracking systems," *IEEE Transactions on Magnetics*, vol. 51, no. 2, pp. 1–12, 2015.

[151] W. Hurley and M. Duffy, "Calculation of self- and mutual impedances in planar sandwich inductors," *IEEE Transactions on Magnetics*, vol. 33, no. 3, pp. 2282–2290, May 1997.

[152] Y. P. Su, X. Liu, and S. Y. R. Hui, "Mutual Inductance Calculation of Movable Planar Coils on Parallel Surfaces," *IEEE Transactions on Power Electronics*, vol. 24, no. 4, pp. 1115–1123, Apr. 2009.

[153] P. T. Luu, J.-Y. Lee, J.-W. Kim, S.-U. Chung, and S.-M. Kwon, "Magnetic sensor design for a permanent magnet linear motor considering edge-effect," *IEEE Transactions on Industrial Electronics*, vol. 67, no. 7, pp. 5768–5777, 2020.

[154] T. Diekhans and R. W. De Doncker, "A dual-side controlled inductive power transfer system optimized for large coupling factor variations and partial load," *IEEE Transactions on Power Electronics*, vol. 30, no. 11, pp. 6320–6328, 2015.

[155] Y. Otomo and H. Igarashi, "A 3-d topology optimization of magnetic cores for wireless power transfer device," *IEEE Transactions on Magnetics*, vol. 55, no. 6, pp. 1–5, 2019.

[156] H. Liu, J. Xie, S. Yang, C. Zhu, X. Zhang, and F. Lu, "A General Data-driven Design Methodology of Magnetic Couplers for Wireless Power Transfer Systems," in *IECON 2022 – 48th Annual Conference of the IEEE Industrial Electronics Society*, Oct. 2022, pp. 1–6.

[157] R. Bosshard and J. W. Kolar, "Multi-objective optimization of 50 kw/85 khz ipt system for public transport," *IEEE Journal of Emerging and Selected Topics in Power Electronics*, vol. 4, no. 4, pp. 1370–1382, 2016.

[158] Z. Luo, X. Wei, M. G. S. Pearce, and G. A. Covic, "Multiobjective Optimization of Inductive Power Transfer Double-D Pads for Electric Vehicles," *IEEE Transactions on Power Electronics*, vol. 36, no. 5, pp. 5135–5146, May 2021.

[159] S. Inoue, R. Nimri, A. Kamineni, and R. Zane, "A new design optimization method for dynamic inductive power transfer systems utilizing a neural network," in *2021 IEEE Energy Conversion Congress and Exposition (ECCE)*, 2021, pp. 1496–1501.

[160] B. K. Bose, "Neural network applications in power electronics and motor drives—an introduction and perspective," *IEEE Transactions on Industrial Electronics*, vol. 54, no. 1, pp. 14–33, 2007.

[161] D. Santamargarita, G. Salinas, M. Vasic, and E. Bueno, "Trade-off between accuracy and computational time for magnetics thermal model based on artificial neural networks (ann)," in *2021 IEEE Design Methodologies Conference (DMC)*, 2021, pp. 1–6.

[162] T. Guillod, P. Papamanolis, and J. W. Kolar, "Artificial neural network (ann) based fast and accurate inductor modeling and design," *IEEE Open Journal of Power Electronics*, vol. 1, pp. 284–299, 2020.

[163] H. Liu, J. Xie, S. Yang, C. Zhu, X. Zhang, and F. Lu, "A general data-driven design methodology of magnetic couplers for wireless power transfer systems," in *IECON 2022 – 48th Annual Conference of the IEEE Industrial Electronics Society*, 2022, pp. 1–6.

[164] B. Jones and D. C. Montgomery, *Design of Experiment: A Modern Approach*. Wiley, Nov. 2019.

[165] Incropera, DeWitt, Bergman, Lavine, *Fundamentals about heat and mass transfer*. New York: Wiley: Sixth Edition, 1996.

[166] SivabalanMohan, "Thermal comparison of fr-4 and insulated metal substrate pcb for gan inverter," Texas Instruments, Tech. Rep., 2019.

[167] "Ferrite materials survey," Ferroxcube, Tech. Rep., 2008.
[168] *The thermal conductivity of unfilled plastics*, https://ctherm.com/resources/newsroom/blog/the-thermal-conductivity-of-unfilled-plastics/.
[169] "Emissivity measurements of additively manufactured materials," Los Alamos National Lab. (LANL), Los Alamos, NM (United States), Tech. Rep., 2017.
[170] *Surface emissivity coefficients*, https://www.engineeringtoolbox.com/emissivity-coefficients-d$_4$47.*html*.
[171] B. Ozpineci, L. Tolbert, and J. Chiasson, "Harmonic optimization of multilevel converters using genetic algorithms," *IEEE Power Electronics Letters*, vol. 3, no. 3, pp. 92–95, 2005.
[172] J. Zhang, H. Chung, and W. Lo, "Pseudocoevolutionary genetic algorithms for power electronic circuits optimization," *IEEE Transactions on Systems, Man, and Cybernetics, Part C (Applications and Reviews)*, vol. 36, no. 4, pp. 590–598, 2006.
[173] M. Pong, X. Wu, C. Lee, and Z. Qian, "Reduction of crosstalk on printed circuit board using genetic algorithm in switching power supply," *IEEE Transactions on Industrial Electronics*, vol. 48, no. 1, pp. 235–238, 2001.
[174] A. Garcia-Bediaga, I. Villar, A. Rujas, L. Mir, and A. Rufer, "Multiobjective optimization of medium-frequency transformers for isolated soft-switching converters using a genetic algorithm," *IEEE Transactions on Power Electronics*, vol. 32, no. 4, pp. 2995–3006, 2017.
[175] T. Wu, Z. Wang, B. Ozpineci, M. Chinthavali, and S. Campbell, "Automated heatsink optimization for air-cooled power semiconductor modules," *IEEE Transactions on Power Electronics*, vol. 34, no. 6, pp. 5027–5031, 2019.
[176] *How the genetic algorithm works*, https://ch.mathworks.com/help/gads/how-the-genetic-algorithm-works.html.
[177] *Gamultiobj*, https://ch.mathworks.com/help/gads/gamultiobj.html.
[178] "Insulation coordination for equipment within low-voltage systems – Part 1: Principles, requirements and tests," CEI, Standard, Apr. 2007.
[179] D. A. do Nascimento, Y. Iano, H. J. Loschi, L. A. de Sousa Ferreira, J. A. D. Rossi, and C. D. Pessoa, *International Journal of Emerging Electric Power Systems*, vol. 19, no. 1, p. 20 170 160, 2018.
[180] H. Zainuddin, P. L. Lewin, and P. M. Mitchinson, "Partial discharge characteristics of surface tracking on oil-impregnated pressboard under ac voltages," in *2013 IEEE International Conference on Solid Dielectrics (ICSD)*, 2013, pp. 1016–1019.
[181] B. Zojer, "Driving coolgan™ 600 v high electron mobility transistors," *Application note, Infineon*, 2018.
[182] *Würth elektronik redexpert*, https://redexpert.we-online.com/we-redexpert.
[183] L. Zhou and M. Preindl, "Inductor Design for Nonisolated Critical Soft Switching Converters Using Solid and Litz PCB and Wire Windings Leveraging Neural Network Model," *IEEE Transactions on Power Electronics*, vol. 37, no. 3, pp. 3357–3373, Mar. 2022.

Xiaotong Du

PhD candidate in Power Electronics

✉ *xiaotong.du@alumni.epfl.ch*
July 1st 1995
Chinese, single

HIGHER EDUCATION

École Polytechnique Fédérale de Lausanne, Lausanne, Switzerland

2019-2023 Ph.D. candidate in EDEE Electrical Engineering Doctoral School

Xi'an Jiaotong University, Xi'an, China

2016-2019 MSc. in Electrical Engineering School

Ecole Centrale Nantes, Nantes, France

2014-2016 Exchange student in Engineering Program

Xi'an Jiaotong University, Xi'an, China

2012-2016 BSc. in Electrical Engineering School

TEACHING / SUPERVISION EXPERIENCE

2021 Supervision of one MSc. student project

2021 Teaching assistant for the course Industrial Electronics II
Modeling and control of power electronics converters and motor drives

2020 Teaching assistant for the course Industrial Electronics I
Modeling and control of grid-connected power electronics converters

2020 Teaching assistant for the course Power Electronics
Design a 50W dc-dc converter

PROFESSIONAL EXPERIENCE

2019-2023	École Polytechnique Fédérale de Lausanne, Switzerland Doctoral assistant
2016	Peugeot Citroën, France Intern in research center

LANGUAGES

English	Level C1
French	Level B1+
Chinese	Mother tongue

COMPUTER TOOLS AND CODING

Simulation	Ansys Maxwell, Plecs
PCB design	Altium Designer
Coding	Matlab, C, C++, python
Mechanic design	Autodesk Inventor